

## On the free-surface vortex driven motion of buoyant particles

Duinmeijer, Alex

**DOI**

[10.4233/uuid:a33fa2a9-f347-40a3-96be-51e880018974](https://doi.org/10.4233/uuid:a33fa2a9-f347-40a3-96be-51e880018974)

**Publication date**

2020

**Document Version**

Final published version

**Citation (APA)**

Duinmeijer, A. (2020). On the free-surface vortex driven motion of buoyant particles.  
<https://doi.org/10.4233/uuid:a33fa2a9-f347-40a3-96be-51e880018974>

**Important note**

To cite this publication, please use the final published version (if applicable).  
Please check the document version above.

**Copyright**

Other than for strictly personal use, it is not permitted to download, forward or distribute the text or part of it, without the consent of the author(s) and/or copyright holder(s), unless the work is under an open content license such as Creative Commons.

**Takedown policy**

Please contact us and provide details if you believe this document breaches copyrights.  
We will remove access to the work immediately and investigate your claim.

Voor Mamma



# **ON THE FREE-SURFACE VORTEX DRIVEN MOTION OF BUOYANT PARTICLES**

## **Proefschrift**

ter verkrijging van de graad van doctor  
aan de Technische Universiteit Delft,  
op gezag van de Rector Magnificus prof. dr. ir. T.H.J.J. van der Hagen  
voorzitter van het College voor Promoties,  
in het openbaar te verdedigen  
op vrijdag 15 Mei 2020 om 12:30 uur

door

**Simon Petrus Alexander DUINMEIJER**

Civiel Ingenieur, Technische Universiteit Delft  
geboren te Alkmaar, Nederland

Dit proefschrift is goedgekeurd door:

promotor: prof. dr. ir. F.H.L.R. Clemens

copromotor: dr. ir. G. Oldenziel

*Samenstelling promotiecommissie:*

Rector Magnificus

Prof. dr. ir. F.H.L.R. Clemens

Dr. ir. G. Oldenziel

Voorzitter

Technische Universiteit Delft

Technische Universiteit Delft

*Onafhankelijke leden:*

Prof. dr. ir. W. Uijtewaal

Prof. dr. S. Tait

Prof. dr. ing. D. Muschalla

Dr. G. Lipeme-Kouyi

Prof. dr. Z. Kapelan

Technische Universiteit Delft

University of Sheffield

Graz University of Technology

Institut National des Sciences Appliquées  
de Lyon

Technische Universiteit Delft, reserve lid

*Overig lid:*

Dr. ir. I.W.M. Pothof

Technische Universiteit Delft

Dit onderzoek is financieel mogelijk gemaakt door het Ingenieursbureau en de afdeling Water van de gemeente Rotterdam.

© 2020 by S.P.A. Duinmeijer

ISBN: 978-94-6366-271-0

Printed by Gildeprint, Enschede

Cover design by S.P.A. Duinmeijer

An electronic version of this dissertation is available at

<http://repository.tudelft.nl/>.

*“I have no special talent. I am only passionately curious”*

Albert Einstein



# CONTENTS

<b>Summary</b> .....	<b>xi</b>
<b>Samenvatting</b> .....	<b>xv</b>
<b>List of symbols</b> .....	<b>xix</b>
<b>1 Introduction</b> .....	<b>1</b>
1.1 The wastewater pumping station .....	2
1.2 Problems with floating solids in pump sumps .....	2
1.3 Sump design for transport of floating solids.....	6
1.3.1 Review of current guidelines with respect to removal of floating solids	6
1.3.2 The ‘no-sump’ principle	7
1.3.3 Transport of FOG by kinetic energy	8
1.4 Problem definition .....	9
1.5 Research questions .....	9
1.6 Research structure .....	9
<b>2 Experimental set-up and measuring techniques</b> .....	<b>13</b>
2.1 Introduction .....	14
2.2 The vortex tank set-up .....	14
2.2.1 Vortex tank measuring techniques	14
2.2.2 Uncertainty analysis	17
2.2.3 Influence of scale effects	18
2.3 Particle Tracking Velocimetry.....	18
2.3.1 Set-up	18
2.3.2 Control software and SQL database	19
2.3.3 Camera calibration	19
2.3.4 Reconstruction of the 2D-positions of the particle from the camera images	21
2.3.5 Determining the refraction indices	23
2.3.6 Uncertainty in 3D particle position	24
2.3.7 Particle reflections on water/air surfaces	24
2.4 Stereo Particle Image Velocimetry .....	25
2.4.1 Set-up	25
2.4.2 Contour averaging method	25
2.4.3 The weighted conditional averaging method	27
2.5 Experimental particles .....	27

<b>3</b>	<b>The Free-surface Vortex 3D-flow field .....</b>	<b>29</b>
3.1	Introduction .....	30
3.2	The free-surface vortex and the Burgers vortex model.....	31
3.3	Experimental program .....	33
3.4	Experimental results .....	34
	3.4.1 Circulation	34
	3.4.2 Tangential velocity profiles	34
	3.4.3 Radial velocity profiles	35
	3.4.4 Axial velocity profiles	37
	3.4.5 Secondary flow patterns	37
3.5	Axial vortex flow.....	38
3.6	Validation of the Burgers model to determine the core radius.....	40
	3.6.1 Vortex core radius	40
	3.6.2 Relation between $U_o$ and core radius	40
	3.6.3 Validation of Burgers' model when using radially dependent $V_z$ profiles	41
3.7	Computation of the air core depth with the Burgers model .....	43
	3.7.1 Influence of surface tension	44
	3.7.2 Validation of the expression to compute the surface elevation	45
	3.7.3 Computation of the air core depth with the Burgers model	46
3.8	Conclusions .....	46
<b>4</b>	<b>Vortex driven particle motion: helical motion along the air core .....</b>	<b>49</b>
4.1	Introduction .....	50
4.2	Mathematical model of the free-surface vortex driven particle motion .....	52
	4.2.1 Introduction	52
	4.2.2 Model limitations	52
	4.2.3 2D approach	52
	4.2.4 General equation of particle motion	54
	4.2.5 Inertial force	54
	4.2.6 Drag force	55
	4.2.7 Flow vorticity induced lift force	55
	4.2.8 Particle's rotation lift force (Magnus force)	56
4.3	Experimental procedure and programme .....	59
	4.3.1 Experimental Procedure	59
	4.3.2 Experimental Programme	59
4.4	Experimental results .....	60
	4.4.1 Evaluation of the mathematical model	60
	4.4.2 Limited repeatability of the experimental particle motion	62
	4.4.3 Analysis of the predictability by applying phase portraits	62
	4.4.4 Quantification of the predictability by the Largest Lyapunov Exponent	65
4.5	Motion parameter for continuous downward motion along the air core .....	67

4.5.1	Definition of a continuous downward motion	67
4.5.2	Motion parameter	68
4.6	Conclusions .....	69
<b>5</b>	<b>Vortex driven particle motion: motion through the vortex core .....</b>	<b>73</b>
5.1	Introduction .....	74
5.2	Experimental procedure and programme .....	75
5.2.1	Procedure	75
5.2.2	Experimental programme	76
5.3	Experimental results .....	76
5.3.1	Measured axial motion of the spheres	76
5.3.2	Measured axial motion of the cubes	78
5.3.3	Measured axial motion of the ellipsoids	78
5.4	The axial velocity profile in the vortex core .....	79
5.4.1	Theoretical approximation of the measured profile	79
5.4.2	Radially uniform axial velocity	80
5.5	Determination of the stage 2 motion condition .....	81
5.5.1	Motion condition based on the independent experimental parameters	81
5.5.2	Motion condition based on Taylor-column drag force	83
5.6	Discussion .....	92
5.7	Conclusions .....	92
<b>6</b>	<b>Conclusions and recommendations .....</b>	<b>95</b>
6.1	Conclusions .....	96
6.1.1	Conclusions on the free-surface vortex	96
6.1.2	Conclusions on the free-surface vortex driven motion of buoyant particles	96
6.1.3	General conclusion on the potential of a free-surface vortex as a mean for the downward transport of buoyant particles	98
6.1.4	Engineering aspects	98
6.2	Recommendations .....	98
<b>References</b>	<b>.....</b>	<b>101</b>
<b>A</b>	<b>3D-Particle Tracking Velocimetry .....</b>	<b>109</b>
<b>B</b>	<b>Stereo PIV measured velocity profiles .....</b>	<b>115</b>
<b>C</b>	<b>2D-PTV particle motion results .....</b>	<b>119</b>
<b>D</b>	<b>3D-PTV particle motion results .....</b>	<b>127</b>
<b>E</b>	<b>Equations for the 2D motion of spherical particles .....</b>	<b>139</b>
<b>F</b>	<b>Comparison of physical results with CFD results .....</b>	<b>143</b>

<b>Acknowledgements.....</b>	<b>151</b>
<b>List of publications.....</b>	<b>153</b>
<b>About the author .....</b>	<b>155</b>

# SUMMARY

The presence of small floating particles of fat, oil and grease and other trash (hereafter referred to as: floating solids) in the sumps of wastewater pumping stations can cause various problems. The individual solids can accumulate together to form larger pieces. These pieces can clog the impellers of centrifugal pumps. The clogging can result in pump failures and during storm events this results in an increase in the (combined) sewer overflow volume. The floating solids can also 'cake' up to a thick and hard floating layer that covers the entire sump surface. These layers have been observed with a thickness of up to 2 m. To ensure the serviceability of the pumping station, the large solids and clusters thereof and the floating layers are periodically removed by hand. The cleaning of the sumps is a labor-intensive, dangerous and very unhygienic job with high costs. In conclusion, the formation of floating layers must be reduced to a minimum. The current guidelines for sump design only deal in a superficial manner with the transport of floating solids and for a limited number of sump geometries only. The guidelines mainly focus on preventing unfavorable flow conditions at the pump inlet e.g. pre-rotation, formation of eddies and air-entrainment by vortices. Applying optimal flow conditions according to the guidelines may even result in an increase of floating solids as regularly observed in practice. To reduce the problem of floating layer formation, two methods are thought as potentially effective. The first method uses the kinetic energy of the fluid in the sump i.e. increasing the turbulent motion of the fluid and floating solids to bring the solids into suspension. The second method is the application of a free-surface vortex for the transport of the solids toward the submerged suction inlet. The goal of this thesis is to study the potential of the vortex as a mean for the downward motion of buoyant particles.

The potential is studied with a laboratory set-up consisting of an  $\sim\varnothing 600$  mm acrylic tank with a height of  $\sim 1000$  mm in which vortices are generated under controlled conditions. The first step in this study was (1) to analyse the vortex flow field and (2) the validation of the Burgers (1948) vortex model. This model describes the three-dimensional velocity field (tangential, radial and axial velocity) by applying two characteristic parameters: the flow circulation  $\Gamma$  and the vortex core radius  $r_c$ . The core radius divides the flow field in an irrotational field (with zero vorticity) and a field in solid-body rotation (the vortex core). The flow velocities are measured at three horizontal planes at different heights by means of Stereo Particle Image Velocimetry (SPIV). The SPIV measurements indeed show that the flow field is divided in an

irrotational and rotational field. The results show that approximately 10 to 25% of the flow is carried by the vortex core and that the axial flow is concentrated within a domain of approximately  $\sim 2r_c$ . The Burgers model quantifies the tangential velocity within an accuracy of  $\sim 10\%$ . The maximum difference between the measured and calculated air core depth is  $\sim 20\%$ . Furthermore, the experiments revealed no radial diffusion of mass by turbulence in the vortex core.

The vortex flow driven motion of particles is measured by application of 2D- and 3D-Particle Tracking Velocimetry. The experimental particles are spherical, cubical and ellipsoid shaped with a characteristic length  $L$  of  $\sim 0.02$  to  $\sim 0.04$  m and a specific density in the range of  $\sim 600$  to  $1.000$  kg m<sup>-3</sup>. The  $\sim 700$  experiments revealed two distinct stages in the vortex driven particle motion: the stage 1 motion is the helical motion along the vortex air core. The stage 2 motion is the axial motion through the vortex core. The particle Reynolds number in stage 1 is  $\sim 10^2 < Re_p < \sim 10^4$  and the axial particle Reynolds number in stage 2 is  $\sim 10^2 < Re_{p,z} < \sim 6 \cdot 10^3$ . The motion in stage 1 has a strong dependency on the initial conditions of the particle at the water surface e.g. the initial velocity and rotation of the particle. Due to this strong dependency the system shows chaotic behavior. As an example: in one experiment the particle moves away from the vortex center while in the other experiment the particle moves towards the center at equal hydraulic conditions but slightly different initial particle conditions. This behavior can be characteristic for some non-linear systems. To qualify this behavior, a simplified mathematical model is developed that describes the vortex driven particle motion in the horizontal plane. The model results also show that the motion strongly depends on the initial condition and thus showing chaotic behavior. Both the chaotic characteristics of the experimental and model results is quantified by the calculation of the Largest Lyapunov exponent. The conclusion is that there is a limited predictability only of the stage 1 motion where the motion allows to be analysed in a qualitative manner only by mean of phase portraits. However, it is to be noted that this limited predictability mainly applies to spherical particles. The cubes and ellipsoidal particles seem to exhibit less chaotic behavior. For the stage 1 motion, a motion parameter is proposed which provides a first indication if a continuous downward motion along the vortex air core occurs.

The study on the stage 2 motion (axial motion through the vortex core) shows that it is pointless to predict this motion by applying the uniform drag force approach and the related standard drag coefficient  $C_D$ . The drag force on the particle appears to be determined by the presence of a Taylor column surrounding the particle. Proudman (1916) and Taylor (1917) discovered that a rising spherical object in a rotating liquid is accompanied by a surrounding column of liquid. This column is responsible for the axial drag force on the particle. By applying the Taylor column theory, a motion

condition is formulated that provides a first indication if downward axial motion through the vortex core occurs.

To apply the free-surface vortex as a transport mechanism in practice, data is required on the hydraulic and geometrical conditions that provides the occurrence of a vortex. The use of a single-phase CFD model as an engineering tool seems able to provide a first indication of the vortex occurrence. This approach, however, is not able to simulate the vortex characteristics accurately and the use of physical (scale) models is preferred.



# SAMENVATTING

De aanwezigheid van stukjes drijfvuil zoals gestolde vetten in het ontvangstbassin van een rioolgemaal kan leiden tot verschillende problemen. De losse stukjes kunnen samenklonteren tot grotere stukken die de waaiers van de pompen kunnen verstopen waardoor pompstoring optreedt. Tijdens hevige regenval kan dit resulteren in een toename van overstortend rioolwater. De stukjes kunnen daarnaast ‘aankoeken’ tot een dikke en harde drijfslag die het volledige oppervlak van het bassin bedekt. In de praktijk komen drijfslagen voor van 2 m hoog. Drijfvuil en drijfslagen worden periodiek handmatig verwijderd om de bedrijfszekerheid van het rioolgemaal te garanderen. Het reinigen is arbeidsintensief, gevaarlijk en onhygiënisch werk wat bovendien veel geld kost. Kortom, drijfslagvorming moet tot een minimum worden beperkt. De huidige normen voor het ontwerp van ontvangstbassins van rioolgemalen houden weinig tot geen rekening met het tegengaan van drijfslagvorming. De normen zijn voornamelijk gericht op het voorkomen van ongunstige stromingscondities nabij de zuigmond zoals prerotatie, wervelvorming door loslating van stroming en luchtaanzuiging door vortexen. Het toepassen van deze normen kan zelfs resulteren in een onbedoelde toename van drijfvuil. In het kader van dit promotieonderzoek zijn twee methodes opgesteld die potentieel bieden om drijfslagvorming te minimaliseren. De eerste methode is gebaseerd op het verhogen van de kinetische energie van het water ofwel verhogen van de turbulente bewegingen van het water en drijfvuil (dit betreft niet de turbulente vloeistofbewegingen op microscopische schaal). De tweede methode betreft het gebruik van een vortex voor ‘verticaal’ transport van drijfvuil naar de zuigmond. De doelstelling van dit promotieonderzoek betreft het onderzoek naar het potentieel van een vortex als mechanisme voor het verticale transport van drijvend materiaal.

Het potentieel is onderzocht in een laboratoriumopstelling bestaande uit een  $\varnothing 600$  mm acrylaat tank van circa 1000 mm hoog waarin een vortex wordt gegenereerd onder gecontroleerde condities. De eerste stap in het onderzoek was (1) het analyseren van de driedimensionale stroming in de vortex en (2) een validatie van het Burgers (1948) vortexmodel. Dit model voorspelt de tangentiële, radiale en axiale stroomsnelheden op basis van een tweetal karakteristieke parameters: de circulatie  $\Gamma$  en de radius  $r_c$  van de vortexkern. De radius verdeelt de stroming in twee typen: een rotatievrije stroming en een stroming in solid-body rotatie (de vortexkern). Met Stereo Particle Image Velocimetry zijn de stroomsnelheden gemeten in drie horizontale vlakken op

verschillende hoogtes. De metingen tonen aan dat de tangentiële stroming inderdaad bestaat uit een rotatievrije stroming en een stroming in solid-body rotatie. De metingen laten tevens zien dat circa 10 tot 25% van het totale instromende debiet door de vortexkern stroomt. Deze axiale stroming is geconcentreerd in een gebied met een straal van  $\sim 2r_c$ . Het Burgers model voorspelt de tangentiële stroomsnelheid met een relatieve nauwkeurigheid van circa 10%. De voorspelde diepte van de luchtkern wijkt tot maximaal  $\sim 20\%$  af van de gemeten waarden. De experimenten tonen tevens aan dat radiale diffusie van massa door turbulentie verwaarloosbaar is.

Met behulp van 2D- en 3D-Particle Tracking Velocimetry is de beweging van diverse voorwerpen in de vortex gemeten. De experimentele voorwerpen zijn bol- kubus en ellipsvorming met een karakteristieke lengte  $L$  van  $\sim 0.02$  tot  $\sim 0.04$  m en een dichtheid tussen de 600 en 1.000 kg m<sup>-3</sup>. Uit de bijna 700 experimenten volgt dat de beweging kan worden onderverdeeld in twee karakteristieke toestanden: stage 1 betreft de spiraalvormige beweging langs de luchtkern van de vortex en stage 2 betreft de axiale beweging door de vortexkern. Het Reynoldsgetal in stage 1 is  $\sim 10^2 < Re_p < \sim 10^4$  en het Reynoldsgetal voor axiale beweging in stage 2 is  $\sim 10^2 < Re_{p,z} < \sim 6 \cdot 10^3$ . De beweging in stage 1 blijkt te worden bepaald door de initiële snelheid en rotatie van het voorwerp of anders gezegd: het systeem vertoont een chaotisch gedrag. Als voorbeeld dient de beweging van een voorwerp in twee experimenten met identieke hydraulische condities maar met kleine verschillen in initiële condities: in het eerste experiment beweegt het voorwerp zich naar het centrum toe en in het tweede experiment van het centrum af. Dit is een vaak voorkomend gedrag bij niet-lineaire systemen. Om dit gedrag te kwantificeren, is een vereenvoudigd model ontwikkeld. Het model beschrijft de beweging van een voorwerp in het stromingsveld van de vortex. Het chaotische gedrag in zowel de metingen als de modelsimulaties is gekwantificeerd door bepaling van de grootste Lyapunov exponent. De conclusie is dat de beweging van een voorwerp in een vortex een korte voorspellingshorizon heeft. De beweging kan op een kwalitatieve manier worden voorspeld met behulp van faseportretten. Hierbij geldt overigens de kanttekening dat het gelimiteerde voorspelbare gedrag voornamelijk geldt voor bolvormige voorwerpen. Kubus- en ellipsvormige voorwerpen vertonen minder chaotisch gedrag. Er is een parameter opgesteld die een eerste indicatie geeft voor het al dan niet optreden van een continue neerwaartse beweging langs de kern van de vortex.

Het onderzoek naar de stage 2 beweging (axiale beweging door de vortexkern) toont aan dat deze beweging niet kan worden voorspeld met de algemeen toegepaste formule van uniforme sleepkracht en bijbehorende sleepcoëfficiënt  $C_D$ . De sleepkracht op een voorwerp lijkt te worden bepaald door de aanwezigheid van een Taylor-kolom onder het voorwerp. Proudman (1916) en Taylor (1917) ontdekten dat een stijgend bolvormig object in een roterende vloeistof wordt vergezeld door een

omringende en stijgende kolom van vloeistof. Deze kolom is verantwoordelijk voor de axiale sleepkracht op het voorwerp. Aan de hand van deze Taylor-kolom is een conditie geformuleerd die een eerste indicatie geeft voor het optreden van een neerwaartse beweging door de vortexkern.

Om de draaikolk als transportmechanisme in de praktijk te gebruiken, moeten de hydraulische en geometrische condities bekend zijn waarbij de vortex optreedt. Het gebruik van Computational Fluid Dynamics met een één-fase model is geschikt om een indicatie te krijgen of de vortex optreedt. Deze methode is echter niet geschikt voor het verkrijgen van gedetailleerde informatie over de vortex zoals de positie en de intensiteit. Het gebruik van een fysisch schaalmodel heeft dan de voorkeur.



# LIST OF SYMBOLS

$a$	= spatial gradient of axial velocity ( $s^{-1}$ )
$A_N$	= cross-sectional area normal to flow ( $m^2$ )
$A_S$	= particle surface area ( $m^2$ )
$C_A$	= added mass coefficient (-)
$C_D$	= drag coefficient (-)
$C_L$	= lift coefficient (-)
$C_T$	= torque coefficient (-)
$d$	= pipe diameter (m)
$D$	= suction inlet diameter, outlet diameter (m)
$D_S$	= sphere diameter (m)
$g$	= gravitational constant ( $m\ s^{-2}$ )
$h$	= height of plane measured from tank bottom (m)
$H$	= undisturbed water depth above outlet (m)
$H_D$	= total surface depression or air core depth (m)
$I_p$	= particle's moment of inertia ( $kg\ m^2$ )
$k$	= constant, shape correction factor (-)
$L$	= characteristic particle length (m)
$n$	= number of measurement planes (-)
$N$	= number of revolutions (-)
$N_B$	= dimensionless buoyancy parameter (-)
$N_D$	= dimensionless drag parameter (-)
$p$	= pressure ( $N\ m^{-2}$ )
$q$	= flow rate per unit of height ( $m^2\ s^{-1}$ )
$Q$	= flow rate ( $m^3\ s^{-1}$ )
$Q_v$	= vortex flow rate ( $m^3\ s^{-1}$ )
$r$	= radial coordinate (m)
$r_c$	= vortex core radius (m)
$R$	= dimensionless radius (-)
$Re_p$	= particle Reynolds number (-)
$Re_{p,z}$	= particle Reynolds number in axial direction (-)
$Ro$	= Rossby number (-)
$S$	= submergence depth (m)
$t$	= time (s)
$t_a$	= particle travel time (s)

$T$	= characteristic time parameter (s)
$T_a$	= Taylor number (-)
$T_p$	= torque on particle (N m)
$U_o$	= mean suction inlet velocity, mean outlet velocity ( $\text{m s}^{-1}$ )
$\mathbf{U}$	= particle velocity field
$U_r$	= particle radial velocity ( $\text{m s}^{-1}$ )
$U_z$	= particle axial velocity ( $\text{m s}^{-1}$ )
$U_\theta$	= particle tangential velocity ( $\text{m s}^{-1}$ )
$\mathbf{V}$	= flow velocity field
$V_r$	= radial velocity ( $\text{m s}^{-1}$ )
$V_z$	= axial velocity ( $\text{m s}^{-1}$ )
$V_\theta$	= tangential velocity ( $\text{m s}^{-1}$ )
$W_e$	= Weber number (-)
$x$	= x coordinate (m)
$y$	= y coordinate (m)
$\mathbf{X}_{p,0}$	= particle initial conditions field
$z$	= axial coordinate (m)
$\alpha$	= bounding radius (m), width of Gaussian function (-)
$\gamma$	= relative velocity parameter (-)
$\theta$	= azimuthal coordinate (rad)
$\kappa$	= streamline curvature ( $\text{m}^{-1}$ )
$\nu$	= kinematic viscosity ( $\text{m}^2 \text{s}^{-1}$ )
$\nu_{eff}$	= effective kinematic viscosity ( $\text{m}^2 \text{s}^{-1}$ )
$\rho_f$	= fluid density ( $\text{kg m}^{-3}$ )
$\rho_p$	= particle density ( $\text{kg m}^{-3}$ )
$\tau$	= viscous stress ( $\text{N m}^{-2}$ )
$\Gamma$	= circulation ( $\text{m}^2 \text{s}^{-1}$ )
$\Phi$	= velocity potential ( $\text{m}^2 \text{s}^{-1}$ ), motion parameter (-)
$\Phi_T$	= Taylor-drag shape factor (-)
$\chi$	= particle volume ( $\text{m}^3$ )
$\Omega$	= angular velocity ( $\text{rad s}^{-1}$ )
$\Omega_p$	= angular velocity of a rotating particle ( $\text{rad s}^{-1}$ )
$\omega$	= vorticity ( $\text{s}^{-1}$ ).

# 1

## INTRODUCTION

## 1.1 THE WASTEWATER PUMPING STATION

The purpose of urban drainage systems is to protect society from health hazards and flooding of urban areas during storm events. Combined sewer systems consist of lateral house connections, collecting pipes and a WasteWater Pumping Station (hereafter referred to as: WWPS). The collecting pipes transport wastewater and storm water to the WWPS which transports the water to a WasteWater Treatment Plant (WWTP) or another sewer system component. In general, the WWPS consists of a sump and one or more pumps. In the sump, all the water is collected. The pumps or suction inlets are placed in the sump and discharges the water through the pressure main towards a point of release.

### A BRIEF HISTORY OF WWPS DESIGN IN THE NETHERLANDS

The first WWPS were built at the end of the nineteenth century. In the city of Rotterdam, the first pumping station was the ‘Westerlijk Stoomgemaal’ and build in 1891. The station both transported surface water and wastewater by steam engine driven piston pumps. Figure 1 shows some drawings of this historic station that has become a national monument. Around 1910-1920 most pumping stations were built with centrifugal pumps that were driven by electric motors. The motors were started with magnetic switches. To reduce high motor temperatures and extensive wear of the switches, the number of pump-starts was limited to circa 5 starts per hour. Consequently, this requires large water storages between the pump switch-on and switch-off levels. The large sump areas resulted in low flow velocities with a high risk on sedimentation and accumulation of floating solids. These problems were solved by using winding gutters (in Dutch: ‘slingergoten’), see Figure 1.2. The high flow velocities in the gutter transports the solids to the pump suction inlets. The high velocities were obtained by setting the pump switch-off level lower that the bottom level of the gutter.

Around the 1970ss, the electric 3-phase motors are controlled by variable frequency drives. The use of these frequency drives increased the maximum number of pump-starts to 10 to 20 starts per hour. Consequently, the required sump area could be much smaller. In modern times and for the WWPS in the city of Rotterdam, electric motors  $> \sim 4$  kW are controlled by frequency drives.

## 1.2 PROBLEMS WITH FLOATING SOLIDS IN PUMP SUMPS

In the Netherlands, and most likely also in urban areas of most other countries, the sumps of WWPS are often covered with floating particles of Fat, Oil and Grease (FOG) and other floating trash (hereafter referred to as: floating solids). The formation

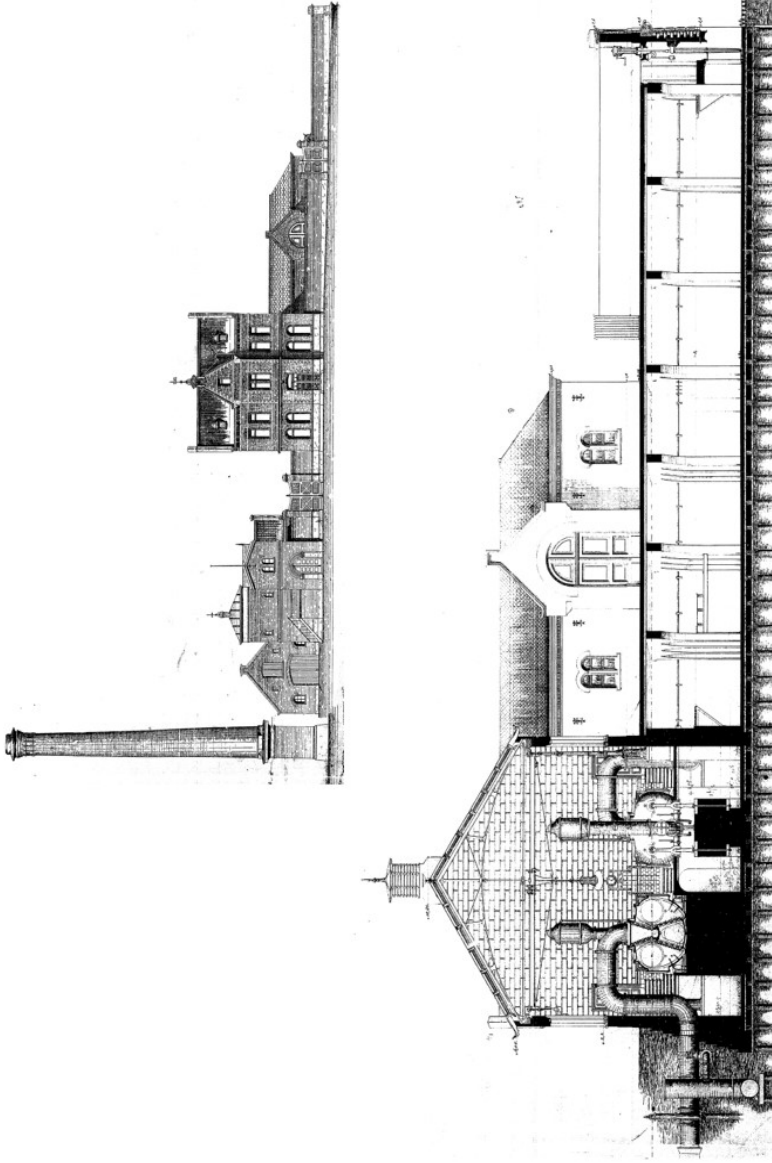


Figure 1.1: WWPS Westelijk Stoomgemaal and one of the first WWPS in the Netherlands, built in 1860. This station discharges surface water and wastewater at the same time. The piston pumps are driven by steam engines. In 1930, the pumps were replaced by electric driven centrifugal pumps.

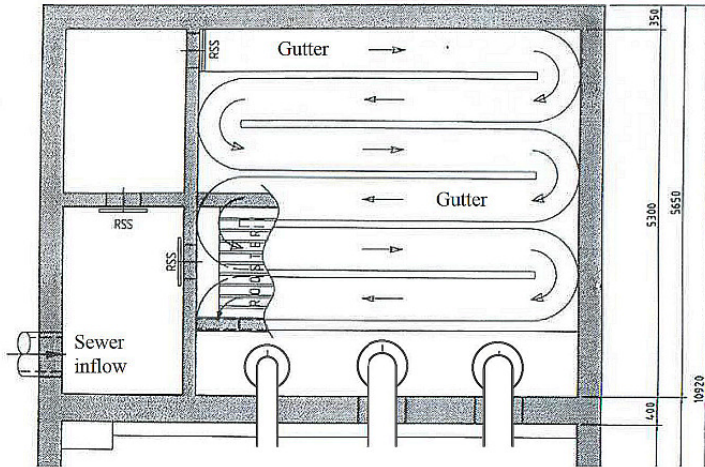


Figure 1.2: Top view of the sump of WWPS Rozenburg. The winding gutter transports floating solids towards the pump suction inlets. The high flow velocities in the gutter were obtained by setting the pump switch-off level lower than the gutter bottom level.

of the FOG particles is assumed to occur in the sewer lines and in the lateral house connections and not in the sump itself. As observed in various Dutch WWPS, the particles have a typical diameter size of 0.01 to 0.2 m. The mechanisms that forms the particles is appeared to be a complex combination of various processes e.g. the saponification process between calcium and free fatty acids amongst other processes (Nieuwenhuis *et al.*, 2018). The source of the fatty acids and calcium are the disposals of cooking oils and fats into the kitchen drains, soaps from showering and washing machines. Due to stagnant water areas in the sump or other (hydraulic) conditions that decelerates the (suspended) motion of floating solids, the solids can clump into larger pieces. The larger pieces can accumulate to form a closed layer that covers the total sump area. Figure 1.3 shows the accumulation of small particles to a closed layer. In time, the layers can grow in thickness to a massive floating package. For a specific pump sump in the Netherlands a floating layer was grown in thickness to a height of  $\sim 2$  m within a period of  $\sim 1$  year, see Figure 1.4. The presence of floating solids is a source of various problems:

1. Larger pieces due to clumping of smaller particles can clog the pump impellers which results in a pump failure. During storm events this failure decreases the serviceability of the sewer-system. For a specific case study, the pump failures results in a 16% increase of yearly volume of combined sewer overflows as shown by Korving *et al.* (2006).

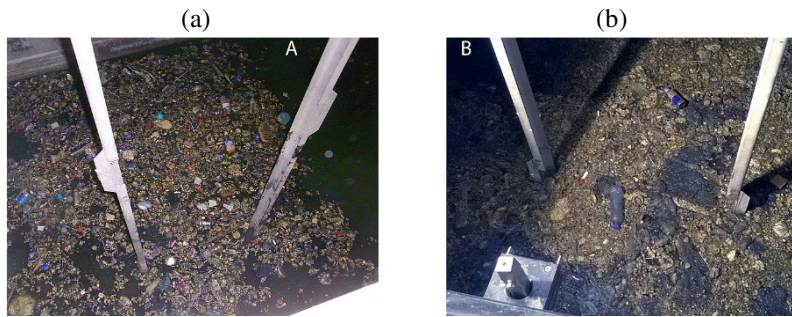


Figure 1.3: Evolution of floating solids in a pump sump (WWPS Amelandseplein, Rotterdam, The Netherlands). (a) Initially, the solids consists of individual particles. (b) During time the solids accumulate to a closed stiff layer that covers the total sump area.

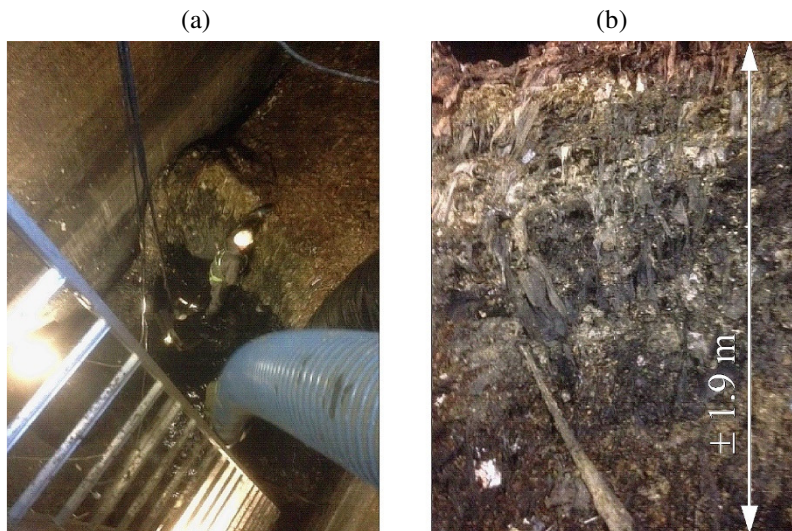


Figure 1.4: (a) Maintenance worker removing a closed stiff floating layer of accumulated floating solids in the pump sump of a WWPS located in Rotterdam. (b) Detail of the floating layer. The layer has a height of  $\sim 2 \text{ m}$ .

2. The particles can accumulate to closed stiff layers. These layers are periodically removed by the maintenance workers with high labour costs. For example, for the municipality of Rotterdam, the annual cost to remove dash is about € 300.000,-. For The Netherlands, the annual costs for pump maintenance and remove dash is estimated to several millions of euros.
3. The removal of the closed stiff layers is a labour intensive, dangerous and unhygienic job.

Consequently, the accumulation and agglomeration of floating solids in closed stiff layers should be avoided or reduced to a minimum.

### 1.3 SUMP DESIGN FOR TRANSPORT OF FLOATING SOLIDS

As introduced in the former section, the small floating solids must be removed by the pumps before they can accumulate to floating layers. Once the layer is formed, it is very difficult removing the layer by pumps. Consequently, the sump must be designed to be able to remove the solids by the pumps. This section addresses a brief review of the guidelines for sump design with respect to the removal of floating solids. This section also addresses a brief introduction on the application of kinetic energy for removal of floating solids.

#### 1.3.1 REVIEW OF CURRENT GUIDELINES WITH RESPECT TO REMOVAL OF FLOATING SOLIDS

In general, the current, widely accepted, guidelines for pump sump design (e.g. ANSI/HI, 2012) focusses on providing optimal hydraulic conditions in the pump sump. Optimal hydraulic conditions, and only verified for clean water sumps, includes:

1. Low flow velocities;
2. a high submergence depth to avoid air entrainment by vortices and;
3. no air entraining by falling water jets.

However, applying these conditions may even result in an increase of floating solids. For example: to prevent strong air entraining vortices, the ANSI/HI (2012) recommends a minimum submergence depth  $S$  of:

$$S = D_b \left( 1 + 2.3 \frac{U_0}{\sqrt{gD_b}} \right) \quad (1.1)$$

with  $D_b$  the outside diameter of the suction inlet. In practice, this design recommendation leads to low fluid surface velocities that has a positive influence on the accumulation of the solids to closed layers. In the Netherlands, the recommended submergence depth is often reduced (even up to 50%) to ensure an increase in surface flow velocities. The occurrence of strong, or even weak, vortices is very rare in wastewater sumps at a significant smaller  $S$ . Therefore, the advised ANSI/HI submergence depth seems very conservative for wastewater pump sumps.

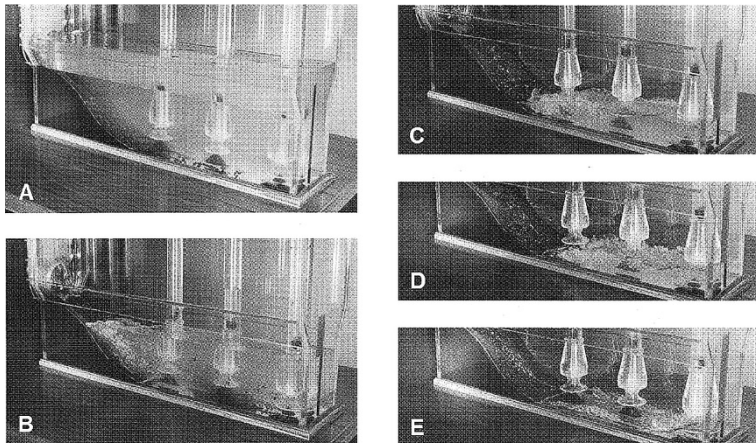


Figure 1.5: Scale model of trench type sump to test the transport ability of the pump-down (Pump Station Design, 2008). The lowering of the water level beneath the inlet conduit introduces a hydraulic jump (Figure B) that mixes the floating solids to a homogeneous mixture. By continuing lowering the water level, the jump moves towards the downstream inlet transporting the mixture to the suction inlet (Figure C to E).

The current guidelines only deal in a superficial manner with the transport of (small) floating solids and for a limited number of sump geometries only: (1) the trench-type sumps (Figure 1.5) and (2) circular sumps. The ANSI/HI (2012) recommends the application of trench-type sumps with a ramp. Trench-type sumps are frequently used in the USA. The transport of floating solids, called as ‘cleaning procedure’, is conducted by a pump-down that introduces a forced water jump providing a mixing of the floating solids to a homogeneous mixture which is transported into the suction inlet by the horizontal velocity component. Figure 1.5 shows a scale model that simulates the introduction of the hydraulic jump by pump-down which must transport the solids towards the suction inlet (Pump Station Design, 2008). For the transport of floating solids in circular (wet) sumps, the ANSI/HI (2012) recommends a periodic cleaning procedure by lowering the submergence depth  $S$  to  $0.5$  to  $1.0D_b$  to create a strong free-surface vortex (type 4 to 6, see Figure 1.6) which transports the floating solids to the suction inlet. The transport of the solids will take some time, so the procedure can only be successful when enough inflow of wastewater is feasible.

### 1.3.2 THE ‘NO-SUMP’ PRINCIPLE

In the Netherlands pump stations are applied without a storage sump. The pump discharges directly from the gravity sewer. Because of the variable amount of inflowing wastewater, the pump discharge is controlled by the amount of inflowing wastewater.

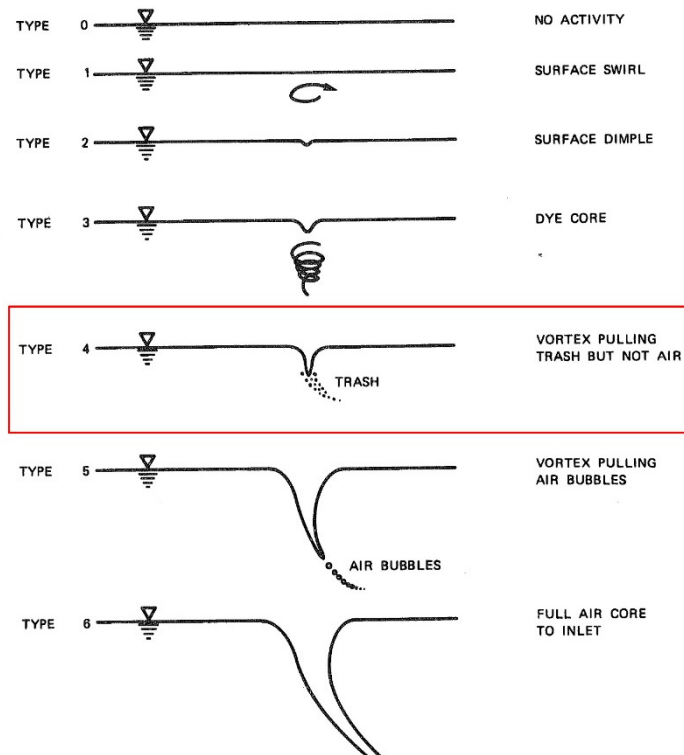


Figure 1.6: Strength classification of types of free-surface vortices (Rindels, 1983). Type 4 is assumed as the required minimum for transport of floating trash. This type only transports floating trash without the entrainment of air.

Because there is no sump, there is also no formation of floating layer in this sump (Stichting Toegepast Onderzoek Waterbeheer, 2012). However, the system only operates successful when there is a constant and sufficient amount inflowing wastewater which makes the system difficult not control. As there is less literature on the reliability of this system, the system is not discussed in detail in this thesis.

### 1.3.3 TRANSPORT OF FOG BY KINETIC ENERGY

Nieuwenhuis *et al.* (2019) studied the correlation between the occurrence of floating solids in the sumps and the kinetic energy per unit volume wastewater per day amongst various other parameters. The study uses data of 126 WWPS located in five Dutch municipalities. The kinetic energy is defined as the sum of the momentum of the inflowing wastewater and the potential energy of the inflowing wastewater with respect to the water level in the sump. The study provides a new insight in the probability of solids accumulation and the kinetic energy density. The study showed a negative correlation between higher kinetic density and the presence of floating

solids in the sump. This can be an indication that higher kinetic energy forces or holds particles in suspension that increases the probability of transport towards the pump suction inlet.

## 1.4 PROBLEM DEFINITION

The cleaning procedure for both trench-type and circular sumps temporally subjects the pumps to vibration, dry running, air entrainment and other severe conditions. It is obvious that this method of removal of floating solids must be conducted with great care without damaging pumps and, very important, a limited entrainment of air. Especially in the Netherlands, pump pressure mains can include many downward slopes that are subject to air pocket formation causing energy losses. In the Netherlands, and according to the authors knowledge, trench type sumps with ramps and/or the described cleaning procedure are seldom used. Furthermore, the ‘no-sump’ system is rarely used due to a lack of published literature on its reliability. Consequently, and also due to the heritage of the very large sumps from the past (see section 1.2), many WWPS in the Netherlands (and probably all over the world) experience problems with the removal of floating solids.

## 1.5 RESEARCH QUESTIONS

As addressed in the former section, in many sumps of WWPS, there is no downward motion of floating solids from the water surface towards the pump suction inlet. To solve this problem of floating solids, two methods are thought as potentially effective. The first method uses the kinetic energy of the fluid in the sump i.e. increasing the turbulent motion of the fluid keeping solids in suspension, see section 1.3.3. The second method is the application of a free-surface vortex for the downward transport of floating solids towards the suction inlet. The goal of this thesis is to study the potential of the vortex as an effective mean for the downward motion of floating solids. In conclusion, the research question to be answered in this thesis is: “what is the potential of a free-surface vortex as a mean for the downward motion of buoyant particles?”

## 1.6 RESEARCH STRUCTURE

To study the potential of the free-surface vortex as a mean for the downward motion of buoyant particles, there is need for knowledge on the free-surface vortex 3D-flow field. Furthermore, as air entrainment by an air core that extends into the pump must be prevented in the practical application of the free-surface vortex (vortex type 6, see Figure 1.6), there is a need for a reliable quantification of the air core depth  $H_D$ . Hence,

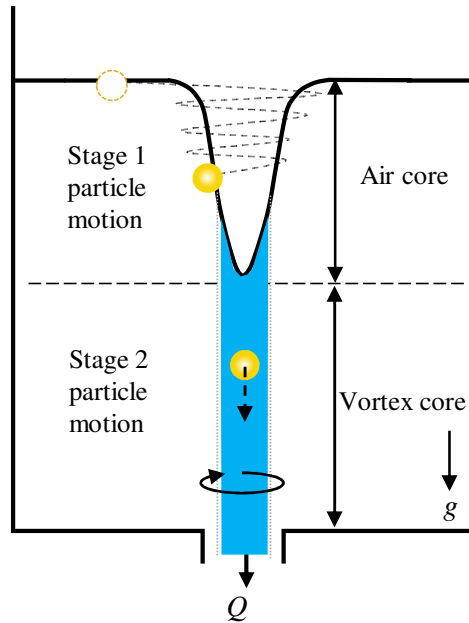


Figure 1.7: Definition of the observed stages in the free-surface vortex driven motion of buoyant particles. The stage 1 motion is the helical motion along the air core. The stage 2 motion is the axial motion through the vortex core.

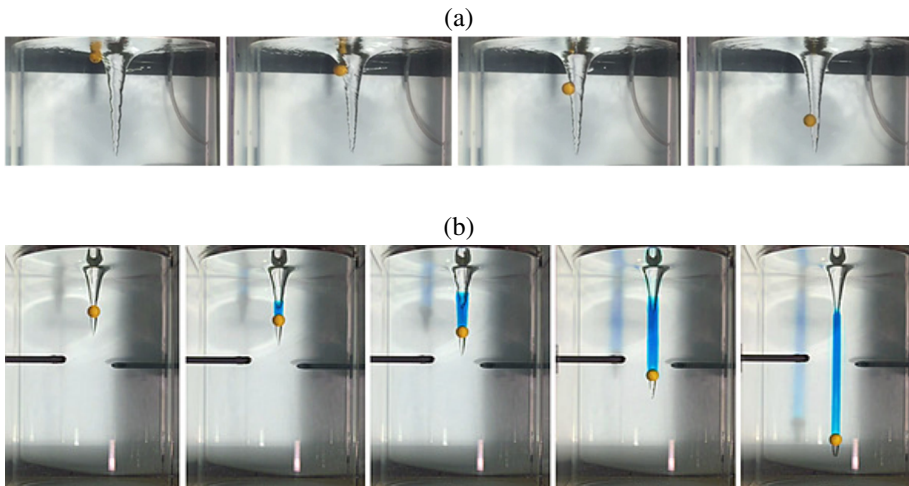


Figure 1.8: Free-surface vortex driven motion of a 38 mm buoyant sphere. (a) Stage 1 particle motion. (b) Stage 2 particle motion.

the first step in this research was to obtain data on this 3D-flow field and to validate a mathematical vortex model that predicts  $H_D$  using characteristic parameters. This data is obtained by an extensive experimental research on the vortex characteristics using an  $\varnothing 600$  mm vortex tank at the Deltares hydraulic laboratory. The flow velocities are measured by applying Stereo Particle Image Velocimetry (SPIV). The experimental program and results of this research are presented in Chapter 3.

The next step is to study the dynamics between particles and the free-surface vortex flow and to obtain conditions that provides a downward particle motion as function of the vortex and particle characteristics. Preliminary experiments in the vortex tank revealed two distinct stages in the vortex flow driven motion of buoyant particles, see Figure 1.7 and Figure 1.8. Stage 1 is characterized by the particle following a helical motion along the vortex air core until the particle reaches the air core bottom where the particle centralizes in the vortex core. During the helical motion, the particle may be ejected out of the air core or reaches a more or less stable orbit around the vortex air core at some specific height. Stage 2 motion is the axial motion through the vortex core where the particle is centralized in the core. In this stage the particle either shows a continuous downward axial motion towards the outlet, see Figure 1.8(b), or the particle remains in position at the air core bottom. By using the vortex tank and applying 2D and 3D-Particle Tracking Velocimetry (hereafter referred to as 2D-PTV and 3D-PTV respectively), the particle motion in both stages is studied and conditions are examined that provides particle motion as function of the vortex and particle characteristics. The experimental research on the stage 1 motion is addressed in Chapter 4. The experimental research on the stage 2 motion is addressed in Chapter 5.

To conclude this thesis, Chapter 6 addresses the conclusions and the recommendations including a part on the engineering aspects of using Computational Fluid Dynamics as simulation tool for free-surface vortices.



# 2

## EXPERIMENTAL SET-UP AND MEASURING TECHNIQUES

The major content of this chapter is based on the published articles:

- i. Duinmeijer, S.P.A. et al. (2019a). *A Simple measuring set-up for the experimental determination of the dynamics of a large particle in the 3D velocity field around a free-surface vortex*. Journal of Flow Measurement and Instrumentation, doi.org/10.1016/j.flowmeasinst.2018.10.007;
- ii. Duinmeijer, S.P.A., Oldenziel, G. & Clemens, F.H.L.R. (2019b). *Experimental study on the 3D-flow field of a free-surface vortex using stereo PIV*. Journal of Hydraulic Research, DOI: 10.1080/00221686.2018.1555558.

## 2.1 INTRODUCTION

In this chapter the following issues are presented:

1. The set-up of the vortex tank;
2. the set-up of the 2D/3D Particle Tracking Velocimetry and;
3. the set-up of the Stereo Particle Image Velocimetry (SPIV).

## 2.2 THE VORTEX TANK SET-UP

The experimental set-up consists of a cylindrical acrylate (PMMA) tank with an inside diameter of  $\sim 0.6$  m and a height of  $\sim 1$  m, see Figure 2.1 and Table 2.1. The tank is placed in a square  $\sim 0.7 \times 0.7 \times 1.0$  m acrylate container filled with water to reduce the effects of light refraction when recording camera images. The setup is a closed loop system with a pump discharging water in the tank that flows through an outlet in the bottom back to the pump. Two outlet pipe diameters ( $D = 0.030$  m and  $0.044$  m) enable the variation the vortex characteristics by changing the mean outlet velocity  $U_o = 4Q/\pi D^2$ . The uncertainty in  $U_o$  is determined to be  $\pm 0.01$  m s<sup>-1</sup>. The transition between tank bottom and outlet is curved to minimize flow separation and at the same time avoiding an error in the calculation of  $U_o$ . A particle separation tank of  $0.30 \times 0.30 \times 0.40$  m is placed between the tank outlet and the pump suction side for separating experimental floating particles from the closed system, see Figure 2.2(c). The flow enters the tank through two horizontal  $\text{Ø}25.9 \times 1.9$  mm inlet pipes mounted flush in the tank wall placed  $0.5$  m above the tank bottom, see Figure 2.2(a). During the experiments, the water temperature is measured and was found to vary between  $22$  and  $28$  °C, influencing the physical properties of water such as viscosity and surface tension. For the 3D-PTV experiments, the experimental particles were released on a fixed position with a particle release device build with LEGO® components, see Figure 2.2(d).

### 2.2.1 VORTEX TANK MEASURING TECHNIQUES

#### FLOW CIRCULATION

The (bulk)circulation  $\Gamma$ , which is an important vortex characteristic as discussed in chapter 3, is determined with a floating quadripod. This device consists of four egg shaped floaters connected to a  $0.30$  m cross shaped frame of  $3$  mm diameter aluminium rods, see Figure 2.2(b). The frame center was connected to a vertical aluminium rod to centre the quadripod above the tank. This method was also applied by e.g. Brocard *et al.* (1983) and Echávez and McCann (2002). The method is based on the Stokes' theorem saying that the bulk circulation  $\Gamma_\infty$  is the integral of the axial

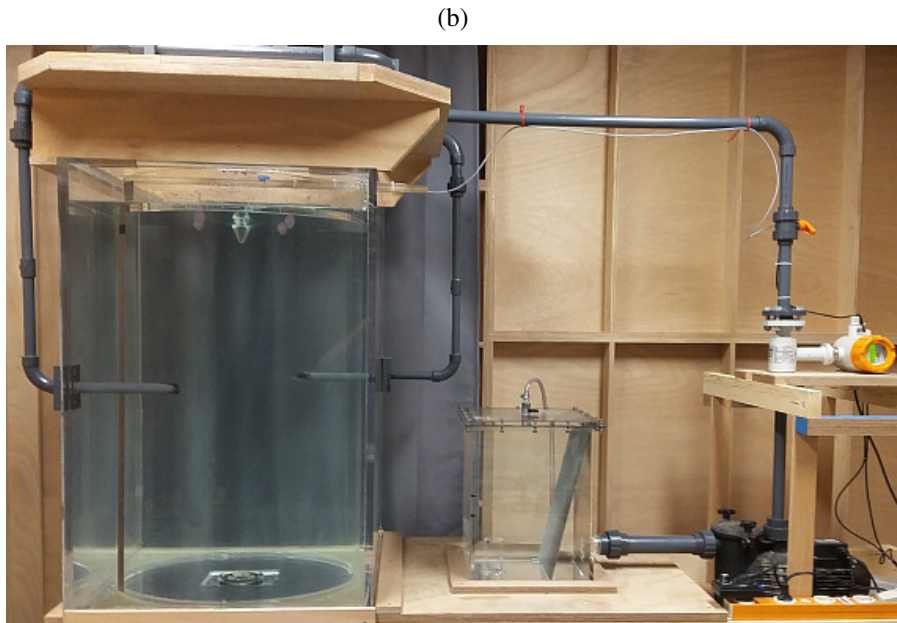
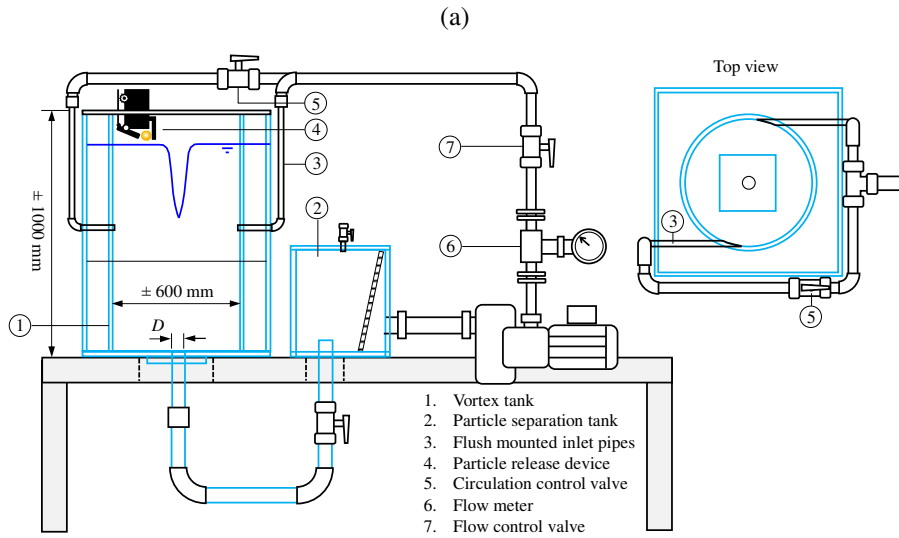


Figure 2.1: (a) Schematic overview of the experimental set-up. (b) Photo experimental set-up.

Table 2.1: Dimensions of the vortex tank and their uncertainties based on 20 repeated measurements.

Dimension	Mean value (mm)	95% uncertainty interval (mm)
Width ( $x$ -direction)	698.77	697.99 to 699.55
Depth ( $y$ -direction)	699.15	696.9 to 701.4
Thickness ( $x, z$ ) wall	19.29	18.63 to 19.95
Thickness ( $y, z$ ) wall	19.29	18.63 to 19.95
Thickness cylinder's wall	7.97	7.80 to 8.14
Diameter cylinder (internal)	609.82	608.66 to 610.98

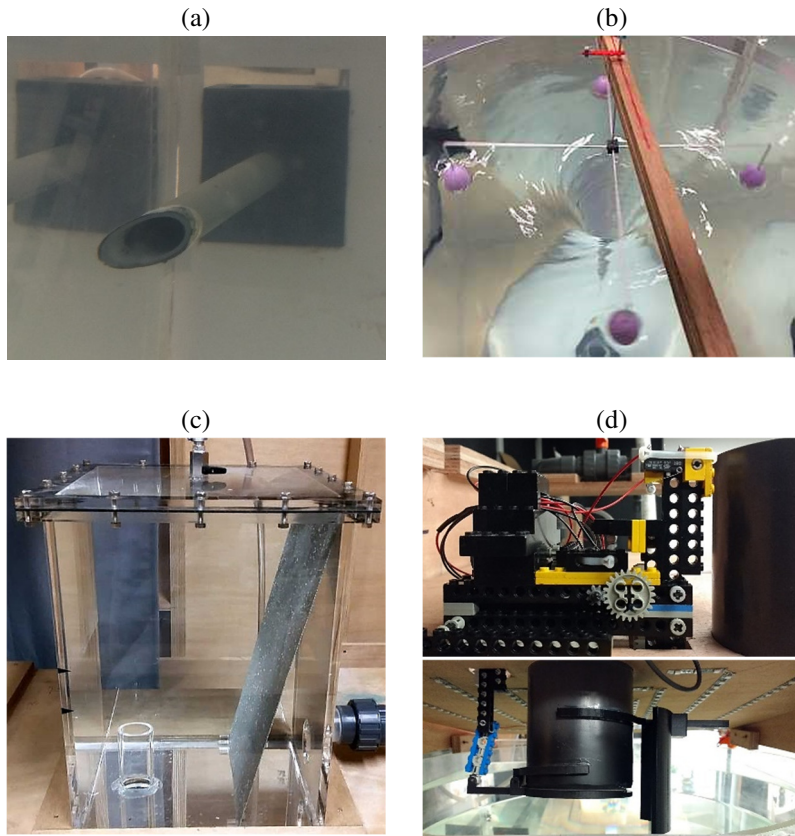


Figure 2.2: Details of the experimental set-up. (a)  $\text{Ø}25.9 \times 1.9$  mm inlet pipe. The pipe is flush mounted to have a minimum disturbance of the flow field. (b) Floating quadripod for measuring the flow circulation. (c) Particle separation tank. (d) Particle release device for the particle release on a fixed position at the water free-surface.

vorticity  $\omega_z$  across the cross-sectional area of the tank and equal to the line integral of the tangential velocity  $V_\theta$  around a closed circle  $C$  with radius  $r$  enclosing the vortex area. The circulation  $\Gamma$  is determined by measuring  $V_\theta$  around a circle with diameter  $d$ :

$$\Gamma = \oint_C \mathbf{V} ds = 2\pi r V_\theta = \pi^2 d^2 N t^{-1} \quad (2.1)$$

with  $d = 0.3$  m the length of the quadripod and  $t$  the measured time to accomplish  $N$  revolutions. The revolution rate  $N/t$  of the quadripod was recorded using a stopwatch. The measurement of  $\Gamma$  is done at a distance of  $r = 0.15$  m which is equal to  $\sim 8r_c$  and thus larger than  $3r_c$  which is assumed to be the minimum to measure the bulk circulation  $\Gamma_\infty$  (Suerich-Gulick *et al.*, 2014a).

#### FLOW RATE

The flow rate  $Q$  is measured with a Kobold type DMH Magnetic-Inductive Flow meter (calibrated prior to the experiments, the average deviation was determined to be 2%) located in the pressure line at a distance  $> 10d$  from any pipe components with  $d$  the component diameter.

#### AIR CORE DEPTH

The depth of the air core  $H_D$  is measured using a stylus placed in the center of the air core with an estimated uncertainty of  $\pm 0.005$  m for series 1 to 3,  $\pm 0.01$  m for series 4 to 6 and  $\pm 0.02$  m for series 7 to 8. The uncertainty of this measurement is largely due to the oscillating behavior of the air core depth and the water free-surface.

### 2.2.2 UNCERTAINTY ANALYSIS

The measured parameters are used to calculate model results and comparing them with experimental results. Hence, the model confidence interval  $\delta H_{D,model}$  must be known. The measuring accuracy of the flow meter is  $\pm 0.3\%$  of the actual value +  $0.0001Q$  at  $10 \text{ m s}^{-1}$ . Based on the DN25 diameter, the total accuracy is then  $\pm(0.003Q + 0.0018) \text{ m}^3 \text{ h}^{-1}$ . During experiments the measured flow rate fluctuates with a deviation of about  $0.02 \text{ m}^3 \text{ h}^{-1}$ . This deviation is included in the uncertainty calculation giving a maximal total uncertainty of  $\delta Q = \pm(0.003Q + 0.02) \text{ m}^3 \text{ h}^{-1}$ . The (undisturbed) water depth  $H$  is measured with a rule and the uncertainty in reading the rule is defined as  $0.002$  m. However, due to the presence of the volume of the aircore, the water depth will increase because of conservation of mass. From initial experiments the maximum variation is about  $0.01$  m. This value is much higher than the rule uncertainty and thus defined as the uncertainty  $\delta H$ . The diameter  $D$  is a constant parameter with a defined uncertainty  $\delta D = 0.001$  m.

Table 2.2: Uncertainties in measured parameters.

Parameter	Symbol	Measuring method	Uncertainty
Flow rate	$Q$	Flow meter	$\delta Q = \pm(0.003Q + 0.02 \text{ m}^3 \text{ h}^{-1})$
Air core depth	$H_D$	Stylus	$\delta H_D = \pm 0.005 \text{ to } 0.02 \text{ m}$
Circulation	$\Gamma$	Floating quadripod	$\delta \Gamma = \pm 0.04\Gamma$
Water depth	$H$	Ruler	$\delta H = \pm 0.01 \text{ m}$

Uncertainties in the calculation of  $\Gamma$  are introduced by inaccuracies in the quadripod length  $d$  and the time registration  $t$  by stopping the stopwatch. The first is defined as  $\delta d = 0.002 \text{ m}$  and the latter by some tests as  $\delta t = 0.5 \text{ s}$ . By applying the theory of error propagation on equation (2.1) and assuming the uncertainties being Gaussian distributed and the constituents being mutually independent, the uncertainty  $\delta \Gamma$  is expressed as:

$$\delta \Gamma = \sqrt{\left(\left|\frac{\partial \Gamma}{\partial d}\right| \delta d\right)^2 + \left(\left|\frac{\partial \Gamma}{\partial t}\right| \delta t\right)^2} = \Gamma \sqrt{0.0002 + \frac{0.25}{t^2}} \quad (2.2)$$

Each  $\Gamma$  is calculated by  $N = 5$  with a lowest measured total time  $t$  of  $\sim 15 \text{ s}$ . By applying equation (2.2) the uncertainty in  $\Gamma$  is simplified to a maximum of  $\sim 0.04\Gamma$ . Table 2.2 shows an overview of the uncertainties of the measured parameters.

In the calculations of the flow quantities the uncertainty is expressed by applying the 95% confidence interval given by  $\pm 2\sigma$ .

### 2.2.3 INFLUENCE OF SCALE EFFECTS

The order of magnitude of the dimensions of the set-up are roughly similar to sumps of real WWPS (the majority of the WWPS in the Netherlands are relatively small). Therefore, scale effects when translating the presented results to the application of vortices in real sumps are considered of minor importance.

## 2.3 PARTICLE TRACKING VELOCIMETRY

### 2.3.1 SET-UP

The 3D motion of particles has been recorded using two groups of three cameras each (Figure 2.3) placed on two perpendicular sides of the tank. Each set consists of three cameras (two iPhone 6 and one iPhone 5s) and are positioned parallel to the tank's outer walls at a distance of  $\sim 1.7 \text{ m}$ . The cameras are placed in a triangular 3D printed setup, spaced  $0.14 \text{ m}$  horizontally and  $0.14 \text{ m}$  vertically. This setup is chosen because

when the particle is behind the air core for one set of cameras it can still be observed by the second set. The iPhones are operated in slow motion mode implying a frame rate of ~120 (iPhone 5s) and ~240 (iPhone 6) fps. Experiments with external visible light sources proved to be prone to errors due to reflections of the light in the air-water and water-acrylate interfaces. Suppressing these reflections effectively proved to be beyond possibility. In order to minimise reflections, the particles were painted with fluorescent paint, the set-up was placed in a dark room and the particles were subjected to UV light (395 nm wavelength) generated from UV-LED strips. This stimulated the paint to emit light in a specific colour range (495 to 570 nm wavelength). Due to the fact that the particles behave as a light source, reflections were reduced to a minimum, increasing the data yield when compared to working with an external light source.

The presented 3D-PTV method consists mainly of two sub-methods: the first sub-method is a software-program that calculates the 2D positions of the experimental particle in both camera set-up reference systems including accurate synchronization between the 6 cameras of both set-ups. The second sub-method is a software-program that converts the 2D positions of the 6 cameras into 3D positions of the particle. Section 2.3.3 addresses the method of camera calibration. Determination of the 2D and 3D positioning methods are addressed in section 2.3.4. Section 2.3.5 addresses the determination of the breaking indices on the air/acrylate and acrylate/water interfaces.

### **2.3.2 CONTROL SOFTWARE AND SQL DATABASE**

The 3D-PTV method is software controlled (Servoy™ driven) that stores all the input in an SQL database and allows for entering experimental conditions, controls the data-acquisition from the iPhone camera's, controls the post processing of the raw data by addressing compiled Matlab® scripts and stores the results. The PostgreSQL database allows for a quick and flexible access to the experimental results and hence accelerates the analysis of the results.

### **2.3.3 CAMERA CALIBRATION**

In order to compensate for lens distortion and skewness of the recorded images, each individual camera was calibrated using the method proposed and described by Heikkila & Silvén (1997), the camera calibration application provided by Matlab® 2017a was applied. An aluminium calibration plate with a black and white checkerboard pattern of  $0.02 \times 0.02$  m covering the whole field of view was applied to this end. For camera calibration a pinhole camera model 1 is applied:

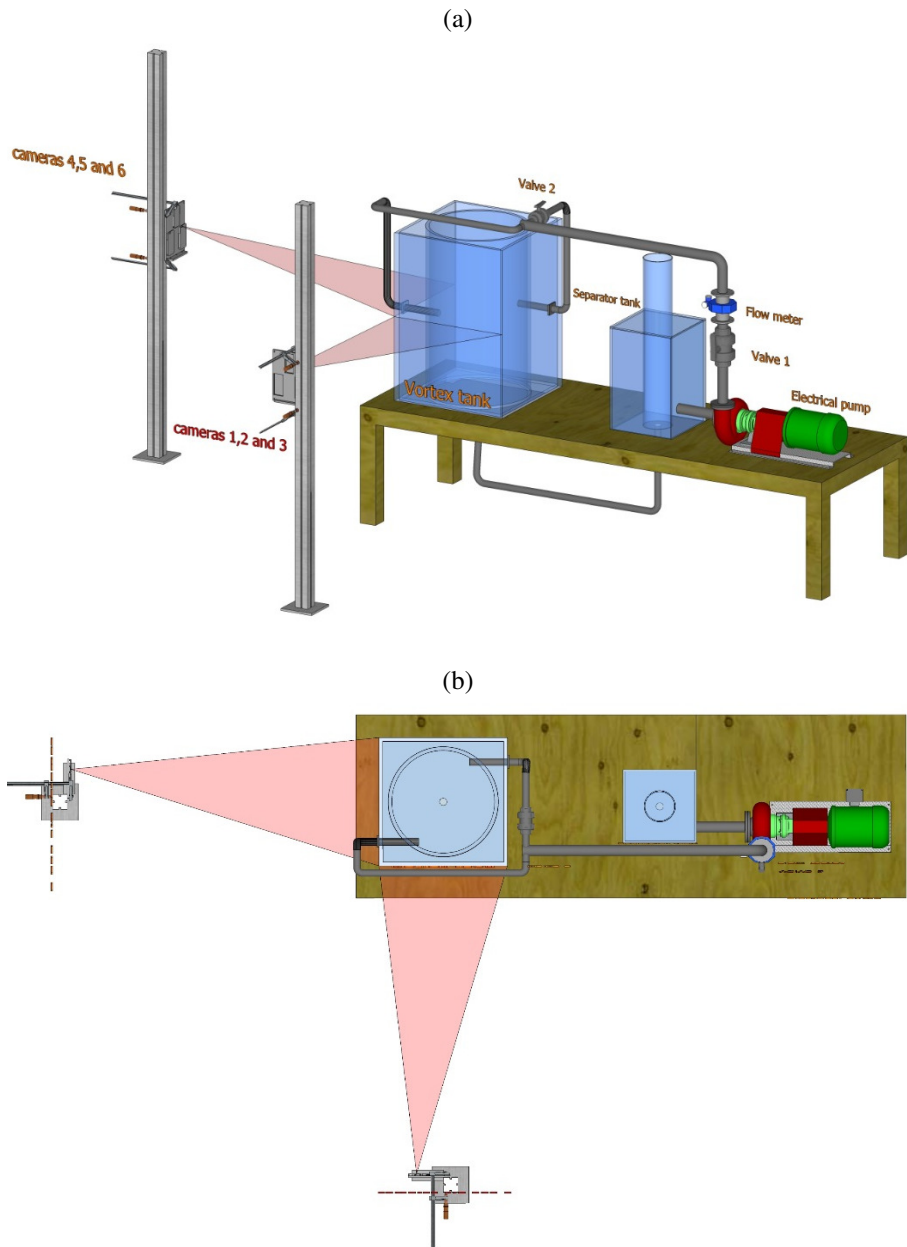


Figure 2.3: (a) Schematic overview of the 3D-PTV set-up consisting of 2 sets of 3 cameras. (b) Top view of the 3D-PTV set-up.

$$w \begin{bmatrix} x \\ y \\ 1 \end{bmatrix} = \begin{bmatrix} X & Y & Z & 1 \end{bmatrix} \begin{bmatrix} R \\ T \end{bmatrix} K \quad (2.3)$$

where  $X, Y, Z$  are world coordinates of a point,  $x, y$  are the pixel coordinates of the corresponding image,  $R$  is the 3D rotation matrix of the camera,  $T$  is the translation vector of the camera relative to the world coordinate system and  $w$  is a homogeneous coordinate scale factor. The model plane is on  $Z = 0$  of the world coordinate system. While  $K$  is the camera intrinsic matrix defined as:

$$K = \begin{bmatrix} f_x & 0 & 0 \\ s & f_y & 0 \\ c_x & c_y & 1 \end{bmatrix} \quad (2.4)$$

where coordinates  $c_x$  and  $c_y$  represent the principal point of the camera in pixel coordinates. The skew factor is defined as:  $s = f_y \tan(\alpha)$  in which  $\alpha$  is the angle between the  $y$ -axis and an axis orthogonal on the  $x$ -axis. The parameters  $f_x = F \cdot s_x$  and  $f_y = F \cdot s_y$  represent the focal length in terms of pixels, where  $s_x$  and  $s_y$  are the number of pixels per world unit in the  $x$ - and  $y$ -direction respectively and  $F$  is the focal length in terms of distance. The distorted points  $x_{distorted}$ ,  $y_{distorted}$  and their radial and tangential distortion coefficients of the lens are denoted as  $k_1, k_2, k_3, p_1, p_2$ :

$$\begin{cases} x_{distorted} = x(1 + k_1 r^2 + k_2 r^4 + k_3 r^6) \\ y_{distorted} = y(1 + k_1 r^2 + k_2 r^4 + k_3 r^6) \end{cases} \quad (2.5)$$

where  $x$  and  $y$  are undistorted pixel locations,  $x_{distorted}$  and  $y_{distorted}$  are distorted pixel locations,  $r^2 = x^2 + y^2$ ,  $k_1, k_2$  and  $k_3$  are the radial distortion coefficients of the lens and  $p_1$  and  $p_2$  are the tangential ones.

### 2.3.4 RECONSTRUCTION OF THE 2D-POSITIONS OF THE PARTICLE FROM THE CAMERA IMAGES

A tracker program (a Matlab® script) detects the particle position from the raw footages and stores the results in the SQL database. Before storage, all six image frames were undistorted following the lens-camera model as previously discussed. Figure 2.4(a) shows the pseudo code description of this method. The detection of the particle was performed based on colour filtering since the particle was selected to be distinguishable from the background. To facilitate colour segmentation, the RGB original frames were converted to an HSV colour space. HSV is a cylindrical colour space, which presents a hue dimension (H) orthogonal to the dominant colour perceived by the observer. This simplifies the filtering of shades of same colour as

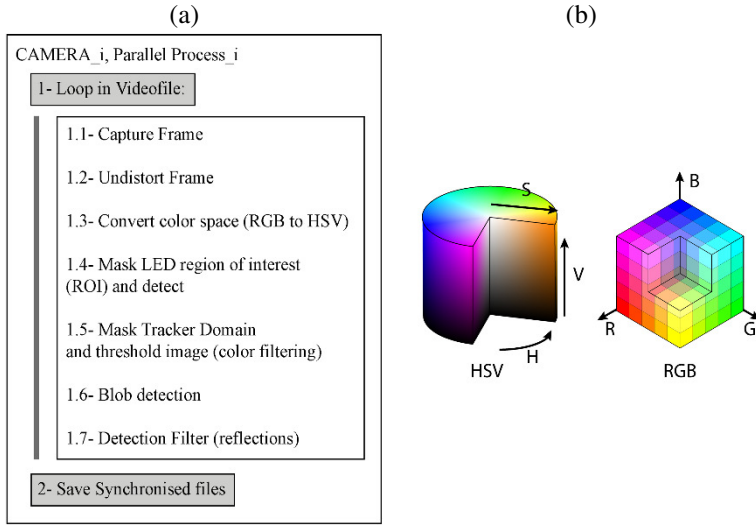


Figure 2.4: (a) 2D detector pseudo code. (b) Parametric colour spaces (RGB vs HSV).

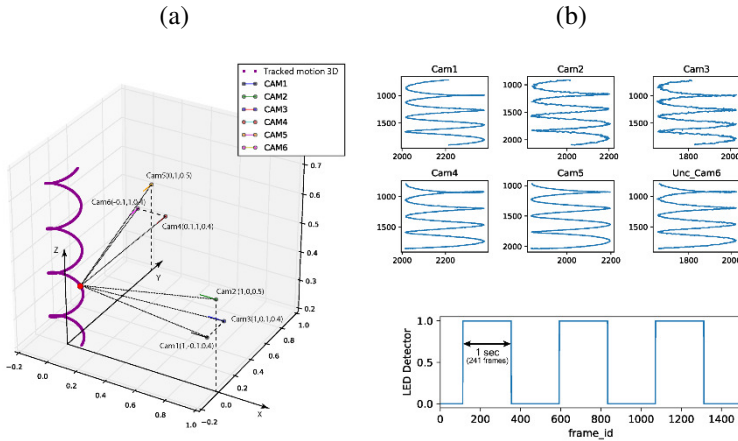


Figure 2.5: Schematic presentation of the 3D and 2D reconstruction and the synchronisation method applied. (a) 3D reconstruction. (b) Top: 2D position in Local Camera Ref System. Bottom: Synchronisation LED (cam 1).

opposed by the RGB description in which a 3D filter should be necessary. Figure 2.4(b) illustrates this difference.

The water-air interface at the free-surface of the vortex tank generated spurious reflections of the particle that conflicted with the tracking algorithm creating uncontrolled “phantom” movements. A motion filter was created to circumvent this.

Initially, a Kalman filter scheme was used without success. The final algorithm relayed in a memory-based filter, in which the next position of the reflection is firstly searched in the direct surroundings of a collection of previous locations. This successfully filtered most of the spurious reflections at the individual camera tracker. Very small differences and variation in time were expected in the framerate of the 6 cameras. This is due to possible differences in internal processing activity or due to differences in the manufacturing process. However, these deviations in frame rate are added over time and can lead to a time-shift in the data stream. Therefore, a temporal synchronization scheme is used to merge the data provided by the individual projection at each camera-frame. This allowed to: (a) eliminate eventual time-shifts, (b) provide a common initial time reference and (c) merge cameras at different frame-rates (e.g. 120 and 240 fps as in this case). To this end an Arduino®-controlled high power LED is mounted to the set-up in such a manner that it is visible for all cameras. The LED is switched on/off at a sequence of 1 s. The LED light was detected by the software by searching for bright pixels (above a tuned threshold) in a user-predefined region of interest in each image. The LED status was recorded along with the calculated variables at each frame. By knowing the LED-blinking pattern frequency and by counting the cycles per camera, a global dynamic time reference was obtained. Figure 2.5 shows schematically the 3D (a) and 2D (b) reconstruction method as well as the synchronization method. The 2D-3D conversion program (Matlab® script) takes the 2D location of the particle projected at each of the 6 camera frames and translates them into 15 estimates of the particle 3D position per video frame and stores the results, along with uncertainties, in the SQL database. From the known camera positions and the observed images in the vortex tank outer wall's plane, a ray-tracing technique has been applied to reconstruct the path of the light from the particle to the camera taking into account the changes in direction due to multiple breaking of the light on the air-acrylate and water-acrylate interfaces. The 3D position at each timestep is determined by triangulation. Details of this technique are described in Appendix A.

### 2.3.5 DETERMINING THE REFRACTION INDICES

The refraction indices of water and acrylate vary with the wavelength of the light and the temperature; the latter was recorded during the experiments. Combined with the measured water temperature the refractive index of the water was quantified using the relations between refractive index, wavelength  $\lambda$  and temperature  $T$  as described in Bashkatov & Genina (2003). The value for the refraction index  $n_{acryl}$  of acrylate is taken from literature (Kasarova *et al.*, 2007). For the refraction index of air a fixed valued ( $n_{air} = 1.0003$ ) is applied and determined using the Ciddor equation (Ciddor, 1996). As the variation of the refractive index of air in the experimental range is much smaller than the variation in the refractive index of the acrylate and water, it was

deemed acceptable to choose a fixed value for  $n_{air}$ . The wavelength range for the light emitted by the particles was 495 to 570 nm.

### 2.3.6 UNCERTAINTY IN 3D PARTICLE POSITION

The results on the uncertainty obtained for stationary particles cannot directly be transferred to moving particles though. The main reason for this is the fact that iPhones are mounted with CMOS sensors utilizing a ‘rolling shutter’. This means that the image is not taken instantaneously from the sensor like in CCD sensors but line after line. This results in the fact that one cannot put one moment in time to a given frame but rather a time interval. It is known that there are methods to counteract or rather almost eliminate this effect (Poelma, 2017), however the maximum observed movement for the particle in  $z$ -direction (the rolling shutter moves from top to bottom) between two frames is 6 pixels, this implies that the maximum time shift for one camera between top and bottom of the particle equals  $8/720 \cdot 1/120 \text{ s} = 9 \cdot 10^{-5} \text{ s}$  for the iPhone 5s and  $4.5 \cdot 10^{-5} \text{ s}$  for the iPhone 6. As the maximum velocity in  $x,y$  direction of the particle observed is in the order of magnitude of  $1 \text{ m s}^{-1}$ , this results in an uncertainty in  $z$ -position of about  $9 \cdot 10^{-5} \text{ m}$ . Another, and far more important uncertainty stemming from the rolling shutter principle, is that the uncertainty in the time parameter is also depending on the rolling shutter: the blinking LED is used to synchronise the camera's. This implies that just identifying the frame in which it blinks on or off results in an uncertainty in the recorded time of half the slowest shutter time (being  $\approx 1/240 \text{ s}$ ). The choice to work with off-the-shelf components proved to result in a well-functioning set-up, however at a price in terms of extended post-processing (e.g. synchronisation issues due to the rolling shutter) and a loss of accuracy when compared to other high-speed camera systems using CCD sensors. A major issue to be solved in future work is the subframe synchronisation. In this sense, the use of flash-light affecting the whole frame for all cameras simultaneously is considered as the main candidate and will be subject to further research.

### 2.3.7 PARTICLE REFLECTIONS ON WATER/AIR SURFACES

A main issue, even though much effort was put into this, was the presence of reflections on the water/air interfaces at the water surface and the air core of the vortex on and on the interface between water and the acrylate bottom of the tank. In order to counteract the latter, it might be an option to cover the bottom of the tank with non-fluorescent paint. However, this would reduce the possibility of illuminating the tank through the bottom which proved to be necessary in order to obtain enough illumination of the particles in the lower half of the tank. An option to reduce the effect of the reflections at the surface and air core is to apply masks when post-processing the raw footage. This would however imply that for almost each individual experiment a tailor-made mask has to be inserted. Given the amount of time to be spent

on this and the expected, relatively small, increase in data-yield (reflections prove to be significant only when the particle was close to either the water surface or close to the bottom (i.e.  $< 1L$ )) and a loss of uncertainty in position when the particle is masked by the air core for 3 out of 6 cameras, these options were not put into effect.

## 2.4 STEREO PARTICLE IMAGE VELOCIMETRY

### 2.4.1 SET-UP

The stereo PIV set-up comprises two cameras (LaVision Imager MX 4M) imaging a horizontal plane covering approximately one quadrant of the inner tank cylinder. One camera captures the plane of interest from above and the other images the plane from below. The cameras pixel size is  $5.5 \mu\text{m}$  at an image format of  $2048 \times 2048$  pixels. Two 28 mm objectives (Nikon Nikkor) are mounted on Scheimpflug adapters at the angle that yields the largest depth of field. Two acrylic water filled prisms are mounted on the tank to improve the imaging by reducing refraction effects. Nearest to the cameras the measurement plane is mapped onto the 10 bit CMOS sensor with a magnification of 0.079 and furthest from the cameras the magnification is 0.10. Figure 2.6 shows a sketch of the set-up. To measure over a radial distance from the vortex center that is as large as possible, the vortex core is positioned in a corner of the measurement domain. A pulsed laser (Litron lasers Nano L 50-100) at 532 nm and 50 mJ per pulse is used to generate a light sheet. For each measurement 500 image pairs are acquired at a sampling rate of 1 Hz. Stereo calibration for each plane is performed by placing a multilevel calibration target with round marks (LaVision, type 21) horizontally in the tank and using the third order polynomial method (Soloff *et al.*, 1997). The light sheet is aimed at and aligned with the calibration plate. The stereo self-calibration correction is on the order of 0.01 pixel and 0.01 degree. The flow is seeded with  $100 \mu\text{m}$  polyamide spheres (Vestosint) with density  $\rho = 1060 \text{ kg m}^{-3}$ . The particle seeding density is limited by the agglomeration of particulate matter in the core and is typically 10 particles per  $64 \times 64$  pixel area.

### 2.4.2 CONTOUR AVERAGING METHOD

To quantify  $V_\theta$  over a large radial distance from the core, while resolving large gradients in velocity in the core, the SPIV results are Contour Averaged (CA) over an angle from 0 to  $\pi/4$  radians. Figure 2.7(a) shows the area over which the CA over  $\pi/4$  radians is applied. To obtain an average of  $V_z$  and  $V_r$  over a larger azimuthal domain near the core, a second CA is determined by averaging over a polar angle from  $-\pi/2$  to  $\pi$ , see Figure 2.7(b). Vectors inside the air core interface are excluded from analysis.

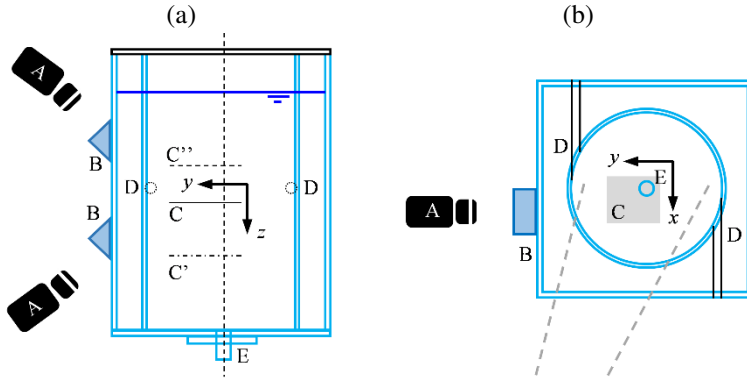


Figure 2.6: (a) (A) cameras, (B) water-filled prisms, (C) measurement area at height  $h = 0.49$  m above tank floor (laser light sheet), (C') measurement area at  $h = 0.29$  m above tank floor, (C'') measurement area at  $h = 0.62$  m above tank floor. (b) Top view of the setup. The grey lines indicate the width of the light sheet.

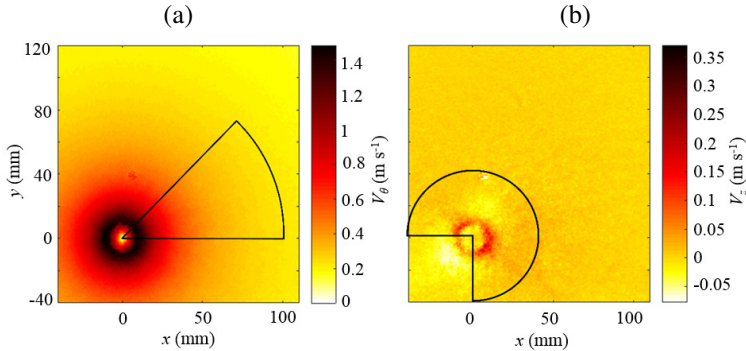


Figure 2.7: (a)  $V_\theta$  of series 1 at  $h = 0.29$  m. The area within the solid black line is the area in which CA is applied for the large domain. (b)  $V_z$ . The domain inside the black line is the area in which CA is applied for the azimuthal domain of  $3\pi/2$  rad ( $V_z$  and  $V_r$ ).

The angular domain for the CA of  $V_z$  is selected larger than that used for the CA of  $V_\theta$  to obtain an estimate of the axial mass flow at the cost of resolution of steep spatial gradients. The vortex center location is obtained by calculating the location of maximum rotation from the in-plane SPIV vector field results. Vector fields are determined using the DaVis8 PIV software by LaVision. A background subtraction is performed and a mask is applied. Universal outlier detection is used for vector validation (Westerweel & Scarano, 2005).

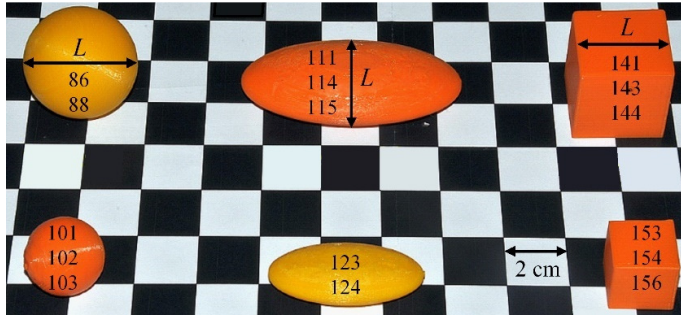


Figure 2.8: 3D printed experimental particles with  $L$  the characteristic length of the particles (spheres 71, 91 and 92 are not showed).

### 2.4.3 THE WEIGHTED CONDITIONAL AVERAGING METHOD

Weighted conditional averaging over the core location is performed as described in Pennings *et al.* (2015) in case the air core is not present in the measurement plane. The procedure of weighted conditional averaging of SPIV data consists of the following steps: (1) Conventional SPIV processing is performed at a coarse resolution ( $48 \times 48$  pixels using 50 % overlap for every double frame image). From the in-plane velocity vectors the core location is determined by fitting a parabola to the sum of the absolute values of the vertical and horizontal components. (2) The raw data files with similar vortex locations are grouped and a sum-of-correlation (SOC) processing is applied to the separate groups. (3) The SOC processing results of these groups are then weighted by the number of raw data images used in the group versus the total number of used images and summed. Using this approach, a higher spatial resolution can be attained. In the present work, the maximum spatial resolution is  $8 \times 8$  pixels with 50 % overlap which gives a vector spacing of 0.39 mm.

## 2.5 EXPERIMENTAL PARTICLES

The experimental particles are spheres, ellipsoids and cubes with a characteristic length ( $L$ ) of 0.02 to 0.04 m with specific relative densities varying between 0.6 and 1.0 in accordance with the range of the reported densities of typical FOG particles found in wastewater, see e.g. Xia He *et al.* (2013), Nieuwenhuis *et al.* (2017) and Keener *et al.* (2008). In practise the particles will show cohesiveness which is assumed to be of importance once a sum layer forms, since the main interest here lies with the transport characteristics of individual particles this cohesiveness was not reproduced in the experimental particles used for the experiments. The particles have been produced in PLA (specific density of  $1.240 \text{ kg m}^{-3}$ ) using two 3D printers (Ultimaker To Go 2+ and To Go 2+ Extended), see Nieuwenhuizen (2017). By choosing a specific empty volume inside the particle, a fine tuning of the specific weight of each

Table 2.3: Experimental particles and characteristics.

Particle number	Shape	Dimension	Density
71	Sphere	Ø20 mm	$692 \pm 1 \text{ kg m}^{-3}$
83	Sphere	Ø38 mm	$630 \pm 1 \text{ kg m}^{-3}$
84	Sphere	Ø38 mm	$616 \text{ kg m}^{-3}$
86	Sphere	Ø38 mm	$709 \pm 2 \text{ kg m}^{-3}$
88	Sphere	Ø38 mm	$665 \pm 2 \text{ kg m}^{-3}$
91	Sphere	Ø19 mm	$675 \text{ kg m}^{-3}$
92	Sphere	Ø19 mm	$600 \text{ kg m}^{-3}$
101	Sphere	Ø25 mm	$771 \pm 5 \text{ kg m}^{-3}$
102	Sphere	Ø25 mm	$730 \pm 5 \text{ kg m}^{-3}$
103	Sphere	Ø25 mm	$860 \pm 3 \text{ kg m}^{-3}$
111	Ellipsoid	$76 \times 38 \times 19 \text{ mm}$ ( $L = 38 \text{ mm}$ )	$787 \pm 1 \text{ kg m}^{-3}$
113	Ellipsoid	$76 \times 38 \times 19 \text{ mm}$ ( $L = 38 \text{ mm}$ )	$666 \pm 1 \text{ kg m}^{-3}$
114	Ellipsoid	$76 \times 38 \times 19 \text{ mm}$ ( $L = 38 \text{ mm}$ )	$859 \pm 2 \text{ kg m}^{-3}$
123	Ellipsoid	$38 \times 19 \times 9.5 \text{ mm}$ ( $L = 19 \text{ mm}$ )	$875 \pm 2 \text{ kg m}^{-3}$
124	Ellipsoid	$38 \times 19 \times 9.5 \text{ mm}$ ( $L = 19 \text{ mm}$ )	$973 \pm 4 \text{ kg m}^{-3}$
141	Cube	$30.6 \times 30.6 \times 30.6 \text{ mm}$	$746 \pm 2 \text{ kg m}^{-3}$
143	Cube	$30.6 \times 30.6 \times 30.6 \text{ mm}$	$914 \pm 1 \text{ kg m}^{-3}$
144	Cube	$30.6 \times 30.6 \times 30.6 \text{ mm}$	$859 \pm 1 \text{ kg m}^{-3}$
153	Cube	$20.2 \times 20.2 \times 20.2 \text{ mm}$	$923 \pm 2 \text{ kg m}^{-3}$
154	Cube	$20.2 \times 20.2 \times 20.2 \text{ mm}$	$869 \pm 4 \text{ kg m}^{-3}$
156	Cube	$20.2 \times 20.2 \times 20.2 \text{ mm}$	$895 \pm 3 \text{ kg m}^{-3}$

particle is allowed. The uncertainty in  $\rho_p$  is determined to be in a range of 1 to 5  $\text{kg m}^{-3}$  (Nieuwenhuizen, 2017). The characteristics of the experimental particles are summarized in Table 2.3.

# 3

## **THE FREE-SURFACE VORTEX 3D- FLOW FIELD**

The main content of this chapter is based on Duinmeijer, S.P.A., Oldenziel, G. & Clemens, F.H.L.R. (2019b). *Experimental study on the 3D-flow field of a free-surface vortex using stereo PIV*. Journal of Hydraulic Research,

DOI: 10.1080/00221686.2018.1555558.

### 3.1 INTRODUCTION

To study the free-surface vortex driven particle motion it is essential to obtain knowledge of the 3D-flow in both the vortex core and outer field. Furthermore, as air entrainment by an air core that extends into the pump must be prevented in the practical application of the free-surface vortex, there is a need for a reliable quantification of the air core depth  $H_D$ .

Over the last decades numerous research projects on the characteristics of free-surface vortex flow field have been reported. A part of the literature focuses on deriving the governing parameters and the effects of viscosity and surface tension on the vortex formation e.g. Anwar (1966, 1978), Dagget & Keulegan (1974), Rindels & Gulliver (1983) and Suerich-Gulick *et al.* (2014a). Other research focusses on deriving expressions to compute the minimum submergence depth above an intake needed to prevent air entrainment by an air core extending into the pump e.g. Anwar & Amphlett (1980), Odgaard (1986), Gulliver & Rindels (1986). Yet another part of research aims on validating vortex models using experimental data e.g. Hite & Mih (1994), Wang *et al.* (2011) and Sun & Liu (2015). Nevertheless, only little accurate experimental data is available on measurements of the 3D-flow in both the outer field and vortex core at different vertical positions and especially regarding the axial flow profile in the vortex core and its gradient in the vertical direction. To obtain knowledge on the free-surface vortex 3D-flow, the research questions addressed in this chapter are (1) What is the distribution of the vortex velocity components in the vortex core and outer field? (2) Can the Burgers (1948) vortex model be validated to enable the quantification of the vortex characteristics? (3) What is the ratio  $Q_v/Q$  between the axial vortex flow  $Q_v$ , and total flow  $Q$ ?

To answer the above research questions, the outline of this research is as follows. The vortex 3D-flow field in the outer field and vortex core is measured in three horizontal planes using the stereo particle image velocimetry (SPIV) method as addressed in section 2.4. A cylindrical coordinate system  $(r, \theta, z)$  is applied where the flow field is presented in tangential ( $V_\theta$ ), radial ( $V_r$ ) and axial ( $V_z$ ) velocities. The measured profiles of  $V_\theta$ ,  $V_r$  and  $V_z$  are compared with the  $V_\theta$  profile of the Burgers (1948) vortex model and with the  $V_z$  profiles proposed by Hite and Mih (1994) and Wang *et al.* (2011). In the vortex flow, the core radius  $r_c$  is a characteristic parameter illustrating the radial position of transition between the vortex core and outer field. Burgers (1948) developed a model (hereafter referred to as Burgers' model) to compute  $r_c$  with  $r_c = 2(\nu/a)^{0.5}$  representing the ratio between axial vortex stretching and molecular viscous diffusion of vorticity with  $a = \partial V_z/\partial z$  the stretching parameter and  $\nu$  the kinematic viscosity. As Burgers' model assumes an unrealistic radially independent  $V_z$  profile ( $\partial V_z/\partial r = 0$ ), the validity of this model is studied when the measured radially

dependent  $V_z$  is modelled as a spatially average value  $\overline{V_z}$ . Furthermore, the accuracy of Burgers' model to predict  $H_D$  for the present setup is examined.

First, section 3.2 addresses the theoretical background of free-surface vortices and the Burgers model. Section 3.3 presents the measuring program. In section 3.4 to 3.5 the results obtained for the velocity profiles are described and in section 3.6 to 3.7 the validity of Burgers' model to compute  $r_c$  and  $H_D$  are discussed.

### 3.2 THE FREE-SURFACE VORTEX AND THE BURGERS VORTEX MODEL

A free-surface vortex is characterized by a solid-body rotating core with vorticity and an outer field of irrotational flow without vorticity, see Figure 3.1(a) where the flow field at the left side of  $r_c$  is in solid-body rotation and the field at the right side is irrotational flow. The vorticity  $\boldsymbol{\omega}$  is defined as the curl of the velocity vector and related to the angular momentum of a fluid particle around its center of mass:

$$\boldsymbol{\omega} = \nabla \times \mathbf{V}. \quad (3.1)$$

In cylindrical coordinates this is:

$$\boldsymbol{\omega} = \left( \frac{1}{r} \frac{\partial V_z}{\partial \theta} - \frac{\partial V_r}{\partial z} \right) \mathbf{e}_r + \left( \frac{\partial V_r}{\partial z} - \frac{\partial V_z}{\partial r} \right) \mathbf{e}_\theta + \frac{1}{r} \left( \frac{\partial}{\partial r} (r V_\theta) - \frac{\partial V_z}{\partial \theta} \right) \mathbf{e}_z. \quad (3.2)$$

A two-dimensional model describing  $V_\theta$  for both fields was proposed by Rankine (1858):

$$\begin{aligned} V_\theta &= \Omega r = \frac{\Gamma}{2\pi} \frac{r}{r_c^2} \quad (r < r_c) \\ V_\theta &= \frac{\Gamma}{2\pi r} \quad (r \geq r_c). \end{aligned} \quad (3.3)$$

In which  $\Omega$  is the angular velocity of the vortex core and  $r_c$  is the position of the transition between the vortex core and the outer field, see Figure 3.1(a). The flow circulation  $\Gamma$  is defined as the line integral of a velocity around a closed curve  $C$ , based on Stokes' theorem it represents the flux of the vorticity vector  $\boldsymbol{\omega}$  through any surface area  $A$  bounded by the closed curve  $C$ :

$$\Gamma = \oint_C \mathbf{V} ds = \iint_A \boldsymbol{\omega} \cdot \hat{\mathbf{n}} dA. \quad (3.4)$$

Consequently, a circulation on  $C$  has a region that contains vorticity. In the Rankine model this region is the vortex core with  $\boldsymbol{\omega} = 2\Omega$ , see Figure 3.1(b).

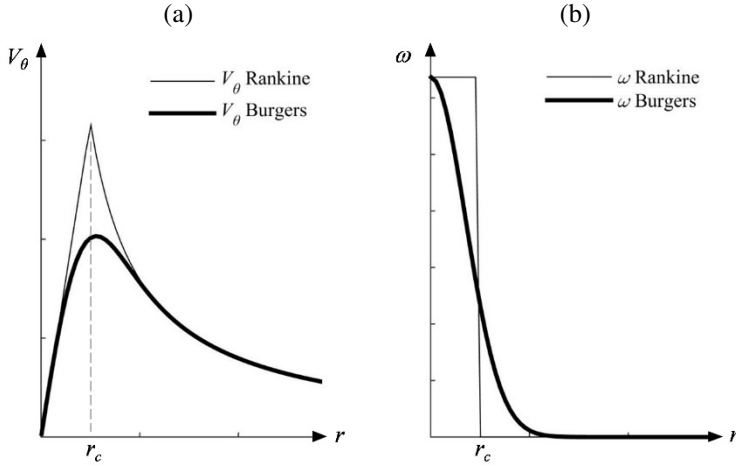


Figure 3.1: (a) Distribution of tangential velocity  $V_\theta$ . (b) Distribution of vorticity  $\omega$ . In the Rankine model, all vorticity is concentrated in the vortex core of solid-body rotation where the Burgers model shows viscous diffusion of vorticity.

Based on the Navier-Stokes equations, Burgers proposed a 3D-vortex model that describes a balance between intensification of vorticity (the vortex stretching) and viscous diffusion of vorticity, see Figure 3.1(b). Burgers' model is based on the equation of conservation of vorticity given by:

$$\frac{D\boldsymbol{\omega}}{Dt} = (\boldsymbol{\omega} \cdot \nabla) \mathbf{V} + \nu \nabla^2 \boldsymbol{\omega}. \quad (3.5)$$

For an axi-symmetric flow there is only vorticity in  $z$ -direction, allowing to reformulate equation (3.5) as:

$$\frac{\partial \omega_z}{\partial t} + V_r \frac{\partial \omega_z}{\partial r} + V_z \frac{\partial \omega_z}{\partial z} + \frac{V_\theta}{r} \frac{\partial \omega_z}{\partial \theta} = \omega_z \frac{\partial V_z}{\partial z} + \nu \left( \frac{\partial^2 \omega_z}{\partial r^2} + \frac{1}{r} \frac{\partial \omega_z}{\partial r} \right). \quad (3.6)$$

Without an external torque acting on the vortex and defining the terms  $\partial \omega_z / \partial \theta = \partial \omega_z / \partial z = 0$  because of axi-symmetry and constant vorticity in  $z$ -direction, the vorticity is only a function of  $r$ :

$$V_r \frac{\partial \omega_z}{\partial r} = \omega_z \frac{\partial V_z}{\partial z} + \nu \frac{1}{r} \frac{\partial}{\partial r} \left( r \frac{\partial \omega_z}{\partial r} \right). \quad (3.7)$$

The first term of the right-hand side represents vortex stretching or extensional strain. To solve equation (3.7) with the boundary conditions  $\omega_z(0)$  and  $\omega_z(\infty)$ , Burgers assumes an axial velocity profile that is independent of  $r$  and varies linearly with  $z$ :

$$\begin{aligned} V_z &= az \\ V_r &= -0.5ar. \end{aligned} \quad (3.8)$$

The profile of  $V_r$  is a result of conservation of mass. Using these profiles in equation (3.7) the following vorticity equation is obtained:

$$\frac{\partial \omega_z}{\partial r} = -\left(\frac{a}{2\nu}\right)r\omega_z \quad (3.9)$$

Integrating equation (3.9) gives the solution for the distribution of vorticity in radial direction:

$$\omega_z(r) = \omega_0 \exp\left[-\left(\frac{r}{r_c}\right)^2\right] \quad (3.10)$$

where:

$$\omega_0 = \frac{\Gamma_\infty}{\pi r_c^2} \quad (3.11)$$

the vorticity in the vortex center and  $r_c$  is the core radius, presenting the ratio between axial stretching  $a = \partial V_z / \partial z$  and molecular diffusion of vorticity:

$$r_c = 2\sqrt{\frac{a}{\nu}} \quad (3.12)$$

Applying Stokes' theorem on equation (3.10), the Burgers profile of  $V_\theta$  is obtained:

$$V_\theta = \frac{\Gamma_\infty}{2\pi r} \left\{ 1 - \exp\left[-\left(\frac{r}{r_c}\right)^2\right] \right\} \quad (3.13)$$

It is noted that Burgers' assumption that  $\partial V_z / \partial r = 0$  seems not valid for real vortices in the far flow field but may hold in the direct vicinity of the core. Various authors, e.g. Vatis (1989), Mih (1991), Wang *et al.* (2011) and Sun and Liu (2015) proposed expressions based on equation (3.13) without the exponential term and using a dimensionless radius  $R = r/r_c$ .

### 3.3 EXPERIMENTAL PROGRAM

The experimental program to measure  $r_c$ ,  $V_\theta$ ,  $V_r$  and  $V_z$  consisted of eight series of different hydraulic conditions. Series one to four was conducted with  $D = 0.03$  m and series five to eight were conducted with  $D = 0.044$  m. All experiments were conducted with an undisturbed water depth  $H$  of 0.90 m. The quantities were measured at three horizontal planes at  $h = 0.29, 0.49$  and  $0.62$  m measured from the tank bottom. The

Table 3.1: Measurement series with hydraulic conditions and  $\Gamma_{quad}$ .

Series	$Q$ (m <sup>3</sup> h <sup>-1</sup> )	$D$ (m)	$\Gamma_{quad}$ (m <sup>2</sup> s <sup>-1</sup> )	Series	$Q$ (m <sup>3</sup> h <sup>-1</sup> )	$D$ (m)	$\Gamma_{quad}$ (m <sup>2</sup> s <sup>-1</sup> )
1	0.69	0.030	$0.07 \pm 0.00$	5	1.50	0.044	$0.16 \pm 0.01$
2	0.69	0.030	$0.08 \pm 0.00$	6	1.50	0.044	$0.23 \pm 0.01$
3	1.16	0.030	$0.12 \pm 0.01$	7	2.50	0.044	$0.31 \pm 0.01$
4	1.16	0.030	$0.17 \pm 0.01$	8	2.50	0.044	$0.44 \pm 0.02$

range of experimental hydraulic conditions  $D$ ,  $Q$  and  $\Gamma$  were selected to generate vortices with air core depths in the range of 0.09 m to 0.85 m. The selected flow rates resulted in two equal  $U_o$  values for four series. This condition was selected to study the relation between  $U_o$  and  $r_c$  as discussed later. All four series consisted of measurements with two flow rates and with two different  $\Gamma$  for each flow rate.  $\Gamma$  was changed by using one or both inlet pipes. Table 3.1 shows the measurement series and  $\Gamma_{quad}$  with 95% confidence interval determined by the quadripod.

### 3.4 EXPERIMENTAL RESULTS

The measured velocity profiles are analysed for measurements with no air core crossing a measurement plane only. Because of the different SPIV measurements post processing methods,  $V_r$  and  $V_z$  are shown for  $0 < r < 0.04$  m and  $V_\theta$  is shown for  $0 < r < 0.10$  m.

#### 3.4.1 CIRCULATION

Based on equation (2.1), Figure 3.2 shows the  $\Gamma$  of both the floating quadripod ( $\Gamma_{quad}$ ) and SPIV measurements ( $\Gamma_{SPIV}$ ) for all series. The  $\Gamma_{SPIV}$  is plane averaged and determined at  $r = 0.135$  m.  $\Gamma_{quad}$  includes the 95% confidence interval ( $\pm 2\sigma$ ) due to uncertainties in the measured parameters. For the presented research purposes,  $\Gamma_{quad}$  shows a sufficiently close match to  $\Gamma_{SPIV}$ . Differences between both methods can be explained by the observation that the  $\Gamma_{SPIV}$  shows a minor gradient in the radial direction indicating that the outer field is not entirely irrotational. This was also observed in the PIV measurements of Sun and Liu (2015). There is a radial variation as well in  $\Gamma_{SPIV}$  due to the concentrated momentum influx from the  $\varnothing 25.9$  mm inlet pipes. This causes a slightly non-uniform distribution of angular momentum along the radial direction throughout the outer field.

#### 3.4.2 TANGENTIAL VELOCITY PROFILES

For series three and five (all series are found in Appendix B) the measured velocities in each plane are shown in Figure 3.3. The figure also shows Burgers' profile of  $V_\theta$

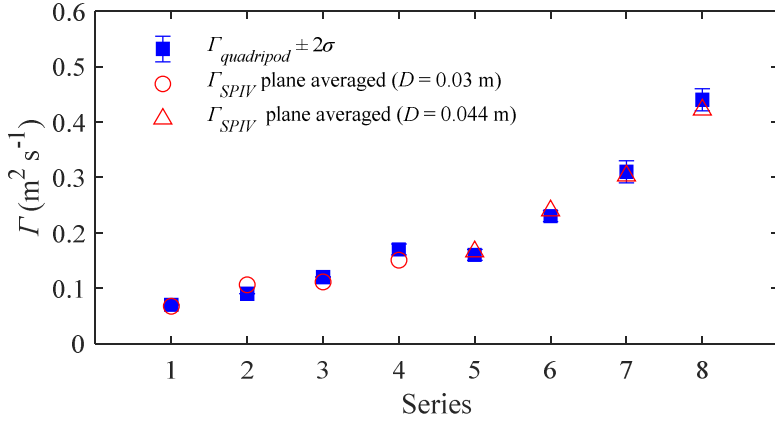


Figure 3.2:  $\Gamma$  measured by quadripod at  $r = 0.15$  m and by SPIV at  $r = 0.135$  m. The error bars represent the 95% confidence interval.

(equation (3.13)) by using the measured  $\Gamma_\infty$  and  $r_c$  for that plane. For  $\Gamma_\infty$ , the  $\Gamma_{SPIV}$  at  $r = 3r_c$  is used where the vorticity is decreased to almost zero and the flow is assumed being irrotational (Suerich-Gulick *et al.* 2014b). The determination of the measured  $r_c$  is given in section 3.6. For all series, the measured profiles of  $V_\theta$  show only slight differences between the different planes. Indeed, for this axi-symmetric vortex, the assumption is that  $\partial V_\theta / \partial z \sim 0$  as is shown by the PIV data of e.g. Sun and Liu (2015) as well and which characterizes the 2D line vortex. Burgers' profiles of  $V_\theta$  match the measured profiles. However, for series five (and a few others) the model shows an under-prediction of the maximum velocity. This is not related to the non-uniformity of  $\Gamma_{SPIV}$  in the outer field and postulating  $\Gamma_{SPIV}$  at  $r = 3r_c$  as  $\Gamma_\infty$ . The use of  $\Gamma_\infty$  calculated at  $r = 5r_c$  gives no significant changes in maximum velocities. The deviations  $\delta V_\theta$  are possibly related to a combination of (a) Burgers' assumption of a radially independent axial velocity and (b) the uncertainty of  $r_c$ . However, by defining a required accuracy  $|\delta V_\theta / V_\theta| < 10\%$  for the presented research purposes, the Burgers model produces a sufficiently accurate prediction of the  $V_\theta$  profile.

### 3.4.3 RADIAL VELOCITY PROFILES

The analysis of the measured profiles of  $V_r$  was shown to be straight forward. Figure 3.3 and Figure 3.4 show that the velocities are relatively low ( $< 0.1$  m s<sup>-1</sup>) and are observed to be the same order as the uncertainties. Therefore, the analysis is limited to a qualitative description of the velocity profiles. The velocities are negative representing radial inflow towards the vortex center. The inflow is concentrated in a domain with radius comparable to the outlet radius with a maximum at  $\sim r_c$  which was also found in the PIV data of Sun and Liu (2015). The measured velocity profiles

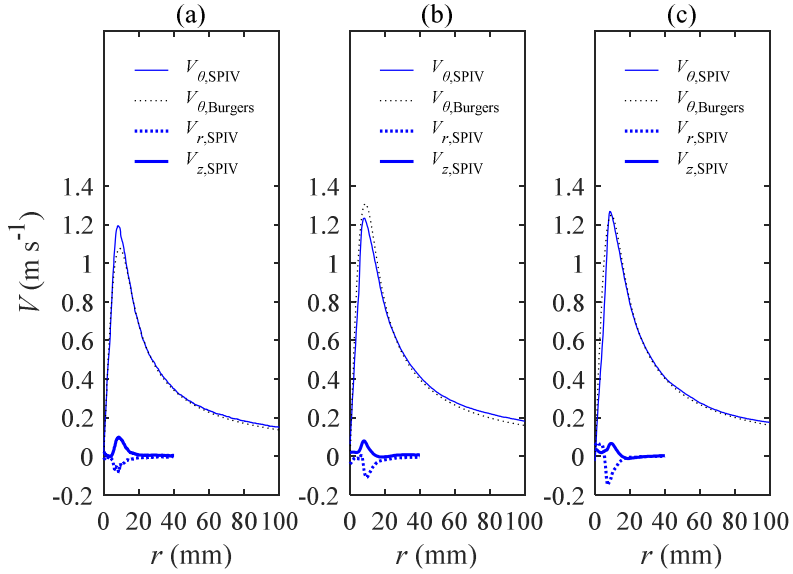


Figure 3.3: Measured profiles of  $V_{\theta}$ ,  $V_r$  and  $V_z$  for series 3 with  $D = 0.03$  m. (a) Profiles at plane 0.29 m. (b) Profiles at plane 0.49 m. (c) Profiles at plane 0.62 m. The graphs include Burgers' profile of  $V_{\theta}$  (equation (3.13)) using the characteristic parameters  $\Gamma_{\infty}$  and  $r_c$ .

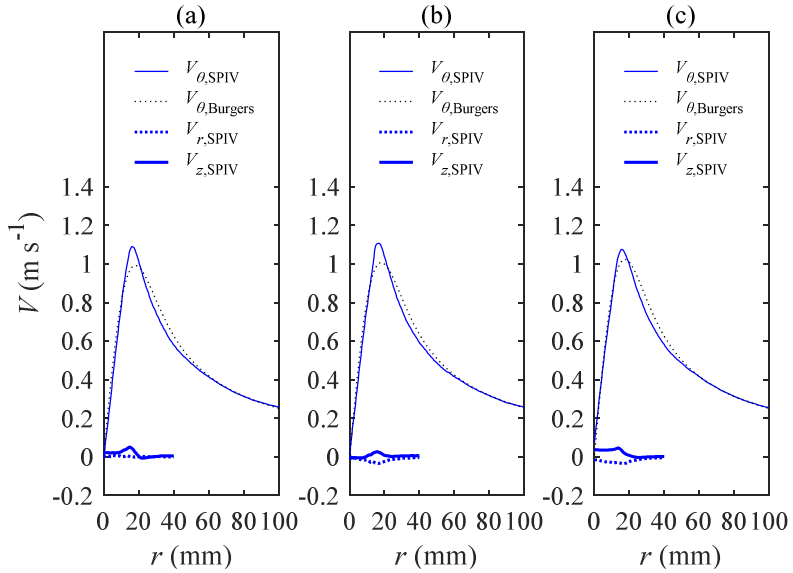


Figure 3.4: Measured profiles of  $V_{\theta}$ ,  $V_r$  and  $V_z$  for series 5 with  $D = 0.044$  m. (a) Profiles at plane 0.29 m. (b) Profiles at plane 0.49 m. (c) Profiles at plane 0.62 m. The graphs include Burgers' profile of  $V_{\theta}$  (equation (3.13)) using the characteristic parameters  $\Gamma_{\infty}$  and  $r_c$ .

show some similarity with the model Einstein and Li (1951) proposed, assuming axial plug flow bounded by a domain with radius  $\alpha$  and  $V_z = 0$  at  $r > \alpha$ :

$$V_r = \begin{cases} -\frac{qr}{2\pi\alpha^2}, & r < \alpha, \\ -\frac{q}{2\pi r}, & r > \alpha \end{cases} \quad (3.14)$$

where  $q = Q_v/H$ . The vortex flow rate  $Q_v$  is defined as the axial down-flow. Unfortunately, a quantitative comparison with the measured profiles is not possible.  $V_r$  is found to be negligible compared to  $V_\theta$ . This supports the choice that was made to neglect the  $V_r$  terms in the computation of  $H_D$  as discussed in section 3.7.

### 3.4.4 AXIAL VELOCITY PROFILES

For all series, the measured profiles show that the axial down-flow is primarily concentrated in a domain with a radius in the order of 2 to  $3r_c$  while having a semi-parabolic profile with a maximum at  $r_c$ . Figure 3.5 shows the SPIV measured axial velocities for experimental series 1 to 7. A similar profile was observed in the experiments of Ito *et al.* (2014). The maximum  $V_z$  is observed to be in a range of 4 to 8% of the maximum  $V_\theta$ .

The measured velocity profiles are not in line with the  $V_z$  models of e.g. Hite and Mih (1994) and Wang *et al.* (2010). These models suggest that the maximum  $V_z$  occurs at the axis of symmetry. However, the models mentioned were validated using experimental data available for  $r > r_c$  only, while no data were available for model validation of the vortex core region.

In order to ensure mass conservation, the  $V_z$  profile should show a positive gradient in the downward direction ( $\partial V_z / \partial z > 0$ ). As  $V_r$  is assumed to be constant in the axial direction, the gradient is constant and thus  $V_z$  follows a linear profile along the vortex length. The gradient is not clearly visible for series one and two because the differences in  $V_z$  between the planes are very small and in the same order of magnitude as the measurement uncertainties. The uncertainty for these series are assumed to be 0.2 to 2% of the maximum value of  $V_\theta$  (Westerweel & Scarano, 2005).

### 3.4.5 SECONDARY FLOW PATTERNS

The measured  $V_z$  profiles do not show any significant velocities in the outer flow field ( $r > 3r_c$ ). Consequently, secondary flow patterns in the outer field as observed by e.g. Echávez and McCann (2002) are not expected. However, a reliable statement on the absence of (small) secondary flow patterns cannot be made, as the very small

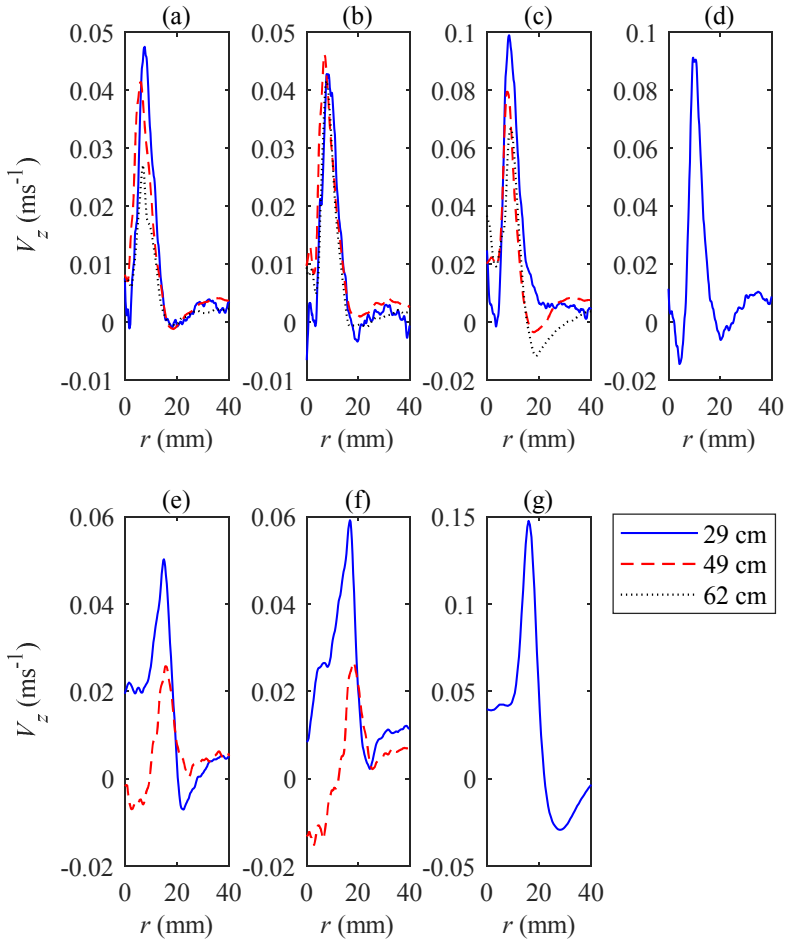


Figure 3.5: (a)-(g) SPIV measured axial velocity profiles  $V_z(r, z)$  at three heights in the vortex tank for series 1 to 7. For series 4 to 7 ((d)-(g)), the presence of the air core affected the measurements for the planes  $h = 0.49$  and  $0.62$  m and thus not considered.

velocities in the outer field are in the same order of magnitude as the measurement uncertainty.

### 3.5 AXIAL VORTEX FLOW

For each plane the axial vortex flow  $Q_v$  is determined by integration of the  $V_z$  profile over the cross-sectional area  $A$ :

$$Q_v(z) = \iint_A V_z(r) dA = 2\pi \int_0^r V_z(r) r dr \quad (3.15)$$

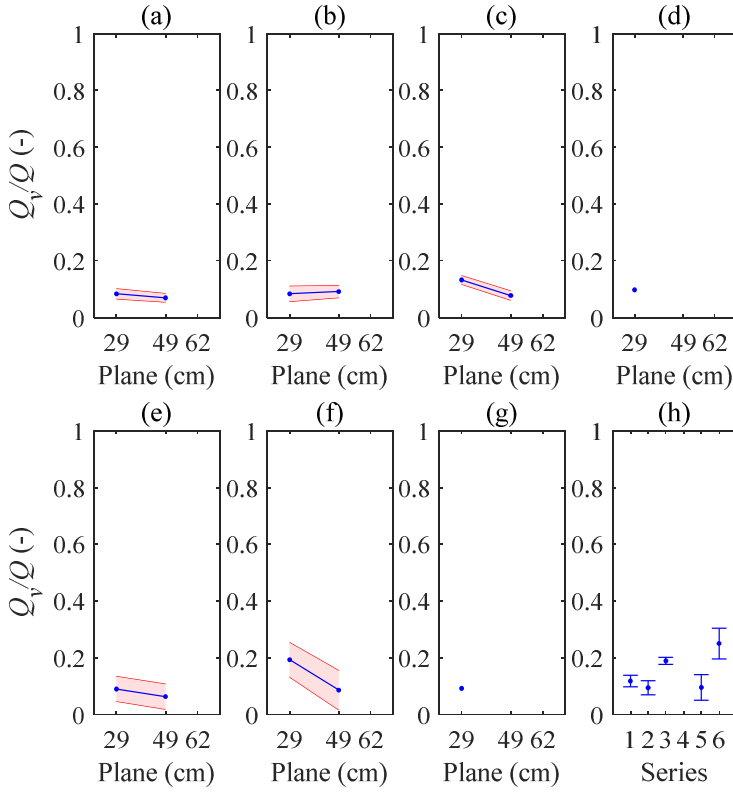


Figure 3.6: (a) to (g) ratio between axial vortex flow  $Q_v$  and total flow  $Q$  for the measurement planes  $h = 0.29$  and  $h = 0.49$  m. (h) Approximation of  $Q_v/Q$  at tank bottom ( $h = 0$  m). All values include the 95% confidence interval.

where  $A$  is the area containing all axial flow bounded by  $r$ . The integration boundary is defined in terms of  $r_c$  and set to  $2.2r_c$  to use the largest number of available measured values of  $V_z$ . Figure 3.6 shows the computed ratios  $Q_v/Q$  for the planes 0.29 and 0.49 m. The  $Q_v/Q$  of series four and plane 0.49 m is considered as an outlier because of hindered optics due to agglomeration of particulate contamination in the vortex core just below the air-water interface. All measurements show distinctly that the vortex carries only a small percentage of the discharge  $Q$ . This is in line with the experimental observations made by Echavez and McCann (2002) and Andersen *et al.* (2006). By assuming a linear gradient in vortex flow between the planes,  $Q_v$  at the tank bottom is quantified by extrapolation of the obtained values of  $Q_v$  between the planes 0.62 and 0.29 m to the tank bottom. Figure 3.6 shows that  $Q_v$  at the tank bottom falls in a range of 10 to 25% of  $Q$ . Furthermore, there is no clear relation observed between the maximum  $Q_v/Q$  and the discharge  $Q$  or outlet diameter  $D$ .

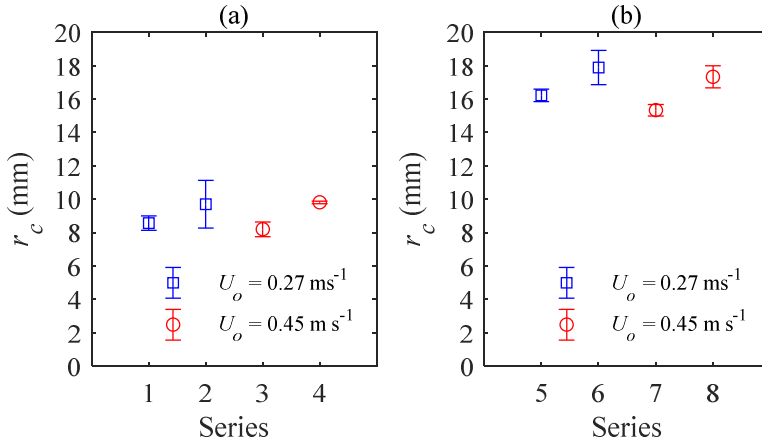


Figure 3.7: Plane averaged  $\bar{r}_c$  obtained from location of maximum  $V_\theta$  including the 95% confidence interval. (a)  $\bar{r}_c$  for series with  $D = 0.03$  m. (b)  $\bar{r}_c$  for series  $D = 0.044$  m.

## 3.6 VALIDATION OF THE BURGERS MODEL TO DETERMINE THE CORE RADIUS

### 3.6.1 VORTEX CORE RADIUS

The validation of Burgers' model to compute  $r_c$  is based on the experimentally observed  $r_c$ . This  $r_c$  is taken equal to the radial position where the measured  $V_\theta$  is maximal ( $V_{\theta\text{-max}}$ ). For each series,  $r_c$  is assumed to be normally distributed and

presented as  $\bar{r}_c \pm \sigma_c$ , where  $\bar{r}_c$  is the mean value of the three planes and  $\sigma_c$  the standard deviation. A Student t-test shows less than 5% significance for each mean radius  $\bar{r}_{c,p} \pm \sigma_{c,p}$  of each plane constructed by the 95% confidence interval of measured velocities around  $\bar{r}_{c,p}$  where  $V_\theta(r) + 2\sigma_{v\theta} < V_{\theta\text{-max}}$ . When the air core intersects a measurement plane, the radius is not considered in the calculation of  $\bar{r}_c$  except for series eight in which the air core diameter was smaller than  $r_c$ . For series seven to eight,  $\sigma_c$  is taken equal to the standard deviation of the 95% interval as the velocities are only measured for one plane. Figure 3.7 shows  $\bar{r}_c$  including the 95% confidence interval.

### 3.6.2 RELATION BETWEEN $U_o$ AND CORE RADIUS

Figure 3.7 shows that there is no unique relation between the average outlet velocity  $U_o$  and  $r_c$ . Using only  $U_o$  to compute  $r_c$  seems invalid, as does Odgaard's (1986) model to predict the submergence depth  $S$  by using  $r_c = 2(v_{\text{eff}}/a)^{0.5}$  with  $a = \partial V_z / \partial z = U_o/H$ . Odgaard (1986) proposes that an increase in circulation leads to high radial shear

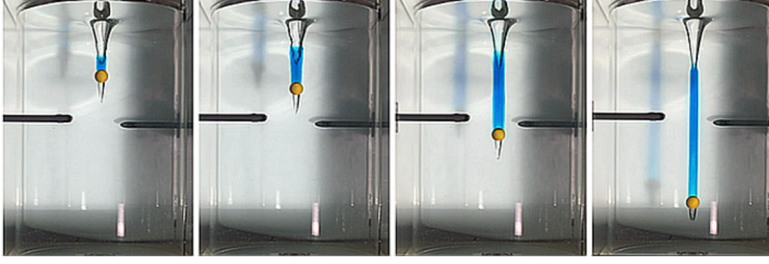


Figure 3.8: Experiment of slow axial transport of a  $\varnothing 50$  mm sphere in a vortex with  $r_c \approx 17$  mm where dye is injected into the vortex core above the sphere. The dye core shows no radial diffusion of dye towards the outer field and thus no indication of radial diffusion of mass by turbulence in the core.

stresses near the vortex core that generates turbulence which increases diffusion of vorticity. To include the radial diffusion of vorticity by turbulence, Odgaard introduced an effective viscosity  $\nu_{eff} = \nu + k\Gamma_\infty$  with  $k\Gamma_\infty$  the eddy viscosity and  $k$  the factor of proportionality given by  $k = 6 \cdot 10^{-5}$  for a typical experimental setup. For the presented research here, the Reynolds number  $Re$  is in a range between  $8 \cdot 10^3$  and  $2 \cdot 10^4$  with  $Re$  defined by  $V_\theta r_c / \nu$ . In this range, radial turbulence can be present. However, the results presented here show that the occurrence of radial turbulence around the vortex core is uncertain as showed by Figure 3.8 where no radial diffusion of dye is observed. Suerich-Gulick *et al.* (2014a, 2014b) propose a semi-empirical model to determine  $r_c$  from the approach flow and the geometry of a specific laboratory-scale hydropower intake based on Burgers' model of  $r_c = 2(\nu/a)^{0.5}$ . The experimental results reported by Suerich-Gulick *et al.* (2014a, 2014b) match with Burgers' model without using eddy viscosity. These results suggest that eddy viscosity is used to compensate the undecided use of  $U_o$  to predict  $r_c$ . For a similar type of experimental setup as the presented setup here, Sun *et al.* (2015) propose an expression where  $r_c$  is only a function of  $\Gamma_\infty$ :  $r_c = 1.69 \Gamma_\infty^{0.55}$ . However, as  $\Gamma_\infty$  strongly depends on  $Q$ , Sun *et al.* (2015) show also a relation between  $Q$  and  $r_c$ . Using the equation suggested by Sun *et al.* (2015) with the measured  $\Gamma_\infty$  presented here and

comparing the thus determined  $r_c$  with the measured  $r_c$ , shows significant deviations. Consequently, relations between vortex characteristics appear to be highly dependent on the geometry of the experimental setup used.

### 3.6.3 VALIDATION OF BURGERS' MODEL WHEN USING RADIALLY DEPENDENT $V_z$ PROFILES

Burgers' model of  $r_c = 2\sqrt{\nu / dV_z / dz}$  is derived using the assumption of a radially independent  $V_z$  profile given by  $V_z = az$ . The measured  $V_z$  profiles show that this assumption not valid. In this section, the validity of this model is studied for radially

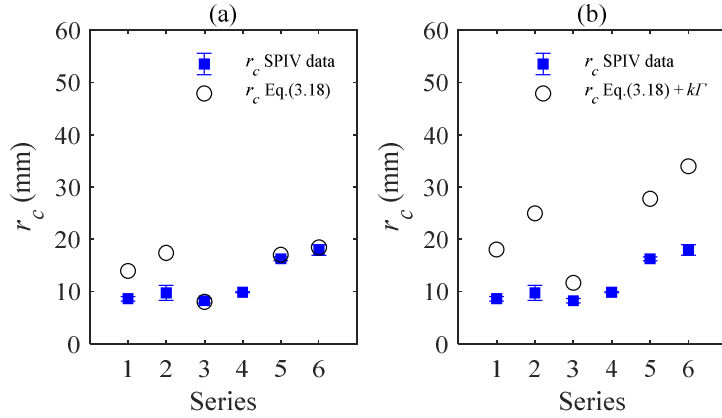


Figure 3.9: (a) Comparison of measured and computed  $r_c$  using  $\overline{V_z}$ . (b) Comparison including extra radial diffusion of vorticity by turbulence with  $k\Gamma$  of the same order of magnitude as the kinematic viscosity.

dependent  $V_z$  profiles comparable to the present measurements of  $V_z$ . To do this, the measured  $V_z$  profile is converted to a radially independent average velocity  $\overline{V_z}$  which is used in Burgers' model for  $r_c$ .  $\overline{V_z}$  is computed based on the vortex axial flow  $Q_v$ :

$$\overline{V_z} = \frac{\iint_A V_z(r) dA}{A} = \frac{Q_v}{\pi(2.2r_c)^2} \quad (3.16)$$

with  $A$  bounded by  $r = 2.2r_c$ . Assuming the profile of  $V_z$  linear with  $z$ , the gradient  $d\overline{V_z}/dz$  is then computed by using the average gradient of  $dQ_v/dz$  between the planes:

$$\frac{d\overline{V_z}}{dz} = \frac{1}{n-1} \sum_{i=1}^{n-1} \left\{ \frac{1}{[h^{(i+1)} - h^{(i)}]} \left[ \frac{Q_v(i)}{\pi(2.2r_{c,i})^2} - \frac{Q_v(i+1)}{\pi(2.2r_{c,i+1})^2} \right] \right\} \quad (3.17)$$

with  $Q_v = (Q_{v,0.29}, Q_{v,0.49}, Q_{v,0.62})$  and  $h = (0.29 \text{ m}, 0.49 \text{ m}, 0.62 \text{ m})$  and  $n$  the number of planes where  $Q_v$  is measured. By substituting equation (3.17) in Burgers' model of  $r_c$ , the following expression is obtained to compute  $r_c$  with the Burgers model:

$$r_c = 2 \sqrt{v \left( \frac{1}{n-1} \sum_{i=1}^{n-1} \left\{ \frac{1}{[h^{(i+1)} - h^{(i)}]} \left[ \frac{Q_v(i)}{\pi(2.2r_{c,i})^2} - \frac{Q_v(i+1)}{\pi(2.2r_{c,i+1})^2} \right] \right\} \right)^{-1}}. \quad (3.18)$$

Figure 3.9(a) shows the computed  $r_c$  for series 1, 2, 3, 5 and 6 (for series 5 the gradient is used between the planes 0.29 and 0.49 m). The determined value for  $r_c$  for the series 3, 5 and 6 show a match with the measured  $r_c$ , while series 1 and 2 show a deviation

of circa 60%. These deviations are possibly related to the small axial velocity differences between the planes with the same order of magnitude as the measurement uncertainty. Another explanation could be the presence of a Taylor-Proudman column above the outlet, suppressing axial velocity gradients. The typical Rossby number ( $Ro = V_\theta(r_c)/2\Omega r_c$ ) for this setup is circa 0.5, indicating that the Coriolis forces are of the same order of magnitude as the inertial forces. A further discussion on this phenomenon however, is beyond the scope of this study. To conclude, it seems valid to apply Burgers' model for the estimation of  $r_c$  by taking the gradient of the average value  $\overline{V_z}$  of the radially dependent  $V_z$  profile within the vortex and assuming it to be linear. Figure 3.9(a) and (b) shows the results of the computed  $r_c$  if extra radial diffusion of vorticity due to turbulence is applied as proposed by Odgaard (1986) where  $\nu$  is replaced by  $\nu + k\Gamma_\infty$  with  $k = 10^{-5}$  to use an eddy viscosity in the same order of magnitude as the kinematic viscosity. Indeed, as radial diffusion by turbulence is likely to be absent, the introduction of a small eddy viscosity leads to unrealistic large values of the core radii.

### 3.7 COMPUTATION OF THE AIR CORE DEPTH WITH THE BURGERS MODEL

The computation of  $H_D$  or total surface depression is based on conservation of radial momentum from the Navier-Stokes equations by assuming  $\partial V_r/\partial z = 0$  and neglecting the contribution of the  $V_r$  terms since they are very small compared to the  $V_\theta$  terms as shown in section 3.4. The radial pressure term as a function of  $r$  is then:

$$p(r) = \rho \int_0^r \left[ \frac{V_\theta^2}{r} - V_r \frac{\partial V_r}{\partial r} + \nu \frac{\partial}{\partial r} \left( \frac{\partial V_r}{\partial r} + \frac{V_r}{r} \right) \right] dr \approx \rho \int_0^r \frac{V_\theta^2}{r} dr + p(0) \quad (3.19)$$

and characterizes the balance between radial pressure force and centrifugal force of the rotating fluid. The pressure distribution in the axial direction is determined by taking the integral of the axial Navier-Stokes equations and neglecting the  $V_z$  pressure terms as they are small compared to the pressure due to the gravitational force:

$$p(r) = \rho \int_0^z \left[ V_r \frac{\partial V_z}{\partial r} + V_z \frac{\partial V_z}{\partial z} + \nu \left( \frac{\partial^2 V_z}{\partial r^2} + \frac{1}{r} \frac{\partial V_z}{\partial r} + \frac{\partial^2 V_z}{\partial z^2} \right) - g \right] dz \approx p(0) - \rho g z. \quad (3.20)$$

Consequently, the pressure distribution is taken as hydrostatic as supposed by e.g. Odgaard (1986), Gulliver & Rindels (1987), Hite & Mih (1994) and Anderson *et al.* (2006). When including surface tension, the elevation  $h$  of the free surface is approached by:

$$h(r) = h(0) + \frac{1}{g} \rho \int_0^r \frac{V_\theta^2}{r} dr - \frac{\sigma}{\rho g} [\kappa(r) - \kappa(0)] \quad (3.21)$$



Figure 3.10: Free-surface vortex air core depths  $H_D$  for series 5 to 8 with from left to right:  $H_D = 0.17$  m,  $H_D = 0.26$  m,  $H_D = 0.54$  m and  $H_D = 0.85$  m. All air cores are typically funnel shaped.

with  $\sigma$  the fluid surface tension and  $\kappa$  the surface curvature (Anderson *et al.*, 2006):

$$\kappa(r) = \frac{h'}{r[1+(h')^2]^{1/2}} + \frac{h''}{[1+(h')^2]^{3/2}} \quad (3.22)$$

with  $h' = dh/dr$  and  $h'' = d^2h/dr^2$ . Subsequently,  $H_D$ , or the total surface depression, is approached by integrating equation (3.21) between  $r = 0$  and  $r \rightarrow \infty$  while neglecting the curvature  $\kappa(\infty)$  at infinity:

$$H_D = h(\infty) - h(0) = \frac{1}{g} \int_0^\infty \frac{V_\theta^2}{r} dr - \frac{\sigma}{\rho g} \kappa(0). \quad (3.23)$$

### 3.7.1 INFLUENCE OF SURFACE TENSION

The influence of surface tension  $\sigma$  on  $H_D$  has been studied by many authors. For example, Anwar (1978) stated that the influence of  $\sigma$  can be neglected when the Weber number  $We = \rho U_o^2 H / \sigma > 10^4$ . In our experimental range with  $\sigma = 0.072$  N m<sup>-1</sup> (25 °C),  $We$  varies between  $10^3$  to  $3 \cdot 10^3$  and thus according to Anwar (1978) the surface tension influences the  $H_D$ , however, the relative contribution is unknown. Odgaard (1986) states that the surface tension pressure  $p_s$  at the tip of the air core is of a magnitude of  $-2\sigma/r_c$  giving a maximal contribution to the presented experimental range of circa 1% of the measured  $H_D$ . Suerich-Gulick *et al.* (2014b) numerically examined the relative contribution of surface tension  $\delta = (h_n - h_\sigma)/h_n$  on the air core depth for different scales and shapes of the surface depression as a function of the nominal slope  $\zeta = h_n/r_c$ , where  $h_n$  and  $h_\sigma$  are the calculated  $H_D$  without and with  $\sigma$ . For funnel-shaped air cores (Figure 3.10) with a minimal nominal slope in our

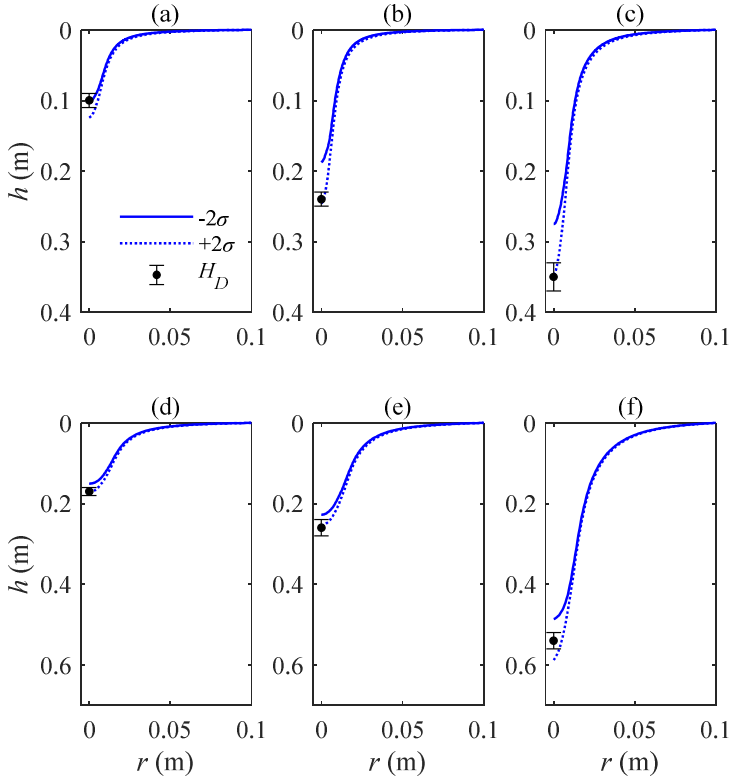


Figure 3.11: (a)-(f) Surface depression profile computed with equation (3.21) and without surface tension and compared with the measured  $H_D$  for series 2 to 7. Both results are presented with the 95% confidence interval.

experimental range of about 10, Suerich-Gulick *et al.* (2014b) showed that the relative contribution has a maximum of about 2%. Because of this minor contribution, the influence of  $\sigma$  in the computation of  $H_D$  is neglected.

### 3.7.2 VALIDATION OF THE EXPRESSION TO COMPUTE THE SURFACE ELEVATION

The Burgers model to quantify  $H_D$  is based on the expression to compute the surface elevation (equation (3.21)) without taking surface tension into consideration. Subsequently, both equation (3.21) and the assumption of negligible surface tension effects are validated by comparing the results of equation (3.21) with the measured  $H_D$ . The comparison uses the measurements of  $V_\theta$  at plane  $h = 0.29$  m. Figure 3.11 shows that equation (3.21) matches with the measured  $H_D$  showing some under-prediction for most of the series that validates neglecting surface tension effects for the presented experimental range.

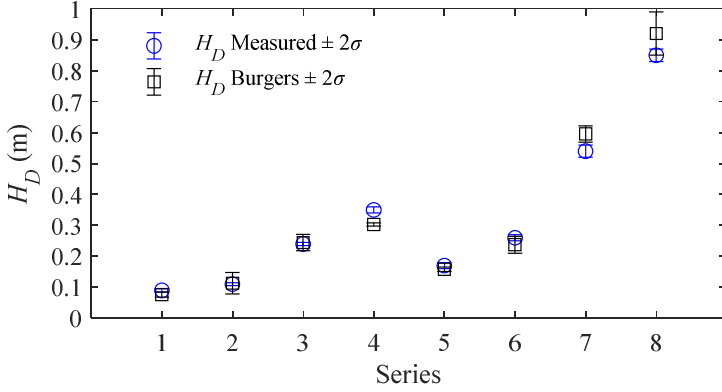


Figure 3.12: Computed air core depth  $H_D$  with the Burgers model (equation (3.24)) compared to measured  $H_D$ . Both results are presented including the 95% confidence interval because the averaged core radius  $\bar{r}_c$  was used and because of uncertainty linked to air core tip instability.

### 3.7.3 COMPUTATION OF THE AIR CORE DEPTH WITH THE BURGERS MODEL

The Burgers model to compute  $H_D$  is obtained by substituting Burgers' expression of  $V_\theta$  in the validated equation (3.21) and integrating over  $r \in [0, \infty]$  while neglecting effects due to  $\sigma$ :

$$H_D = \frac{1}{g} \int_0^\infty \frac{V_\theta^2}{r} dr = \frac{\ln 2}{4\pi^2 g} \left( \frac{\Gamma_\infty}{r_c} \right)^2. \quad (3.24)$$

Figure 3.12 shows the results of the Burgers model using  $\bar{\Gamma}_{SPV}$  and  $\bar{r}_c$  that are the plane averaged values. For series 1 to 6, the Burgers model shown an under-prediction of  $H_D$  while there is an over-prediction of  $H_D$  for series seven and eight. The randomness of the deviations is probably related to a combination of minor inaccuracies in  $\bar{r}_c$  and Burgers' assumption of an unrealistic radially independent  $V_z$  profile. In conclusion, with an uncertainty of approximately 20% the Burgers model produces sufficiently accurate results for the research purposes addressed in this thesis.

## 3.8 CONCLUSIONS

The simple floating quadripod to measure  $\Gamma$  proved to be a simple but accurate measuring device. The profile of  $V_\theta$  is shown to be nearly independent of the vertical coordinate ( $\partial V_\theta / \partial z \approx 0$ ) and thus the rotational flow can be assumed as a 2D line-vortex. Based on the characteristic vortex parameters  $r_c$  and  $\Gamma_\infty$ , where  $\Gamma_\infty$  is assumed to be equal to  $\Gamma$  at  $r = 3r_c$ , the Burgers (1948) vortex model produces a sufficiently accurate estimate of the  $V_\theta$  profile for the present research purposes. The profile of  $V_r$

was hard to measure because of the velocities being in the same order of magnitude as the measurement uncertainty. The radial inflow is primary concentrated near the vortex core with a maximum velocity around  $r_c$  and assumed as zero in the outer field. For all series, the measured  $V_z$  profiles show that the axial down-flow is primary concentrated in a region with a radius comparable to approximately 2 to  $3r_c$  while showing a semi-parabolic profile with a maximum around  $r_c$ . Integration of the measured  $V_z$  shows that between 10% and 25% of the flow is transported by the vortex.

The measurements show that it is valid to use Burgers' model for the computation of  $r_c$  for radially dependent  $V_z$  profiles by using the average  $\overline{V_z}$  over a radial domain of  $2.2r_c$ . Compared to the magnitude of diffusion of vorticity by viscosity the experiments show that there is no considerable radial diffusion by turbulence, see Figure 3.8. The influence of surface tension can be neglected in the computation of  $H_D$  for the present experimental range. By only using  $\Gamma_\infty$  and  $r_c$  and compared with the measured  $H_D$ , the Burgers model computes  $H_D$  with an uncertainty of 20%. The purpose of the vortex' application is to transport floating debris to the pump suction inlet. At the design stage there is a safety margin in distance between  $H_D$  and the inlet depth as air entrainment by a full air core must be prevented. The 20% uncertainty in air core depth is negligible compared to this margin and therefore acceptable for engineering applications.



# 4

## **VORTEX DRIVEN PARTICLE MOTION: HELICAL MOTION ALONG THE AIR CORE**

The main content of this chapter is based on Duinmeijer, S.P.A. & Clemens, F.H.L.R (2019c). (subm.). *Experimental study on free-surface vortex driven particle motion at high Reynolds numbers: helical motion along the air core*. Submitted to *Journal of Hydraulic Research*.

## 4.1 INTRODUCTION

The free-surface vortex driven motion of buoyant particles is determined by the interaction between the particle dynamics at one hand and the vortex flow characteristics on the other hand. The dynamics are determined by the hydrodynamic and body forces acting on the particle. Regarding the stage 1 motion (helical motion along the air core), see Figure 4.1, the motion along the air core is determined by the inertial and lift forces. Even though the lift force is generally insignificant when compared to e.g. the drag force, the particle's motion is strongly influenced by this former force, see for example Figure 4.1. Over the last decades many studies are reported on the motion of bodies in shear and rotating flows in which the generation of drag and lift forces are involved. For example, Saffman (1965, 1968) and Mei (1991) studied the lift force on a sphere in a pure shear flow for low particle Reynolds numbers  $1 \ll Re_p \leq 100$  with  $Re_p$  defined as  $(|\mathbf{V} - \mathbf{U}|)L/\nu$  where  $\mathbf{V}$  and  $\mathbf{U}$  are the flow and particle velocities respectively,  $L$  is the sphere diameter and  $\nu$  is the fluid's kinematic viscosity. Auton (1987) studied the lift force on a fixed sphere in an inviscid weak shear flow ( $Re_p \rightarrow \infty$ ). Auton *et al.* (1988) derived a general expression of the fluid force on a moving sphere in an inviscid fluid with a non-uniform rotational velocity field and showed that the lift force is made up by an inertial/added-mass and a rotational component. For  $10 < Re_p < 100$ , Bagchi & Balachander (2002) studied the lift coefficient  $C_L$  of a sphere in a linear shear flow and in a vortex and showed that for the latter flow  $C_L$  is approximately two orders of magnitude higher even at equal vorticity. Van Nierop *et al.* (2007) studied the lift forces on a  $\varnothing 1$  mm air bubble in a solid-body rotating flow for  $0.01 < Re_p < 500$ . Bluemink *et al.* (2009) examined  $C_L$  for a freely rotating buoyant  $\varnothing 4$  mm sphere in a solid-body rotating flow for  $2 \leq Re_p \leq 1060$ . Fukada *et al.* (2014) examined the hydrodynamic forces acting on a sphere that generates the rotation of particles in both irrotational as solid-body rotating flow for  $5 < Re_p < 100$ . Voßwinkel (2017) studied the free-surface vortex transportability of spherical particles with diameters ranging from  $\varnothing 3$  to  $\varnothing 40$  mm for a specific flow geometry. Based on experimental research, Voßwinkel determined correlations between downward motion and the intake hydraulic boundary conditions and particles characteristics. However, the characteristics of the free-surface vortex 3D-flow field are not considered and so the outcome of the research is limited to just one specific intake geometry.

In this thesis and when compared to the literature mentioned, the characteristic particle length  $L$  (0.02 to 0.04 m) is large relative to spatial changes in the surrounding flow. For the stage 1 motion, with differences between the SPIV measured  $V_\theta$  and 2D/3D-PTV measured  $U_\theta$  in the range of approximately 0.005 to 1 m s<sup>-1</sup>, the experimental  $Re_p$  range is  $\sim 10^2 < Re_p < \sim 10^4$ . Furthermore, the stage 1 particle motion also occurs

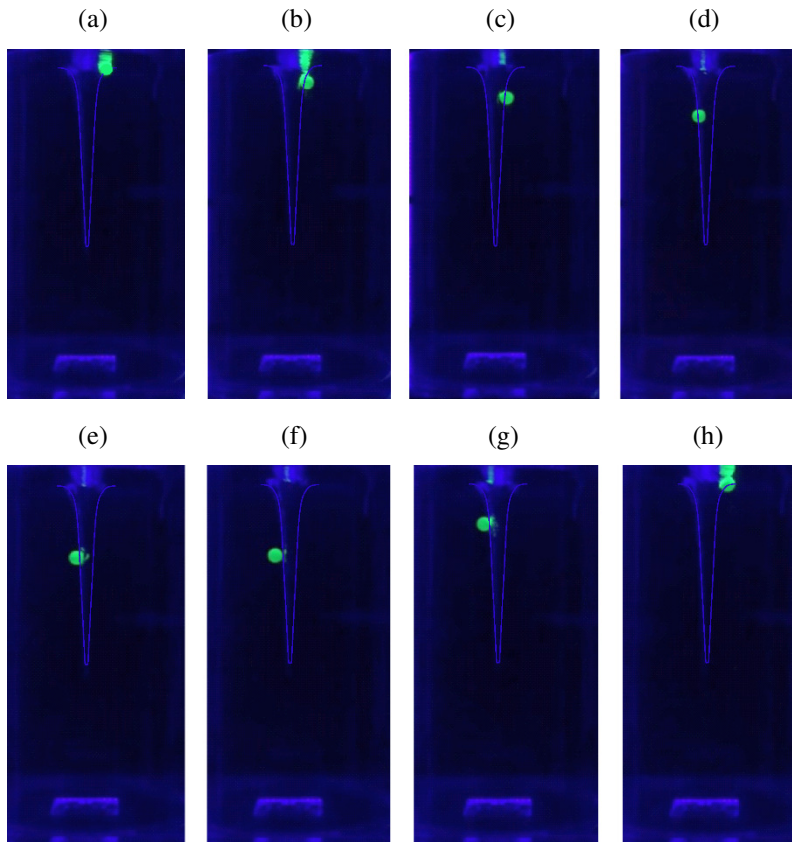


Figure 4.1: 3D-PTV recordings of the stage 1 motion. In this example with sphere 86 at series 7, the sphere starts with the downward helical motion along the air core, see figures (a)-(d). At some height and assumed as due to an unbalance between the lift and inertial forces, the motion changes to an upward motion that ends at the surface, see figures (e)-(h).

in the irrotational part of the vortex flow while the studies reported in literature mainly focus on the motion in shearing flows like solid-body rotating flow. Hence, there is less numerical and experimental data on particle motion in irrotational flows. Consequently, the results from literature are not directly applicable to study the stage 1 particle motion. In this research measurements are conducted to obtain experimental data and knowledge on the stage 1 motion for  $\sim 10^2 < Re_p < \sim 10^4$ . A mathematical model is proposed for a qualitative analysis of the vortex driven particle motion in stage 1. In conclusion, a motion parameter is proposed to provide a first indication of a continuous downward motion along the air core.

The outline of this chapter is as follows: section 4.2 addresses the mathematical

model. Section 4.3 addresses the experimental set-up and program. In section 4.4 and 4.5 the experimental results and the model results are discussed. Section 4.6 addresses the conclusions.

## **4.2 MATHEMATICAL MODEL OF THE FREE-SURFACE VORTEX DRIVEN PARTICLE MOTION**

### **4.2.1 INTRODUCTION**

Visual analysis of the initial experimental results revealed that the experiments showed a high degree of non-repeatability. This is a first indication of chaotic behavior in the vortex driven particle motion which is of major importance of the predictability of the particle motion. To study and quantify this behavior, a mathematical model is developed that describes the particle motion in the two-dimensional (2D) horizontal plane. The motion is described in a Cartesian coordinate system where the  $z$ -axis is pointing in upward vertical direction, see Figure 4.2. Based on the Lagrangian approach, the set of non-linear particle motion equations are numerically solved using a trust-region-dogleg algorithm (e.g. see Powell, 1970).

### **4.2.2 MODEL LIMITATIONS**

In the vortex driven particle motion, the particle moves between an irrotational flow field ( $\omega_z = 0$ ) and a solid-body rotation flow field ( $\omega_z \neq 0$ ). As  $L$  is large compared to the spatial gradient in the flow velocity, the particle can experience both types of flow field at the same moment. The model is therefore limited to particle lengths in the same order of twice the vortex core radius:  $2r_c/L \approx O(1)$ . For the sake of simplicity, it is assumed that the flow field is not influenced by the particle. In literature, theoretical descriptions of the mutual influence of vortices and bodies in a vortex flow field are found (e.g. Roenby & Aref, 2010). However, these studies are limited to idealized situations (2D bodies and 2D flow fields in an ideal fluid). Forces due to surface tension at the solid-fluid-air interface, that may occur when the body is partially submerged, are neglected. Consequently, the model is not expected to result in a perfect match with the experimental results obtained.

### **4.2.3 2D APPROACH**

The air core interface is interpreted as a curved solid boundary that guides the ‘far field’ horizontal particle motion to a 3D motion along the interface where the particle is in radial direction partly ‘pushed’ through the interface towards the center, see Figure 4.2(b). A first approach is that the vertical motion is generated by an axial drag

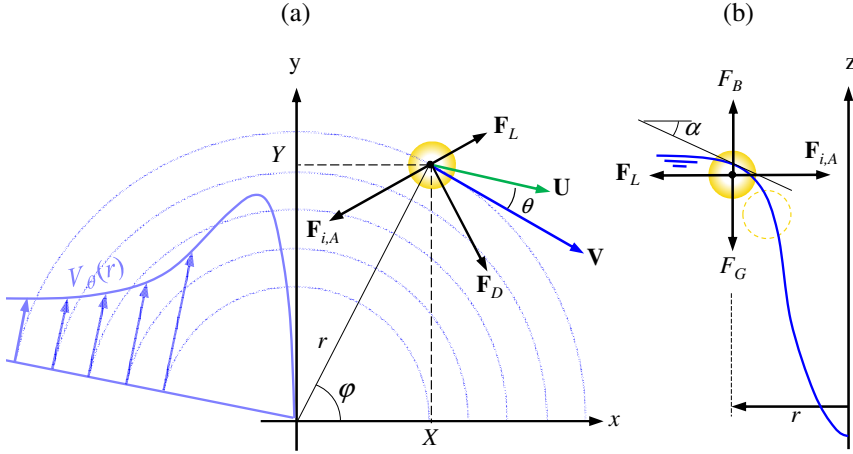


Figure 4.2: (a) Motion in the horizontal plane and (b) the vertical plane along the air core.  $\mathbf{F}_D$ ,  $\mathbf{F}_L$  and  $\mathbf{F}_{i,A}$ ,  $F_G$  and  $F_B$  are the drag, lift, inertial/added-mass, gravity and buoyancy forces respectively. The left side of (a) shows a schematic profile of  $V_\theta(r)$ .

force  $F_{D,z}$  due to the axial velocity component of the vortex flow along the interface. However, and based on measurements of the flow rate along the interface (Duinmeijer *et al.*, 2019b) and by applying the uniform drag force approach ( $F_{D,z} \sim \rho_f C_D A_N (V_z - U_z)^2$ ),  $F_{D,z}$  is shown to be orders of magnitude smaller than the upward force  $F_B - F_G$ . Consequently, the observed vertical motion must be generated by other processes. The responsible mechanism is assumed to be the decrease in buoyancy force  $F_B$  when the particle is due to the inertial force partly pushed through the interface until  $F_B < F_G$  and the particle slides down along the air core. The sliding motion deaccelerates the horizontal motion towards the vortex center giving the horizontal lift force  $F_L$ , generated by the Magnus effect and vorticity as discussed later, more time to grow in magnitude. This condition is approximated in the mathematical 2D-model by a reduction of the calculated distance  $\mathbf{X}$ :

$$\frac{d\mathbf{X}}{dt} = \cos(\alpha) \mathbf{U}. \quad (4.1)$$

with  $\alpha$  the angle of the deflection and taken equal to the tangent line of the interface curvature, see Figure 4.2(b):

$$\tan(\alpha) = \frac{dH_D}{dr} = d \left( \frac{1}{g} \int_{r_1}^{r_2} \frac{V_\theta^2}{r} dr \right) / dr = \frac{1}{g} \frac{V_\theta^2}{r}. \quad (4.2)$$

The ‘sliding’ condition effects only the motion towards the vortex center; there is no constraint incorporated in the model for the outward motion.

#### 4.2.4 GENERAL EQUATION OF PARTICLE MOTION

At moderate to large Reynolds numbers and for an inertial frame of reference, the generalized equation of motion for a body with volume  $\chi$  moving with velocity  $\mathbf{U}$  through an ambient non-uniform flow with velocity  $\mathbf{V}$  is (see e.g. Tio, 1993, Van Nierop *et al.*, 2007, Bluemink, 2009):

$$(\rho_p + C_A \rho_f) \chi \frac{D\mathbf{U}}{Dt} = \rho_f (1 + C_A) \chi \frac{D\mathbf{V}}{Dt} + \mathbf{F}_D + \mathbf{F}_L + \mathbf{F}_g. \quad (4.3)$$

For a spherical body Appendix E displays the full written equation. The terms on the right side are the forces acting on the body: (1) the inertial force due to the fluid acceleration  $D\mathbf{V}/Dt$ , (2) the hydrodynamic drag force  $\mathbf{F}_D$ , (2) the hydrodynamic lift force  $\mathbf{F}_L$  and (3) the body force  $\mathbf{F}_g$  due to gravity. Centrifugal and Coriolis forces are not considered as the motion is relative to an inertial reference system and the history or Basset force is considered to be insignificant for  $Re_p > 5$  (Van Nierop *et al.*, 2007) and is neglected as in this study  $10^2 < Re_p < 10^4$ . During the vertical motion along the air core, interaction of the particle with its own wake is assumed as negligible.

#### 4.2.5 INERTIAL FORCE

The inertial force  $\mathbf{F}_{i,A}$  is due to the acceleration of the unperturbed fluid at the sphere's center:

$$\mathbf{F}_{i,A} = \rho_f (1 + C_A) \chi \frac{D\mathbf{V}}{Dt} = \rho_f (1 + C_A) \left( \chi \frac{\partial \mathbf{V}}{\partial t} + \mathbf{V} \cdot \nabla \mathbf{V} \right). \quad (4.4)$$

For a stationary flow ( $\partial/\partial t = 0$ ) and in Cartesian coordinates these forces are:

$$\begin{aligned} F_{i,A,x} &= \rho_f (1 + C_A) \chi \left( V_x \frac{\partial V_x}{\partial x} + V_y \frac{\partial V_x}{\partial y} + V_z \frac{\partial V_x}{\partial z} \right) \\ F_{i,A,y} &= \rho_f (1 + C_A) \chi \left( V_x \frac{\partial V_y}{\partial x} + V_y \frac{\partial V_y}{\partial y} + V_z \frac{\partial V_y}{\partial z} \right) \\ F_{i,A,z} &= \rho_f (1 + C_A) \chi \left( V_x \frac{\partial V_z}{\partial x} + V_y \frac{\partial V_z}{\partial y} + V_z \frac{\partial V_z}{\partial z} \right). \end{aligned} \quad (4.5)$$

The added mass coefficient  $C_A$  accounts for the fluid's inertia close to the sphere with  $C_A = 0.5$  for a submerged sphere in a fluid of infinite extent. For a floating sphere the effect of the free-surface is to decrease the  $C_A$ . For example, Berklite (1972) found for a sphere that  $C_A \approx 0.4$  for  $h/a = 1$  and  $C_A \approx 0.19$  for  $h/a = 0.5$  (applied in this thesis) with  $h$  the distance between the surface and the sphere's center.

#### 4.2.6 DRAG FORCE

For  $Re_p \gg 1$  the equation of the drag force on a body moving through a fluid is expressed as:

$$\mathbf{F}_D = 0.5\rho_f C_D A_N (\mathbf{V} - \mathbf{U})(|\mathbf{V} - \mathbf{U}|). \quad (4.6)$$

For a sphere moving not parallel to the rotation axis in a rotating flow, the drag coefficient  $C_D$  is quantified by the empirical expression suggested by Holzer & Sommerfeld (2008):

$$C_D = \frac{24}{Re_p} + \frac{3}{\sqrt{Re_p}} + 0.42. \quad (4.7)$$

Equation (4.7) produces approximately equal results as the results presented by Fukada *et al.* (2014) while  $C_D$  is not significantly affected by the particle rotation (Bluemink *et al.*, 2008).

#### 4.2.7 FLOW VORTICITY INDUCED LIFT FORCE

In this research the hydrodynamic lift force consists of two components: a lift force induced by the flow vorticity and a lift force due to the particle's rotation. For  $Re_p \gg 1$  the vorticity lift force  $\mathbf{F}_{L,\omega}$  is (see e.g. Auton *et al.*, 1988 and Bluemink *et al.*, 2009):

$$\mathbf{F}_{L,\omega} = \rho_f \chi C_L (\mathbf{V} - \mathbf{U}) \times \boldsymbol{\omega}. \quad (4.8)$$

Assuming only vorticity in the  $z$ -direction, there is only a lift force  $F_{L,\omega}$  in the horizontal plane:

$$F_{L,\omega} = \rho_f \chi C_L (\mathbf{V} - \mathbf{U}) \omega_z. \quad (4.9)$$

A number of experimental and numerical studies determining the lift coefficient  $C_L$  as function of the flow type are found in literature, see Table 4.1. Van Nierop *et al.* (2007) stated that the influence of the sphere's rotation (i.e. the 'Magnus' lift) on  $C_L$  is significant and not addressed for  $Re_p \gg 1$ . Bluemink *et al.* (2009) examined the effect of the sphere's rotation on  $C_L$  for  $Re_p \leq 200$  and proposed a linear decoupling of  $C_L$  in a flow vorticity contribution ( $C_{L,\omega}$ ) and Magnus lift contribution ( $C_{L,\Omega}$ ). Based on numerical data,  $C_{L,\omega}$  is parametrized as:

$$C_{L,\omega} = 0.51 \cdot {}^{10}\log(Re_p) - 0.22. \quad (4.10)$$

Bluemink *et al.* (2009) assumed the decoupling to be also valid for  $Re_p \gg 200$ , so equation (4.10) is applied in the model under consideration with limiting values for

Table 4.1: Experimental and numerical studies to determine the vorticity lift coefficient  $C_L$ .

Authors	Flow type	Shape	$Re_p$	Results
Auton (1987)	Inviscid weak shear flow	Fixed sphere	$\rightarrow \infty$	$C_L = 0.5$
Auton (1988)	Inviscid solid-body rotating	Cylinder at rest	$\rightarrow \infty$	$C_L = 1$
Tio <i>et al</i> (1993)	Stuart vortex	Sphere	$\gg 1$	$C_L = 0.5$
Bagchi and Balachandar (2002)	Solid-body rotating	Sphere	10-100	$C_L = 2 C_{L, \text{shear flow}}$
Van Nierop <i>et al.</i> (2007)	Solid-body rotation	Rotating sphere	$\gg 1$	$C_L = 0.5$
Bluemink <i>et al.</i> (2009)	Solid-body rotation	Rotating sphere	$\leq 200$	see equation (4.10)

$C_{L,\omega}$  between  $\sim 0.8$  and  $\sim 1.8$ . For the vortex  $\omega_z$  depends on the radius due to the viscous diffusion and is computed by Burgers' expression of  $\omega_z(r)$ , see equation (3.10) and thus  $F_{L,\omega}$  is:

$$F_{L,\omega} = \frac{\rho_f \chi C_{L,\omega} (\mathbf{V} - \mathbf{U}) \Gamma_\infty}{\pi r_c^2} \exp \left[ - \left( \frac{r}{r_c} \right)^2 \right]. \quad (4.11)$$

Equation (4.11) is valid for rotational flow with uniform vorticity. The non-uniformity of Burgers vorticity equation is assumed to be linear. Therefore, the vorticity at the location  $r$  of the sphere's center is taken as the average value over the distance  $r - 0.5L$  to  $r + 0.5L$ .

#### 4.2.8 PARTICLE'S ROTATION LIFT FORCE (MAGNUS FORCE)

The Magnus lift force is generated by the particle's rotation  $\Omega_p$  that generates a rotating layer of fluid around the particle resulting in a non-symmetric velocity field around the particle. The derivation of  $F_L$  acting on a sphere starts with the derivation of  $F_L$  acting on a cylinder:

$$F_L = \int_0^s p(r = a, \phi) \sin(\phi) ds = \int_0^{2\pi} p(\phi) \sin(\phi) a d\phi \quad (4.12)$$

where  $\phi$  is the angle with a relative flow velocity  $(\mathbf{V} - \mathbf{U})$ . For a rotating sphere in an irrotational flow  $p(\phi)$  can be determined with the potential flow theory. For a rotating cylinder (applying cylindrical coordinates) the velocity potential  $\Phi$  is (see e.g. Batchelor, 1967):

$$\Phi(r, \theta) = -(\mathbf{V} - \mathbf{U}) \left( r + \frac{a^2}{r} \right) \cos(\phi) + \frac{\Gamma_p \theta}{2\pi}. \quad (4.13)$$

$\Gamma_p$  is the flow circulation around the cylinder due to  $\Omega_p$ :

$$\Gamma_p = 2\pi a^2 \Omega_p. \quad (4.14)$$

The tangential velocity  $u_{a,\theta}$  at the particle surface is:

$$u_{a,\theta} = \left( \frac{1}{r} \frac{\partial \Phi}{\partial \theta} \right)_{r=a} = 2(\mathbf{V} - \mathbf{U}) \sin(\phi) + \frac{\Gamma_p}{2\pi a}. \quad (4.15)$$

As for potential flow the viscous forces are neglected,  $p(\phi)$  is quantified by applying the Bernoulli theorem:

$$p(\phi) = p_o + \frac{1}{2} \rho_f \left[ (\mathbf{V} - \mathbf{U})^2 - \left( 2(\mathbf{V} - \mathbf{U}) \sin(\phi) + \frac{\Gamma_p}{2\pi a} \right)^2 \right]. \quad (4.16)$$

By substituting equation (4.16) in equation (4.12), the lift force on a cylinder per unit length and perpendicular to the flow direction is (the Kutta-Joukowski Lift Theorem):

$$\begin{aligned} F_{L,\Omega_p} &= \int_0^{2\pi} \left( p_o + \frac{1}{2} \rho_f \left[ (\mathbf{V} - \mathbf{U})^2 - \left( 2(\mathbf{V} - \mathbf{U}) \sin(\phi) + \frac{\Gamma_p}{2\pi a} \right)^2 \right] \right) \sin(\phi) a d\phi \\ &= \rho_f (\mathbf{V} - \mathbf{U}) \Gamma_p. \end{aligned} \quad (4.17)$$

Equation (4.17) is transformed to an expression for a sphere by integrating along the sphere's rotation axis from  $[-a, a]$  with  $l = a \cos(\gamma)$  the length along the axis,  $r = a \sin(\gamma)$  the radius of an infinite small cylinder and  $\gamma$  the angle from the sphere's center along the rotation axis:

$$F_{L,\Omega_p} = \rho_f (\mathbf{V} - \mathbf{U}) 2\pi \Omega_p a^3 \int_0^\pi (\sin(\gamma))^3 d\gamma = 2\rho_f \chi (\mathbf{V} - \mathbf{U}) \Omega_{p,z}. \quad (4.18)$$

The rotating vortex flow is approached as being uniform by taking  $(\mathbf{V} - \mathbf{U})$  at the center of the body (Fukada *et al.*, 2014). The particle needs rotation to generate  $F_{L,\Omega_p}$ . For irrotational flows, studies of i.e. Bagchi & Balachandar (2002), Bluemink *et al.* (2008) and Fukada *et al.* (2014) showed the rotation of a sphere and thus the presence of a torque due to an asymmetric stress distribution along the sphere's surface. Indeed, for the present study, the existence of a torque in the irrotational vortex flow is confirmed by measurements of  $\Omega_p$  that show that  $ld\Omega_p/dt > 0$ , see for example Figure 4.3. The equation of particle rotation motion is:

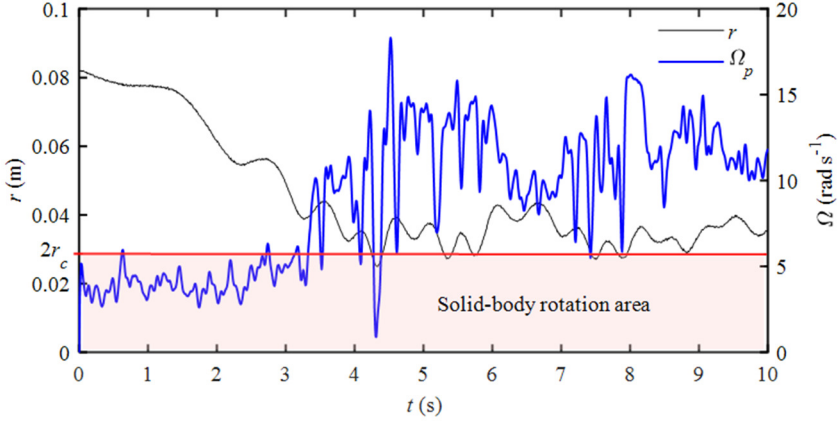


Figure 4.3: 2D-PTV measured  $\Omega_p$  and the radial location  $r$  for exp. 86-5. Despite the noisy results there is generation of angular velocity  $\Omega_p$  in the irrotational flow field ( $r > 2r_c$ ).

$$\frac{d\Omega_p}{dt} = \frac{T_p}{I_p}. \quad (4.19)$$

$T_p$  is the torque on the particle and  $I_p$  is the particle moment of inertia:

$$T_p = a \int_{A_s} \tau_{a,\theta} dA_s. \quad (4.20)$$

For a sphere in an irrotational vortex flow, Fukada *et al.* (2014) proposed an expression for  $T_p$  as a function of the streamline curvature  $\kappa$  and determined for  $5 \leq Re_p \leq 100$  with  $r \geq 30L$ :

$$T_p = \frac{\rho_f}{2} \left( \frac{L}{2} \right)^5 C_T (\Omega_{p,st} - \Omega_p) (|\Omega_{p,st} - \Omega_p|). \quad (4.21)$$

$\Omega_{p,st}$  is the steady angular velocity as function of  $\kappa$  (Fukada *et al.*, 2014):

$$\Omega_{p,st} = 0.0554 (\mathbf{V} - \mathbf{U}) \kappa Re_p^{0.635}. \quad (4.22)$$

The torque coefficient  $C_T$  is (Fukada *et al.*, 2014):

$$C_T = 239 \left( \frac{L^2 (|\Omega_{p,st} - \Omega_p|)}{\nu} \right)^{-0.956}. \quad (4.23)$$

The equation of particle rotation is then:

$$\frac{d\Omega_p}{dt} = \frac{239\rho_f V^{0.956} L^{3.088}}{I_p 64} (\Omega_{p,st} - \Omega_p) (|\Omega_{p,st} - \Omega_p|)^{0.044}. \quad (4.24)$$

In Fukada *et al.* (2014), equation (4.22) is verified for  $5 \leq Re_p \leq 10^2$  and  $\kappa < 1/30L$  where in the presented study it holds that  $10^2 \leq Re_p \leq 5 \cdot 10^3$  and  $\sim 1/L \leq \kappa \leq \sim 1/12L$ . However, Fukada's results indicate that their findings are valid for a much higher range of  $Re_p$ . The validity of equation (4.22) for larger curvatures than  $\kappa = 1/30L$  is unknown.

### 4.3 EXPERIMENTAL PROCEDURE AND PROGRAMME

#### 4.3.1 EXPERIMENTAL PROCEDURE

The motion of the particles in stage 1 is measured by 2D-PTV and 3D-PTV. The first method is applied to measure the motion of the particle at the free-surface and in the horizontal plane. The second method is applied to measure the motion of the submerged particle in both the horizontal and vertical plane. The experimental procedure for the experiments was as follows: prior to starting the measurements, care was taken to obtain a stationary free-surface vortex. This was validated by comparing the air core depth  $H_D$  with the  $H_D$  for the known stationary situation. Starting with an initial situation of no-flow this could take up to maximum 15 minutes. Then the room lights were shut off, the UV-lights and the camera(s) activated and the particle was released on the water surface by hand for the 2D-PTV experiments and by using the remote-controlled device for the 3D-PTV experiments, see Figure 2.2(d). When the particle disappeared through the outlet the experiment was finished. When the particles showed a repeating motion like entering the air core, ejecting out the air core and entering the air core again, the sequence was recorded a few times to check the consistency of this behavior.

#### 4.3.2 EXPERIMENTAL PROGRAMME

The 3D-PTV experimental programme comprised 8 series of mutually different vortex characteristics (series 1 to 8) and 15 experimental particles, see Table 2.3 (except particles 71, 83, 84, 91 and 92), with mutually different characteristics. So, a total of 120 experiments (that were repeated 5 time each) were executed. The vortex characteristics are the circulation  $\Gamma_\infty$  and the core radius  $r_c$ , see Table 3.1. The 2D-PTV experimental programme comprised of 6 series of different vortex characteristics (series 1 and 3 to 7) and 5 spherical particles (particles 86, 88, 101, 102 and 103). So, a total of 30 experiments (that were repeated 2 time each) were executed. The experimental conditions for both the 2D- and 3D-PTV experiments are presented by the particle number followed by the series number, for example: 'exp. 86-4'.

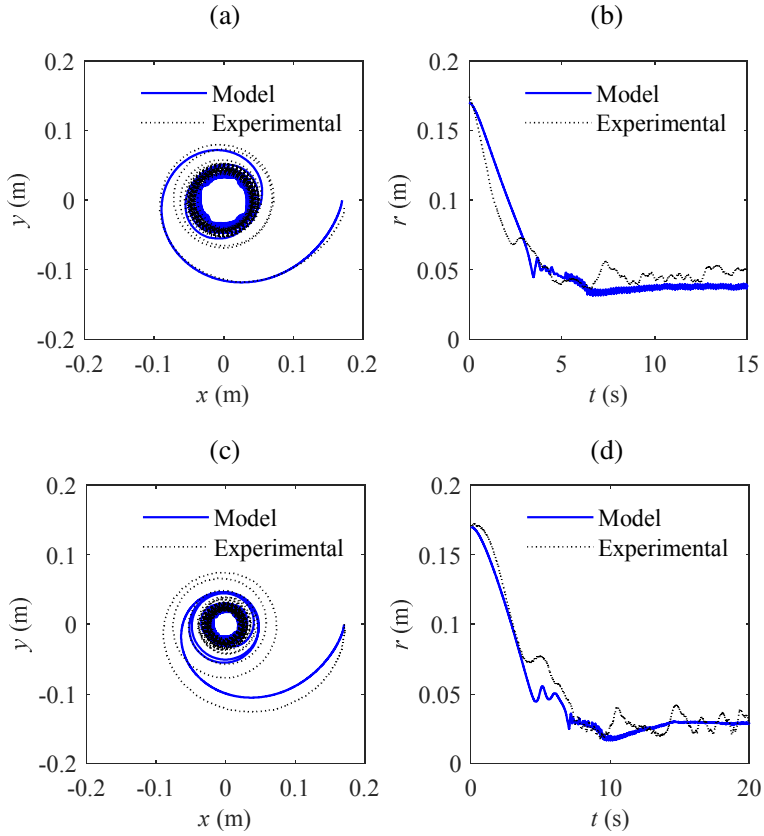


Figure 4.4: (a)-(b) Model and experimental particle motion and radial position of exp. 86-6 with  $\mathbf{X}_{p,0} = [0.18, 0, 0, -0.21V_\theta, 0.21]$ . (c)-(d) Results of exp. 86-3 with  $\mathbf{X}_{p,0} = [0.17, 0, 0, 0.27V_\theta, 0.09]$ .

## 4.4 EXPERIMENTAL RESULTS

### 4.4.1 EVALUATION OF THE MATHEMATICAL MODEL

The model is evaluated by comparing the experimental particle motion with the model motion. This section addresses the comparison for exp. 86-3 and exp. 86-6, see Figure 4.4, where the comparison with other experiments shows similar results. The model uses the initial particle conditions  $\mathbf{X}_{p,0} = [x_0, y_0, V_{x,0}, V_{y,0}, \Omega_{p,0}]$  i.e. the initial position, velocity and angular speed and based on measurements. The values of  $\Omega_{p,0}$  were measured with a relatively large uncertainty. It was verified for each experiment that

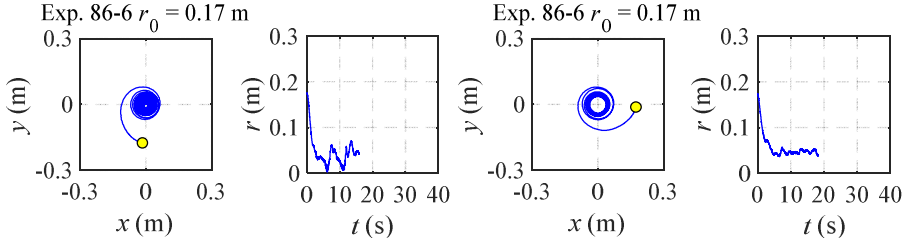


Figure 4.5: Measured motion and radial position of exp. 86-6. Left graphs:  $x_0, y_0 = [0, -0.17]$ . Right graphs:  $x_0, y_0 = [0.17, 0]$ .

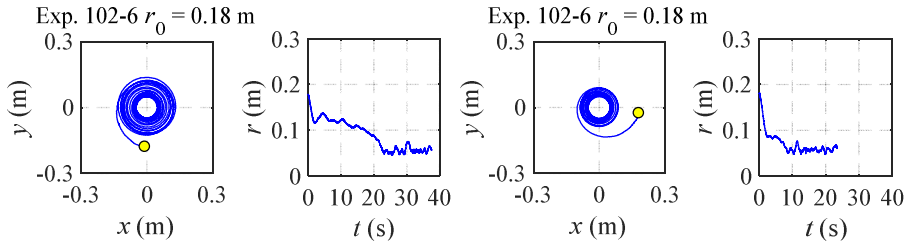


Figure 4.6: Measured motion and radial position of exp. 102-6. Left graphs:  $x_0, y_0 = [0, -0.17]$ . Right graphs:  $x_0, y_0 = [0.17, 0]$ .

$\Omega_{p,0} \ll 1 \text{ rad s}^{-1}$ . The model shows a similarity with the experiments in the sense that both the experiments and the model show that the particle ends up in either orbiting the air core at a more or less constant radial distance or the particle ends up in the vortex core. Based on this similarity the model is assumed as applicable for a qualitative study of the chaotic behavior of the vortex driven particle motion. However, on a small-time scale (i.e. comparing measured and modelled time series on position), experimental and model results show significant differences. Attempts to calibrate the model's parameters proved to be not feasible in the sense that the RMSE between experiment and model can be reduced to zero but at the same time the bias of the calibrated model was high, implying that either some processes are missing from the model and/or information from the experiments is missing. For example: (1) the model uses an approximation to incorporate the effect of the curved air-core, see 4.2.3. (2) The applied potential flow theory to calculate the rotation lift force  $F_{L,\Omega_p}$  is a proper approximation without the occurrence of a (symmetric) downstream wake with shed vorticity due to boundary layer separation. But in the presented study flow separation can occur which effects the particle rotation. (3) The torque equation is validated for  $\kappa > 1/30L$  where the model uses  $\sim 1/12L \leq \kappa \leq \sim 1/L$ . (4) The model does not consider forces due to surface tension and the generation of free-surface waves and forces generated by the interaction between particle and flow at the particle release in the undisturbed flow field.

#### 4.4.2 LIMITED REPEATABILITY OF THE EXPERIMENTAL PARTICLE MOTION

Analysis of the 2D-PTV measured particle motion conducted at controlled conditions but different initial positions of particle release showed significant differences between the motion of the particles. Appendix C shows all the 2D-PTV measured motions in the horizontal plane. Consequently, there is a certain non-repeatable behavior of the experiments. As an example, Figure 4.5 shows the measured motion of a  $\varnothing 38$  mm sphere. In the first experiment the sphere was released at  $[x_0, y_0] = [0 \text{ m}, -0.17 \text{ m}]$  and in the second experiment the sphere was released at  $[0.17 \text{ m}, 0 \text{ m}]$  while the rest of the conditions were identical. In the first experiment (left two graphs), the sphere reached the air core bottom after  $\sim 5$  s and subsequently the sphere was ejected. In the second experiment (right graphs), the sphere ended in a stable limit cycle at  $r \approx 0.05$  m. Another obvious example of the non-repeatable behavior is shown in Figure 4.6. In the first experiment a  $\varnothing 25$  mm sphere was released at  $[0 \text{ m}, -0.18 \text{ m}]$  and in the second experiment at  $[0.18 \text{ m}, 0 \text{ m}]$ . Both experiments show a stable limit cycle at  $r \approx 0.05$  m but in the first experiment this cycle was reached at  $t = \sim 22$  s where in the second experiment the cycle was reached at  $t = \sim 8$  s. The observed chaotic behavior is not uncommon in non-linear dynamical systems.

#### 4.4.3 ANALYSIS OF THE PREDICTABILITY BY APPLYING PHASE PORTRAITS

The predictability and the related chaotic behavior of the vortex driven particle motion is examined by a visual analysis of phase portraits. The mathematical model's phase portraits presented here are constructed by using the initial conditions of radial position  $r_0$ , radial velocity  $U_{r,0}$  and particle rotation  $\Omega_{p,0}$  with ranges  $r_0 = 0.02$  to  $0.30$  m,  $U_{r,0} = -1.0$  to  $1.0$  m s<sup>-1</sup> and  $\Omega_{p,0} = 0$  and  $1.5$  rad s<sup>-1</sup> and for two spheres  $\varnothing 25$  and  $\varnothing 38$  mm. Figure 4.7 and Figure 4.8 show the phase portraits including 4 streamlines with different start conditions  $r_0$  and  $U_{r,0}$  and illustrated by a blue dot. Depending on the initial conditions the sphere can move to a 'stable' limit cycle with radius  $r \approx 0.03$  m and  $r \approx 0.025$  m for the  $\varnothing 38$  and  $\varnothing 25$  mm spheres respectively. This cycle attracts neighbouring trajectories and is defined as an *attractor*. On the other hand, the sphere can move in an 'unstable' limit cycle with increasing radius. This cycle repels trajectories and is thus a *repellor*. For the presented example, Table 4.2 show the system behavior for the given initial condition. For a more realistic  $\Omega_{p,0}$  in the range of 0 to  $0.5$  rad s<sup>-1</sup> Figure 4.9 shows for the conditions of exp. 86-6 all the characteristic model streamlines including two experimental streamlines represented by the dotted lines. The deviations between these lines indicates the limited repeatability of the particle motion. When compared to the model's stable limit cycle, the experimental streamlines show multiple limit cycles. This is due to a vertical motion of the sphere along the air core, see Figure 4.9(d). Hence, there is no unique stable limit cycle. Furthermore, a nice feature is the shift of the position of the saddle-point with

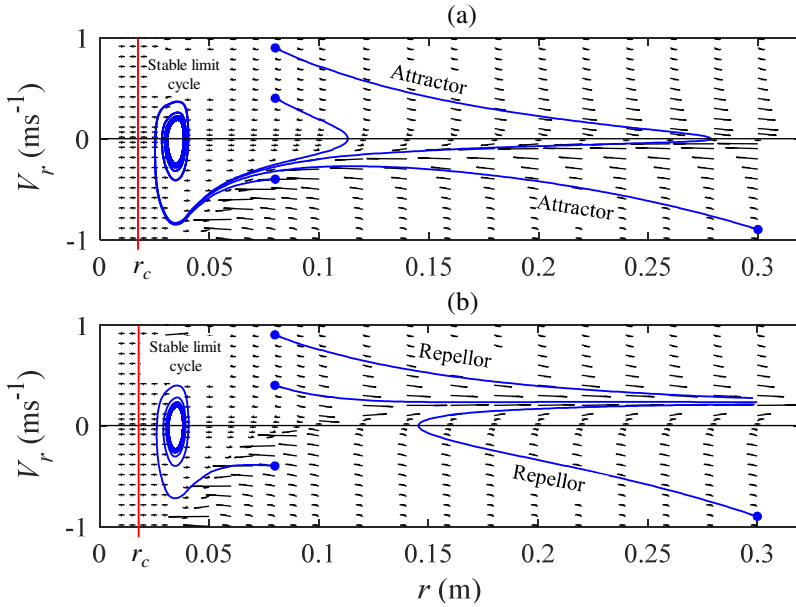


Figure 4.7: Mathematical model phase-portraits for exp. 86-6. (a) Model results for  $\Omega_{p,0} = 0 \text{ rad s}^{-1}$ . (b) Model results for  $\Omega_{p,0} = 1.5 \text{ rad s}^{-1}$ .

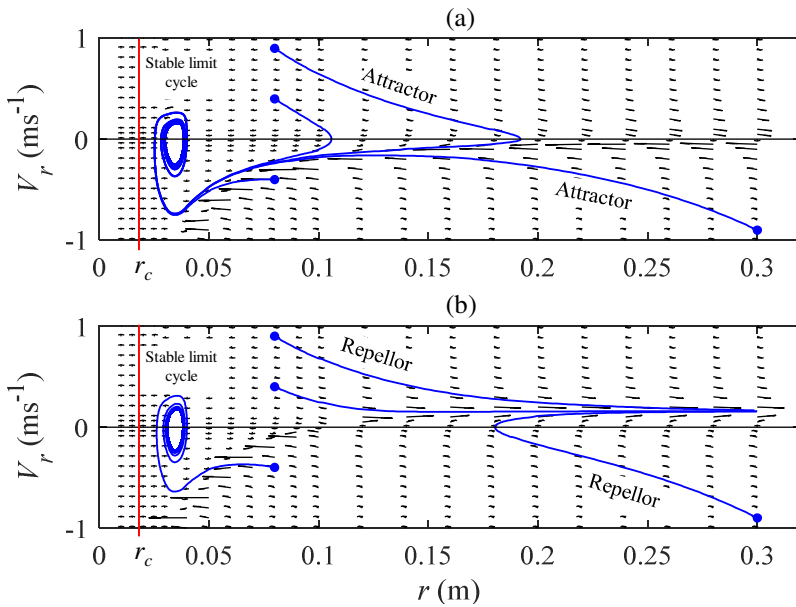


Figure 4.8: Mathematical model phase-portraits for exp. 101-6. (a) Model results for  $\Omega_{p,0} = 0 \text{ rad s}^{-1}$ . (b) Model results for  $\Omega_{p,0} = 1.5 \text{ rad s}^{-1}$ .

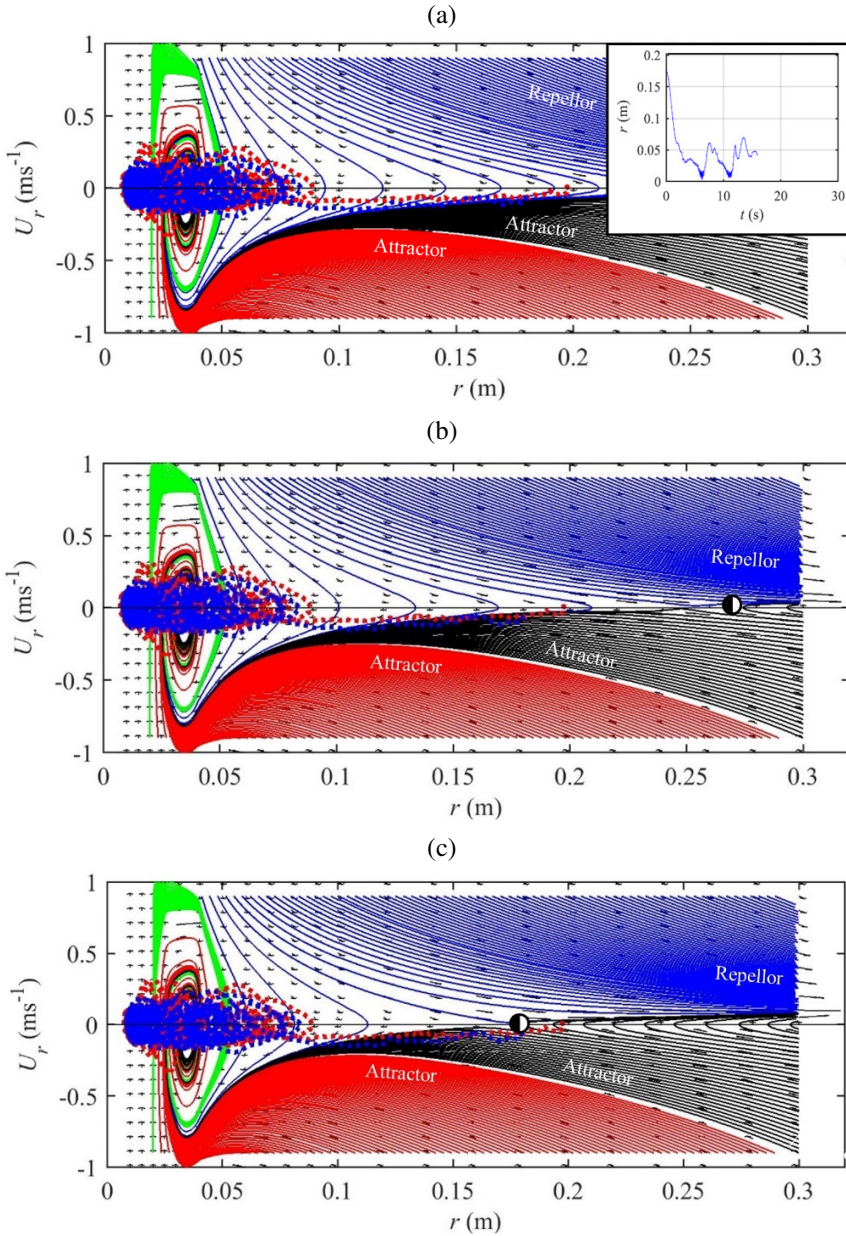


Figure 4.9: Model phase portraits and streamlines for exp. 86-6 with three different initial sphere rotations. The saddle points are indicated by the symbol  $\bullet$ . (a)  $\Omega_{p,0} = 0 \text{ rad s}^{-1}$ . (b)  $\Omega_{p,0} = 0.2 \text{ rad s}^{-1}$ . (c)  $\Omega_{p,0} = 0.5 \text{ rad s}^{-1}$ . The blue and red dotted lines represent the streamlines derived from the measurements and showing multiple limit cycles. This is due to the up-en down motion of the sphere along the air core as showed in the subfigure of (a). Hence, the measurements show a non-stable limit cycle.

Table 4.2: System behavior based on the analysis of mathematical model phase-portraits.

$r_0$ (m)	$U_{r,0}$ (m s <sup>-1</sup> )	$\Omega_{p,0}$ (rad s <sup>-1</sup> )	Behavior of the system at series 6	
			Ø38 mm (sphere 86)	Ø25 mm (sphere 101)
0.08	0.90	0	repellor	attractor
0.08	0.40	0	attractor	attractor
0.30	-0.90	0	attractor	attractor
0.08	0.90	1.5	repellor	repellor
0.08	0.40	1.5	repellor	repellor
0.30	-0.90	1.5	attractor	repellor
0.10	0	1.5	saddle point	attractor

increasing initial rotation. In conclusion, the system's dynamics depends to a large extent on the initial conditions and, indeed, the system does show chaotic behavior that makes the system limited predictable. However, not all features seen in the experiments are reproduced by the model as was to be expected given the limited validity of the model, a number of significant simplifications and neglecting a number of processes as discussed in section 4.4.1.

#### 4.4.4 QUANTIFICATION OF THE PREDICTABILITY BY THE LARGEST LYAPUNOV EXPONENT

For dynamical non-linear systems that are sensitive to  $\mathbf{X}_{p,0}$ , the predictability of a system can be quantified by the largest Lyapunov Exponent (LLE)  $\lambda$ . This exponent characterizes the separation rate of infinitesimally close trajectories with a small difference  $\delta\mathbf{X}_{p,0}$  in initial conditions:

$$|\delta\mathbf{X}_p(t)| \approx e^{\lambda t} |\delta\mathbf{X}_{p,0}|. \quad (4.25)$$

If  $\lambda < 0$  the initial small difference converges in time to zero which implies a stable system. If  $\lambda > 0$  the difference increases in time which implies a 'chaotic' and consequently a non-predictable system. There are several algorithms available for determining LLE from time series in literature. A main demand when working with experimental data is the ability of the algorithm to be able to handle relatively short time series which is the case for the present study. Consequently, the algorithm proposed by Rosenstein *et al.* (1992) was applied. This algorithm works well with small, noisy data sets and was reportedly verified using generally accepted benchmarks (Rosenstein *et al.*, 1992). An important condition for the successful application of the Rosenstein algorithm is that the number of data points  $n$  available

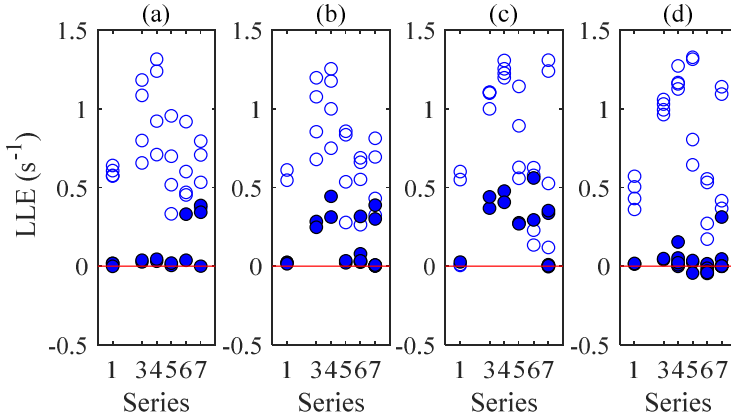


Figure 4.10: Calculated LLE's of the 2D/ 3D-PTV experimental data and model data sets of (a) sphere 86 (b) sphere 88 (c) sphere 101 and (d) sphere 102. The filled and open circles represent the experimental and model data respectively.

from the measurements and/or model is sufficiently large according to a requirement formulated by Eckmann & Ruelle (1992)  $n > 10^m$  in which  $m$  is the embedding dimension of the dynamic system (the attractor). In all experiments presented, this condition is met. When it comes to the mathematical model's predictability of the behavior of the system for the vortex driven particle motion, only situations having a negative LLE can be considered. Figure 4.10 shows the calculated LLE applying an embedding dimension  $m = 3$  for both the experimental and model results. The LLE's of series 8 are not analysed because of large scale oscillations. The experimental  $\mathbf{X}_{p,0}$  are not known in detail so the model LLE's are calculated for 4 combinations of  $\mathbf{X}_{p,0}$  that are assumed as being realistic:  $r_0 = 0.15$  m,  $\Omega_{p,0} = 0$  and  $0.2$  rad  $s^{-1}$  and  $U_{\theta,0} = 0.5V_\theta$  and  $0.99V_\theta$ . The initial tangential velocity  $U_{\theta,0}$  is used instead of  $U_{r,0}$  to provide a larger data set. The experimental and model LLE's show the same trend and are in general  $> 0$ . The differences between experiment and model LLE's are assumed as related to the 2D approach of the model. The inverse of the LLE (the Lyapunov time), that is  $1/\lambda$ , is a characteristic timescale indicating the predictability horizon of the particle motion. For the system under consideration this range is  $\sim 0.8$  to  $\sim 10$  s and when compared to the timescale of 2 s for hydrodynamic chaotic oscillations (Gaspard, 2005), the system can be quantified as limited predictable. To conclude, the free-surface vortex driven particle motion is quantified as chaotic with a limited predictability.

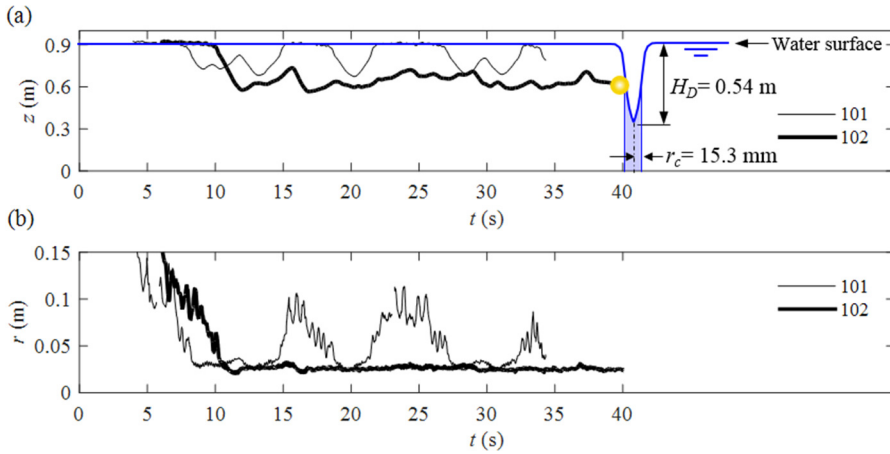


Figure 4.11: (a) 3D-PTV measured axial motion along the vortex center axis for exp. 101-7 and exp. 102-7. Sphere 102 ends at an equilibrium height of  $z \approx 0.60$  m where sphere 101 shows an up- and down motion. (b) Measured radius of the sphere's orbit around the center axis. For sphere 102,  $dr/dt \approx 0$  at  $t > \sim 12$  s.

## 4.5 MOTION PARAMETER FOR CONTINUOUS DOWNWARD MOTION ALONG THE AIR CORE

As the broader aim of this thesis is to study the applicability of the free-surface vortex for the downward transport of buoyant particles, a motion parameter  $\Phi$  is proposed to provide a first indication if continuous downward motion along the air core will occur (the stage 1 motion). The motion parameter is limited to spherical particles.

### 4.5.1 DEFINITION OF A CONTINUOUS DOWNWARD MOTION

A continuous downward particle motion is defined as the non-stop helical motion along the air core until the bottom of the air core is reached where the particle centralizes in the vortex core. To illustrate this definition, Figure 4.11 shows the measured motion of two spheres. Sphere 102 shows a downward motion from the water surface to an equilibrium height halfway the air core ending in a stable limit cycle at  $r \approx 0.025$  m. Sphere 101 shows an up and down motion without ending in an equilibrium position. According to the definition, both spheres don't show a continuous motion until the air core bottom. Furthermore, Figure 4.12 shows the experimental results of the spheres with respect to continuous or no continuous downward motion. The experiments show less continuous motion (indicated by a filled circle). The major part of the motion ended in an orbit around the air core at a specific height  $z$ . Only a combination of series 6 and spheres 88 and 102 showed a continuous particle motion.

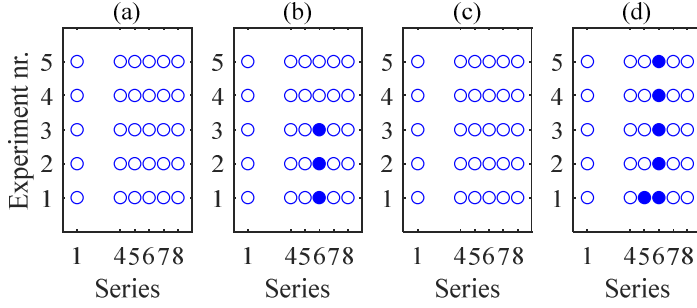


Figure 4.12: 3D-PT V results of the downward motion of the spheres, (a) sphere 86, (b) sphere 88, (c) sphere 101, (d) sphere 102. A continuous downward motion is indicated by a filled circle. The experiments are repeated 5 times at conditions as identical as feasible.

#### 4.5.2 MOTION PARAMETER

The dimensionless motion parameter  $\Phi$  represents the ratio between the inertial/added mass force and the lift force:

$$\Phi = \frac{|\mathbf{F}_{i,A}|}{(\mathbf{F}_{L,\omega} + \mathbf{F}_{L,\Omega_p})}. \quad (4.26)$$

To obtain a sustained downward motion the condition  $\Phi > 1$  has to be met. This implies that the sphere remains ‘pushed’ against the air-water interface until the bottom air core is reached. By application of the force equations (4.4), (4.11) and (4.18) while neglecting the radial fluid velocity,  $\Phi$  is expressed as:

$$\Phi = \frac{|\rho_f (1 + C_A) \chi (\mathbf{V} \cdot \nabla \mathbf{V})| \cdot \hat{\mathbf{e}}_r}{\rho_f \chi (\mathbf{V} - \mathbf{U}) (2\Omega_p + C_L \omega_z) \cdot \hat{\mathbf{e}}_r}. \quad (4.27)$$

By assuming the sphere’s center positioned at coordinates  $[x, 0]$  and assuming a circular motion, equation (4.27) is expressed in Cartesian coordinates as:

$$\Phi = \frac{\rho_f (1 + C_A) \chi \left( V_y \frac{\partial V_x}{\partial y} + V_x \frac{\partial V_x}{\partial x} \right)}{\rho_f \chi (V_y - U_y) (2\Omega_p + C_L \omega_z)}. \quad (4.28)$$

For  $[x, 0]$ ,  $V_x = 0$  and  $V_y \partial V_x / \partial y = V_y^2 / x$ . The value of  $U_y$  in the relative velocity term  $(V_y - U_y)$  is dynamic and given the chaotic character of the system under consideration has a limited predictability at best.  $U_y$  is expressed as  $\gamma V_x$  ( $\gamma$  is the relative velocity parameter:  $(V_y - U_y) = V_y(1 - \gamma)$ ):

$$\Phi = \frac{(1 + C_A)V_x^2}{xV_x(1 - \gamma)(2\Omega_p + 1.8\omega_z)}. \quad (4.29)$$

The vorticity  $\omega_z$  is a known function of  $x$ .  $\Omega_p$  is limited predictable and therefore replaced by  $\Omega_{p,st}$  which is the known maximum value at position  $x$  and thus a conservative approach.  $C_L = 1.8$  being the maximum value for the experimental range. For a cylindrical coordinate system and applying Burgers' (1948) model of  $V_\theta$ , the motion parameter  $\Phi$  is:

$$\Phi = \frac{0.76L^{-2}(1 - \gamma)^{-1} \left\{ 1 - \exp \left[ - \left( \frac{r}{r_c} \right)^2 \right] \right\}}{\left( \frac{0.0054(\Gamma_\infty L)^{0.64}}{(1 - \gamma)^{1.64} r^{2.64} \nu^{0.64}} \left\{ 1 - \exp \left[ - \left( \frac{r}{r_c} \right)^2 \right] \right\}^{1.64} + \frac{0.57}{r_c^2} \exp \left[ - \left( \frac{r}{r_c} \right)^2 \right] \right)}. \quad (4.30)$$

Given the vortex and particle characteristics  $\Phi$  provides a first indication of the minimum required value of  $\gamma$  at each radial position for a continuous downward motion. An example is provided for the spheres 103 and 86 at series 3 to 7 based on experimental data. Figure 4.13 shows the computed motion parameter  $\Phi$  in a series of values for  $\gamma = 0.5, 0.8, 0.85$  and  $0.9$ . The results show that a continuous downward motion occurs for  $\gamma > 0.8$ . The validity of this motion parameter  $\Phi$  is evaluated by analysing experimental results and the corresponding parameter  $\gamma_{exp}$ . The latter is determined by  $\gamma_{exp}(r) = V_\theta(r)/U_\theta(r)$  with  $U_\theta$  being a measured value. Figure 4.14 shows the results of  $\gamma_{exp}$ . The results show some noise due to noise in the measured values of  $U_\theta$ . The experiments show that downward motion is terminated at approximately  $0.4 < \gamma_{exp} < 0.8$ . However, a major part of the terminated motion at  $\gamma_{exp} < 0.6$  occurs at unstable situations. For example, this is illustrated in the left graph of Figure 4.5 where the sphere 'touches' the air core bottom ( $r = 0$  m) but ends in a stable limit cycle at  $r = 0.05$  m with  $\gamma_{exp} \approx 0.8$ . In conclusion, the proposed motion parameter  $\Phi$  provides a first indication if continuous motion will occur. The validity however, strongly depends on the correct assumption of the relative velocity parameter  $\gamma$  which needs further research.

## 4.6 CONCLUSIONS

Extensive experiments are conducted in a  $\varnothing 600$  mm vortex tank to study the free-surface vortex driven helical motion of buoyant particles along the vortex air core. The experimental particles were spherical with a characteristic length  $L$  of 0.025 and 0.038 m. The particle Reynolds number was  $\sim 10^2 \leq Re_p \leq \sim 10^4$ . For the given

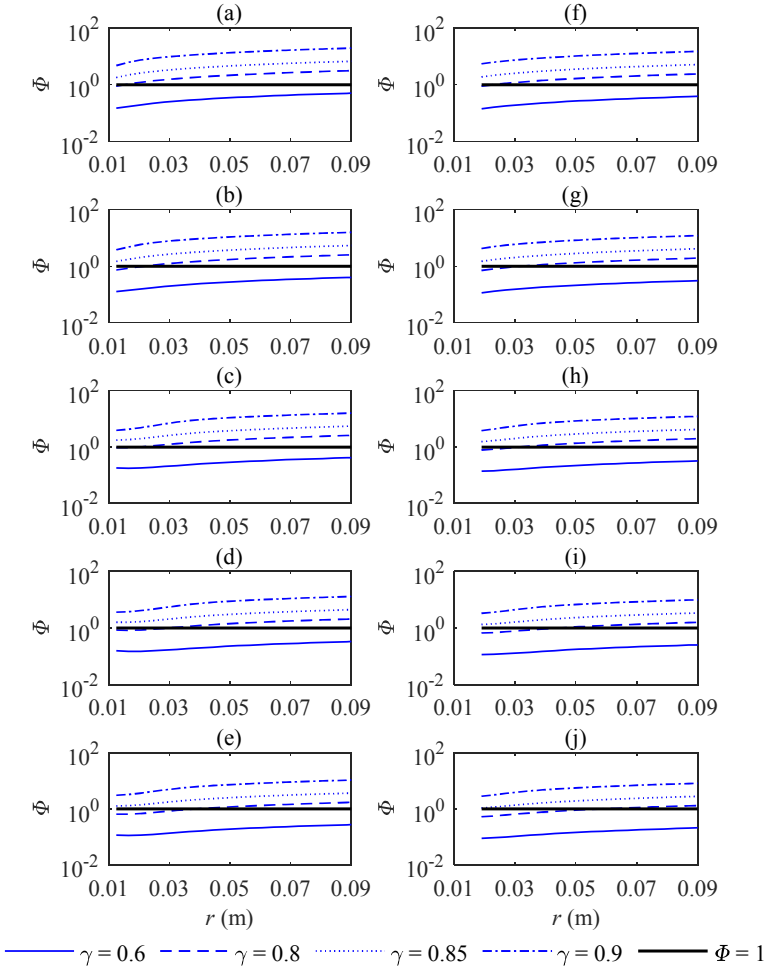


Figure 4.13: Motion parameter  $\Phi$  for series 3 to 7. (a)-(e)  $\Phi$  for  $\varnothing 25$  mm sphere. (f)-(j)  $\Phi$  for  $\varnothing 38$  mm sphere. A continuous downward motion is provided at approximately  $\gamma > 0.8$ .

experimental parameter ranges, the experiments revealed that the particle motion has a very sensitive dependence on the particle initial conditions i.e. the initial velocity and rotation by showing chaotic behavior. This behavior is not uncommon for non-linear dynamic systems i.e. the system under consideration. This behavior is also shown by a simplified mathematical model of the free-surface vortex driven particle motion. The chaotic behavior of the experiments and the model is confirmed by the quantification of the largest Lyapunov Exponent. Consequently, the free-surface vortex driven particle motion has limited predictability and allows to be analysed in a qualitative manner only by use of phase portraits. A motion parameter is proposed

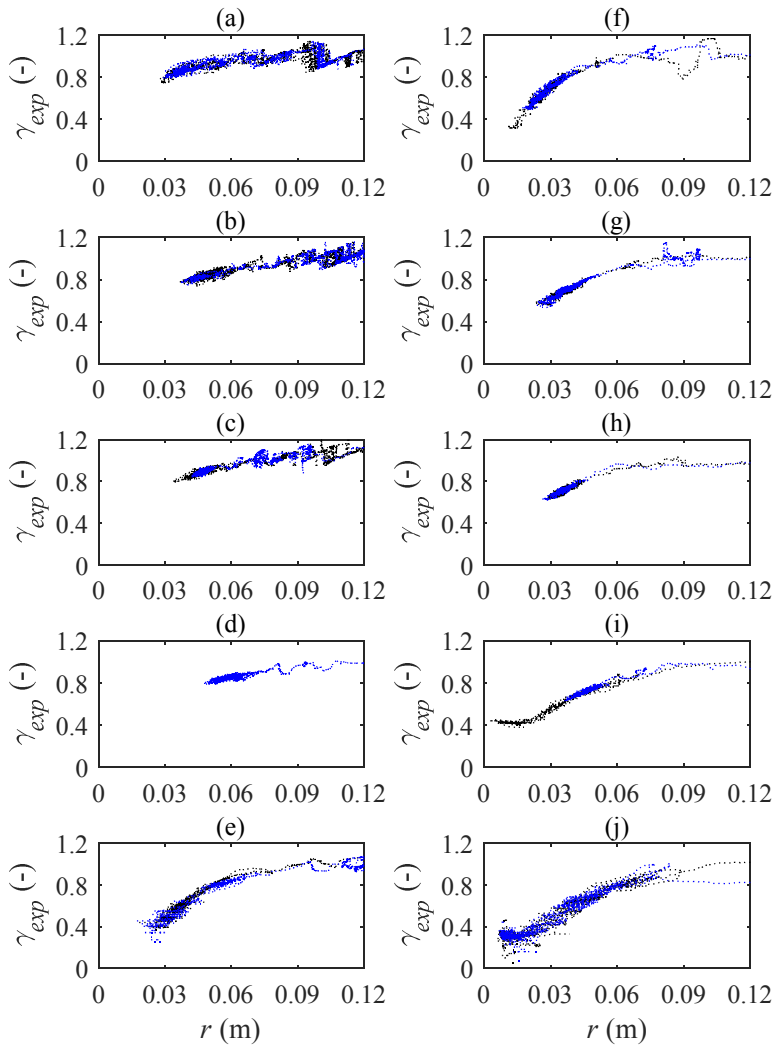


Figure 4.14: Experimental relative velocity parameter  $\gamma_{exp}$  determined from two sets of 2D-PTV measurements. (a)-(e)  $\gamma_{exp}$  for sphere 103 ( $\text{Ø}25$  mm). (f)-(j)  $\gamma_{exp}$  for sphere 86 ( $\text{Ø}38$  mm).

that provides a first indication if a continuous downward particle motion occurs.

The experiments were also conducted for cubical and ellipsoidal shaped experimental particles with similar  $L$  and  $\rho_p$ . These shapes showed to be less sensitive to the particle's initial conditions and displayed less chaotic behavior in the motion through the vortex flow field. The non-point symmetric shapes yield the modelling of the inertial and lift forces complex. Therefore, these experimental results are not utilized in this thesis and are subject to further study.



# 5

## **VORTEX DRIVEN PARTICLE MOTION: MOTION THROUGH THE VORTEX CORE**

The main content of this chapter is based on Duinmeijer, S.P.A. & Clemens, F.H.L.R (2019c). (subm.). *Experimental study on free-surface vortex driven particle motion at high Reynolds numbers: the motion through the vortex core*. Submitted to *Journal of Hydraulic Research*.

## 5.1 INTRODUCTION

The stage 2 motion (see section 1.6 and Figure 1.7) of buoyant particles is assumed to be determined by the fluid axial drag force and the buoyancy force. The particle's axial motion parallel to the axis of a solid-body rotating fluid introduces a complex phenomenon which is as first described by Proudman (1916) and Taylor (1917). They found that a moving sphere was accompanied by a fluid column that circumscribed the sphere. This column influences the drag on the moving body. For inviscid flow, Stewartson (1952) presented a theoretical study on the influence of this so-called Taylor column on the drag force and proposed an expression for this force for the inviscid limit. For a low viscous fluid and an axial geometry of finite length, Moore and Saffman (1968) studied the drag force on a rising body with a Taylor column up- and downstream of the body. For  $\sim 5 < Re_{p,z} < \sim 10^3$  with  $Re_{p,z}$  the axial particle Reynolds number  $|V_z - U_z| L/\nu$  with  $V_z$  and  $U_z$  the axial fluid and particle velocity respectively, Maxworthy (1970) reports an experimental study on the drag force on  $\varnothing 12.7$  and  $\varnothing 19$  mm rising spheres along the center axis of a  $\varnothing 305$  mm rotating tank of water. Tanzosh and Stone (1994) studied the particle motion parallel to the axis of rotation in a fluid in solid body rotation by application of an integral equation approach for  $Re_{p,z} \ll 1$ . Bush *et al.* (1994) performed a comprehensive survey of particle motion in solid-body rotating fluids for motions parallel and perpendicular to the axis of rotation. Bush *et al.* (1995) performed an experimental and theoretical study on the axial motion of a deformable drop in a solid-body rotating fluid.

In this thesis and compared to the mentioned literature, the axial motion is not driven by a buoyancy force but driven by a non-uniform axial flow. Furthermore, the vortex flow field is not fully in solid-body rotating. The steady solid-body rotating flow is limited to a distance of  $\sim r_c$  from the vortex center axis. Consequently, the results from literature are not directly applicable to study the vortex driven motion through the core. To obtain knowledge on this motion experiments are conducted on the axial motion of particles through the core. By applying this data, a stage 2 motion condition is proposed to provide a first indication if axial motion through the core occurs as function of the particle and vortex characteristics. This chapter addresses the experimental results and the development and validation of this condition.

The structure of this chapter is as follows: first section 5.2 and 5.3 address the experimental program, procedure and results of the measured axial motion of the particles through the vortex core. Section 5.4 addresses the quantification of the axial velocity profile throughout the vortex core by using the SPIV results presented in Chapter 3. These profiles are applied for the quantification of the axial drag force acting of the particles. The stage 2 motion condition is addressed and discussed in section 5.5 and 5.6. Finally, the conclusions are presented in section 5.7.

## 5.2 EXPERIMENTAL PROCEDURE AND PROGRAMME

### 5.2.1 PROCEDURE

The motion of the particles in stage 2 is measured by 3D-PTV. Prior to starting the 3D-PTV measurements, care was taken to obtain a stationary free-surface vortex which takes around 15 minutes. The stationary situation was validated by comparing the air core depth  $H_D$  with the  $H_D$  for the known stationary situation. Then the room lights were shut off, the UV-lights and the six cameras switched on and the particle was released on the water surface by using the remote-controlled device, see Figure 2.2(d). The experiment was classified as ‘terminated’ when either one of the three following conditions was applied: (1) the particle was transported out of the control volume through the outlet within  $t < \sim 300$  s after the particles’ release at the water surface (2) at  $t > \sim 300$  s the particle remained either stationary at the air core bottom or at a certain level above the tanks’ bottom in the vortex core and (3) at  $t > \sim 300$  s after the release the particle was still present in the control volume. In this case the particle showed a repeating motion like entering the air core, ejecting out the air core and entering the air core again, the sequence was recorded a few times to check the consistency of this behavior.

As a large part of the experiments showed ejection of the particles in the stage 1 motion less experimental data was obtained of the stage 2 motion. To obtain more experimental data on this axial motion through the vortex core and particularly for the validation of the stage 2 motion condition, a method was used where particles were forced to start at the bottom of the air core. This is done by dropping the particle from above the surface into the air core to have them situated at the air core bottom which is defined as the start position for the downward motion. This method is hereafter referred to as ‘the dropping method’. As numerous particles broke down the air core resulting in an air volume under the particle, see also Figure 1.8(b), the air was removed by disturbing the axial flow in the vortex core, so the air rises to the surface.

#### DEFINITION OF AXIAL MOTION THROUGH THE VORTEX CORE

Experiments meeting condition 1 and  $t_a \leq T$  are labelled as ‘Motion’ and experiments meeting condition 3 or condition 1 and  $t_a > T$  are labelled as ‘No motion’.  $t_a$  is the measured time needed for a particle to travel the distance from the air core bottom to the outlet:  $H - H_D$ .  $T$  is a characteristic time parameter and determined by the hydraulic conditions:  $T = (H - H_D) / U_{z,\min}$  with  $U_{z,\min}$  a defined minimum required particle velocity. By definition,  $U_{z,\min}$  is set equal to  $V_{z,\min} = Q_v / (4\pi r_c^2)$  that is the minimum averaged flow velocity through the vortex core.  $Q_v = \gamma Q$  is the flow rate through the vortex core. By applying  $\gamma = 0.1$  (see section 3.5) the required minimum particle velocity  $U_{z,\min} = 0.01 \text{ m s}^{-1}$  and thus  $T = 100(H - H_D)$  or by applying equation (3.24):

$$T = 100 \left[ H - \frac{\ln 2}{4\pi^2 g} \left( \frac{\Gamma_\infty}{r_c} \right)^2 \right]. \quad (5.1)$$

### 5.2.2 EXPERIMENTAL PROGRAMME

The 3D-PTV experimental programme for the stage 2 motion is similar to the stage 1 programme, see section 4.3.2 and included the 8 series of vortex characteristics and the 15 different particles. Each experiment is repeated 5 times (sub-experiments 1 to 5) to check the reproducibility of the experiment. The dropping method experimental programme for the spheres and cubes is listed in Table D.1 in Appendix D. The experimental programme for the ellipsoids is listed in Table D.2. In combination with the results of the 3D-PTV experiments, a data set of 65 experiments was obtained for the validation of the motion condition for the spheres and cubes and a data set of 31 experiments was obtained for the validation of the ellipsoids.

The experimental conditions are presented by the particle number followed by the series number, for example: ‘exp. 86-4’.

## 5.3 EXPERIMENTAL RESULTS

This section shows the results of the 3D-PTV measured axial motion of the particles through the vortex core as function of time and including a short qualitative analysis of the observed motion to stipulate some characteristic behavior of that type of shape. The results of the total experimental programme are listed in Appendix D. Indeed, the particles start at the free-surface at height  $z \approx 0.9$  m. The motions are shown for the spheres, cubes and ellipsoids for various series and sub-experiments. For various experiments, the duration of the measured motion is relatively short, say  $t < 20$  s. In these experiments the particle showed an outward directed motion because of the chaotic behavior. In this case, the measurements were finished at after a short period.

### 5.3.1 MEASURED AXIAL MOTION OF THE SPHERES

For series 1, Figure 5.1 shows the measured axial motion of the spheres 86, 88, 101 and 102. For all spheres there is approximately no axial motion visible, hence the spheres stay at the surface. Figure 5.2 shows the results for series 7. Here, the results show an up- and down motion along the air core. This motion is due to an unbalance between the inertial and lift forces in the horizontal plane as quantified in section 4.5. Consequently, there is no axial motion through the vortex core (stage 2 motion).

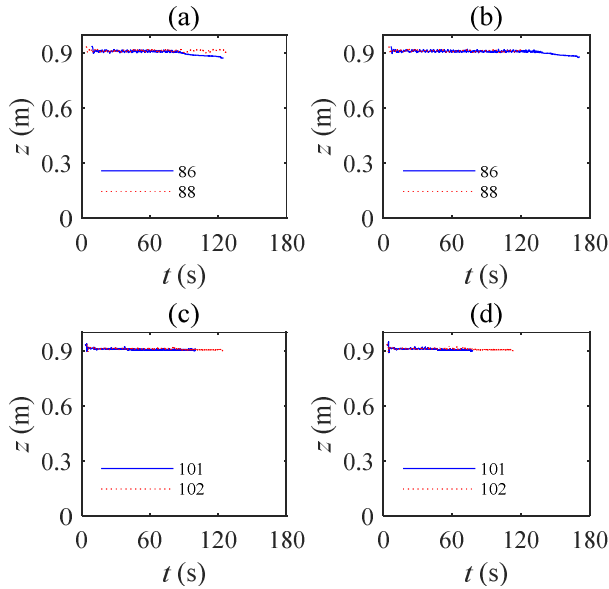


Figure 5.1: 3D-PTV measured axial motion of the spheres 86, 88, 101 and 102. (a)-(b) results of exp. 86-1 and exp. 88-1 for sub-exp. 1 to 2. (c)-(d) Results of exp. 101-1 and exp. 102-1 for sub-exp. 1 to 2.

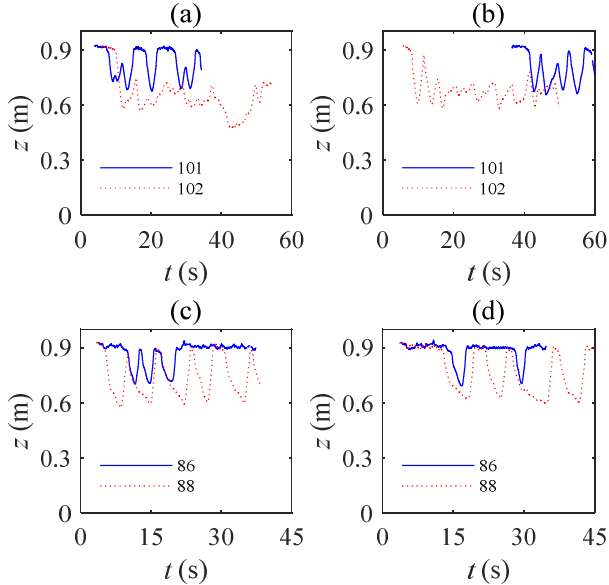


Figure 5.2: 3D-PTV measured axial motion of the spheres 86, 88, 101 and 102. (a)-(b) Results of exp. 101-7 and exp. 102-7 for sub-exp. 1 to 2. (c)-(d) Results of exp. 86-7 and exp. 88-7 for sub-exp. 3 to 4. In these experiments all sphere's show an up- and down motion along the air core and due to an unbalance between the inertial and lift forces.

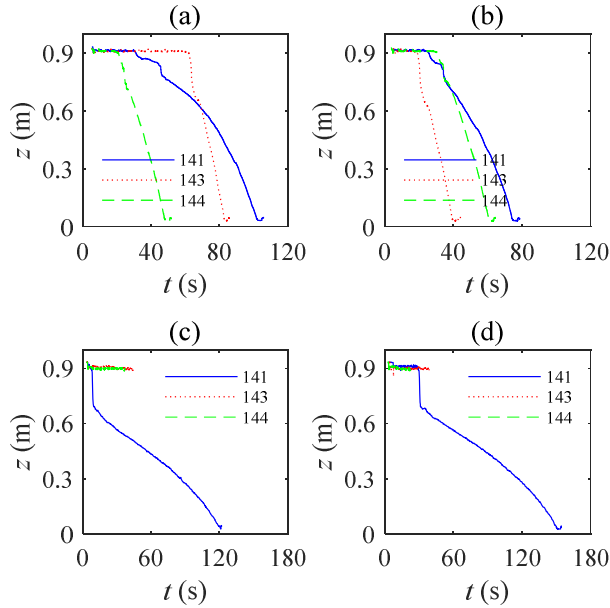


Figure 5.3: 3D-PTV measured axial motion of the cubes 141, 143 and 144. (a)-(b) Results of exp. 141-2, exp. 143-2 and exp. 144-2 for sub-exp. 1 to 2. (c)-(d) Results of exp. 141-6, exp. 143-6 and exp. 144-6 for sub-exp. 3 to 4. The cubes axial velocity at series 2 is higher than at series 6 at equal mean outlet velocity. This is assumed as due to a higher mean axial flow velocity in the vortex core.

### 5.3.2 MEASURED AXIAL MOTION OF THE CUBES

Figure 5.3 show the measured axial motion of the cubes 141, 143 and 144 ( $L = 30.6$  mm) at series 2 and 6. The cubes axial velocity at series 2 is higher than at series 6 at equal mean outlet velocity  $U_o$ . This is due to a higher mean axial flow velocity in the vortex core that generates a larger axial ‘drag’ force on the cube and consequently a higher axial velocity of the cube.

### 5.3.3 MEASURED AXIAL MOTION OF THE ELLIPSOIDS

For series 5, Figure 5.4 shows the measured axial motion of ellipsoids 111 and 113 ( $L = 76$  mm). In general, all ellipsoids succeed the stage 1 motion (the downward helical motion along the air core). Consequently, the ellipsoids appear to be less sensitive to lift forces that terminate the stage 1 motion. On the other hand, however, ellipsoid 111 clearly shows a downward axial motion while ellipsoid 113 remains at the air core bottom. This behavior appears to be determined by the higher specific density and thus lower buoyancy force of ellipsoid 111.

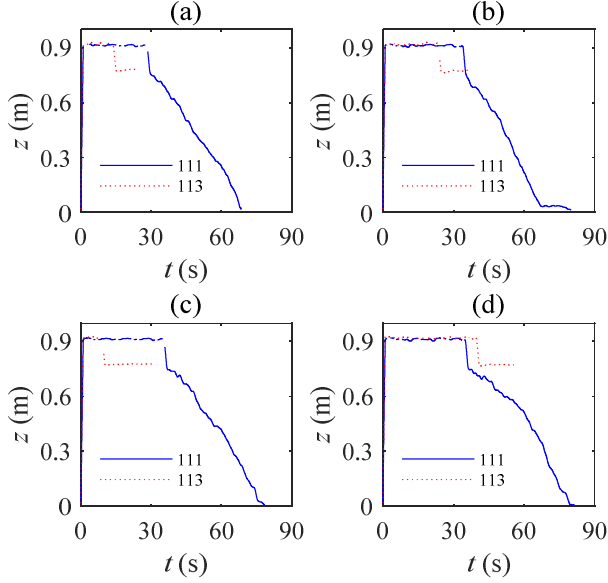


Figure 5.4: 3D-PTV measured axial motion of the ellipsoids 111 and 113. (a)-(d) Results of exp. 111-5 and exp. 113-5 for sub-exp. 1 to 4. Only ellipsoid 111 shows axial motion which is clearly related to the higher density of 111 and thus a smaller buoyancy force.

## 5.4 THE AXIAL VELOCITY PROFILE IN THE VORTEX CORE

This section addresses the quantification of the radially uniform  $V_z$  in the vortex core. This velocity is used for quantification of the axial drag force acting on the particles. First, section 5.4.1 addresses the theoretical approximation of the measured  $V_z$  profile and subsequently section 5.4.2 addresses the transformation of the approximated profile of  $V_z(r)$  to a radially uniform velocity.

### 5.4.1 THEORETICAL APPROXIMATION OF THE MEASURED PROFILE

The SPIV measured profile of  $V_z$  in the vortex core is approximated with a Gaussian function using the measured values of  $V_{z,\max,av}$  and  $r_{\max}$ :

$$V_z(r) = V_{z,\max,av} \exp \left[ - \left( \frac{r - r_{\max}}{\alpha r_{\max}} \right)^2 \right]. \quad (5.2)$$

$V_{z,\max,av}$  is the averaged value of the measured  $V_{z,\max}$  at each height in the vortex and  $r_{\max}$  is the radial position of the maximum  $V_z$ .  $\alpha$  is the width factor of the Gaussian

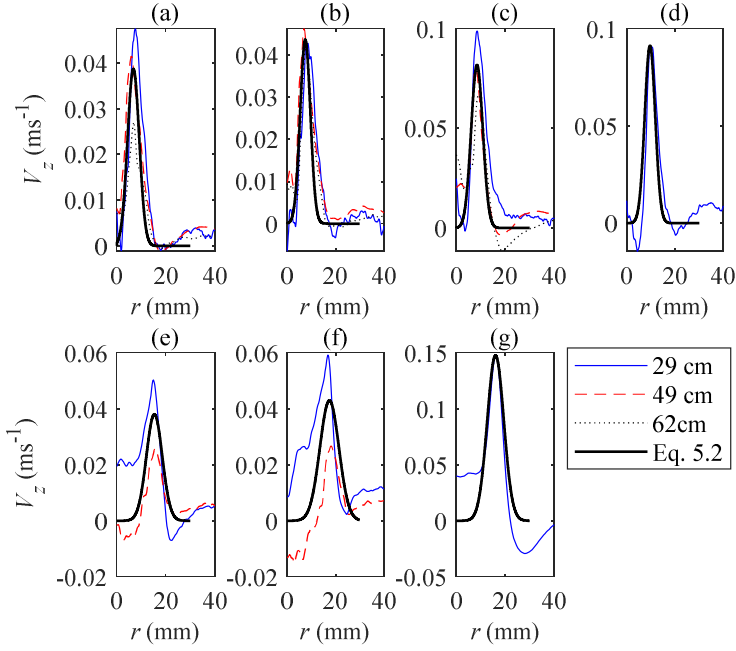


Figure 5.5: (a)-(g) Measured profiles of  $V_z$  and the approximated profile of  $V_z(r)$  for series 1 to 7 with  $\alpha = 0.5, 0.4, 0.4, 0.32, 0.3, 0.32$  and  $0.3$ .  $\alpha$  is the Gaussian width factor for the best fit with the SPIV measured profiles.

velocity profile to obtain a best fit with the measured profile and determined for each series. Figure 5.5 shows the measured and approximated  $V_z$  profiles.

#### 5.4.2 RADIALLY UNIFORM AXIAL VELOCITY

The radially uniform axial velocity is defined as  $\overline{V_z}$ . This velocity is obtained by determining the average value of  $V_z(r)$  over a radial domain equal to half length of the particle that is centralized in de vortex core:  $r = 0.5L$ , see Figure 5.6. The radial uniform  $\overline{V_z}$  to quantify the axial drag force acting on a particle with dimension  $L$  is then defined by:

$$\overline{V_z} = \frac{1}{A} \iint_A V_z(r) dA_N = \frac{8}{L^2} \int_0^{0.5L} V_z(r) r dr. \quad (5.3)$$

By applying equation (5.2), the plane averaged radial uniform velocity  $\overline{V_z}$  is then approximated by:

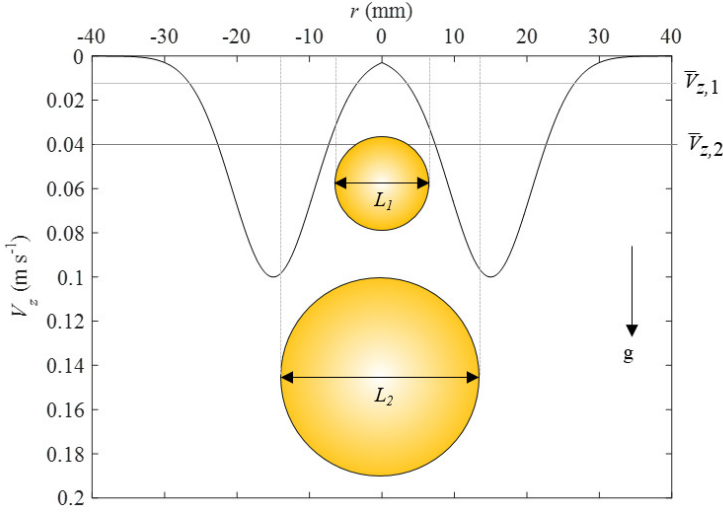


Figure 5.6: Schematic view of two spheres with diameter  $L_1$  and  $L_2$  that are centralized in the vortex core. The figure also shows the axial velocity profile  $V_z(r)$  that follows from equation (5.2) which approximates the measured profiles. For both spheres, the figure illustrates the radially uniform axial velocity  $\overline{V_{z,1}}$  and  $\overline{V_{z,2}}$  over the radial domain  $0 < r < 0.5L$ .

$$\overline{V_z} = \frac{8V_{z,\max,av}}{L^2} \int_0^{0.5L} \exp\left[-\left(\frac{r-r_{\max}}{\alpha r_{\max}}\right)^2\right] r dr. \quad (5.4)$$

The values of  $\overline{V_z}$  are approximated inclusive the 95% confidence interval ( $\pm 2\sigma$ ) with  $\sigma = 0.002V_{\theta,\max}$ .

## 5.5 DETERMINATION OF THE STAGE 2 MOTION CONDITION

This section addresses the development of a motion condition that provides a first indication if axial motion through vortex core occurs as function of the particle and vortex characteristics. Two methods are applied to derive the condition: (1) by applying the independent experimental parameters and (2) by applying the Taylor-column drag force.

### 5.5.1 MOTION CONDITION BASED ON THE INDEPENDENT EXPERIMENTAL PARAMETERS

In the experimental program the independent experimental parameters are  $H$ ,  $Q$ ,  $D$ ,  $L$ ,  $C_D$ ,  $\rho_p$  and  $\rho_f$ . In here, the standard drag coefficient  $C_D$  represents the effects of the fluid viscosity and the particle shape (sphere, cube and ellipsoid) as function of the

experimental  $Re_z$  range. For the sphere reliable values of  $C_D$  are known over a wide range of Reynolds numbers but no for cubes and ellipsoids. To approximate these  $C_D$  values Holzer and Sommerfeld (2008) proposed a correlation formula for non-spherical particles:

$$C_D = \frac{8}{Re} \frac{1}{\sqrt{\Phi_\perp}} + \frac{16}{Re} \frac{1}{\sqrt{\Phi}} + \frac{3}{\sqrt{Re}} \frac{1}{\Phi^{3/4}} + 0.42 \cdot 10^{0.4(-\log \Phi)^2} \frac{1}{\Phi_\perp}. \quad (5.5)$$

The sphericity  $\Phi$  is the ratio between  $A_S$  of the volume-equivalent sphere and the non-spherical particle. The cross-wise sphericity  $\Phi_\perp$  is the ratio between  $A_N$  of the sphere and the non-spherical particle. As both the cubes and ellipsoids are not point symmetric, the  $C_D$  depends on the particle's orientation at the start of the vortex' core with respect to the flow direction. At the onset and during the axial motion through the vortex core, this orientation is dynamic as shown in the 3D-PTV recordings of Figure 5.7. The cubes show an angled stationary orientation with  $A_N$  a hexahedron with a rib length of  $0.5(2L)^{0.5}$  and so  $A_N = 1.3L^2$ . For the ellipsoids the initial orientation and thus the  $A_N$  is taken as the averaged value of the three orientations, see section 5.5.2. The (averaged) drag coefficient  $C_D$  of the different shapes is:

$$\begin{aligned} \text{Sphere: } C_D &= \frac{24}{Re} + \frac{3}{\sqrt{Re}} + 0.42 \\ \text{Angled cube: } C_D &= \frac{26.09}{Re} + \frac{3.52}{\sqrt{Re}} + 0.80 \\ \text{Ellipsoid: } \bar{C}_D &= \frac{26.32}{Re} + \frac{3.58}{\sqrt{Re}} + 0.88. \end{aligned} \quad (5.6)$$

The experimental parameters can be represented by two dimensionless parameters. The first dimensionless parameter is defined as  $N_B$  and represents the effect of buoyancy on the axial particle motion:

$$N_B = \frac{\rho_f - \rho_p}{\rho_f}. \quad (5.7)$$

The second dimensionless parameter  $N_D$  can be read as the axial drag force acting on the particle and generated by the axial flow velocity  $V_z$ :

$$N_D = \frac{Q^2 C_D}{D^2 H L^2 g}. \quad (5.8)$$

The term  $Q^2/(D^2 H)$  shows similarity to the axial velocity gradient  $d\overline{V_{z,i}}/dz$  using the average axial outlet velocity  $\overline{V_{z,i}}$ . As a first assumption the value of  $C_D$  is taken as an approximated average over the experimental range of  $Re_{p,z}$  and computed with

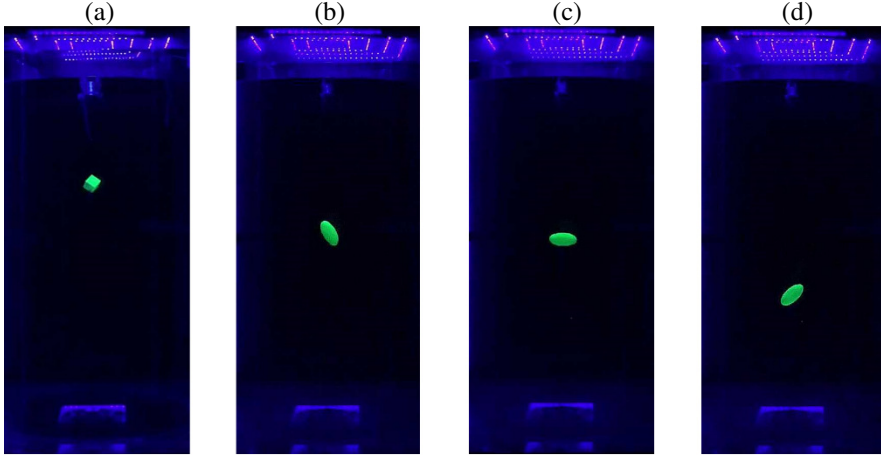


Figure 5.7: (a) Stationary orientation of the cube in the vortex core in exp. 154-5. The cube is orientated as an ‘angled’ cube. (b)-(d) Dynamic orientation of the ellipsoid in the vortex core in exp. 114-2.

equation (5.6). For the spheres, cubes and ellipsoids the  $C_D = 0.7, 1.1$  and  $1.2$  respectively.

Figure 5.8 shows the results of the 3D-PTV measured motion as function of the dimensionless parameters  $N_B$  and  $N_D$ . In order to study the stage 2 motion condition, the results are presented by the labels ‘Motion’ and ‘No motion’ as defined in Section 5.2.1. The presented results show no distinct relation between particle motion and the particle and vortex characteristics. Indeed, various experiments show same values of  $N_B$  and  $N_D$  but with opposites results (‘Motion’ and ‘No motion’). Consequently, it seems not possible to describe a motion condition as function of the experimental parameters  $H, Q, D, L, C_D, \rho_p$  and  $\rho_f$ .

### 5.5.2 MOTION CONDITION BASED ON TAYLOR-COLUMN DRAG FORCE

By applying the general equation of particle motion (equation (4.3)) and by substituting the expressions of the drag force and the lift forces by vorticity and particle rotation for spherical particles, the equation of motion for spherical particles is expressed by:

$$\begin{aligned} (\rho_p + C_A \rho_f) \chi \frac{DU}{Dt} = \rho_f (1 + C_A) \chi \frac{DV}{Dt} + 0.5 \rho_f C_D A_N (\mathbf{V} - \mathbf{U})(\|\mathbf{V} - \mathbf{U}\|) \\ + \rho_f \chi C_L (\mathbf{V} - \mathbf{U}) \times \boldsymbol{\omega} + 2 \rho_f \chi (\mathbf{V} - \mathbf{U}) \boldsymbol{\Omega}_p + \chi (\rho_f - \rho_p) \mathbf{g}. \end{aligned} \quad (5.9)$$

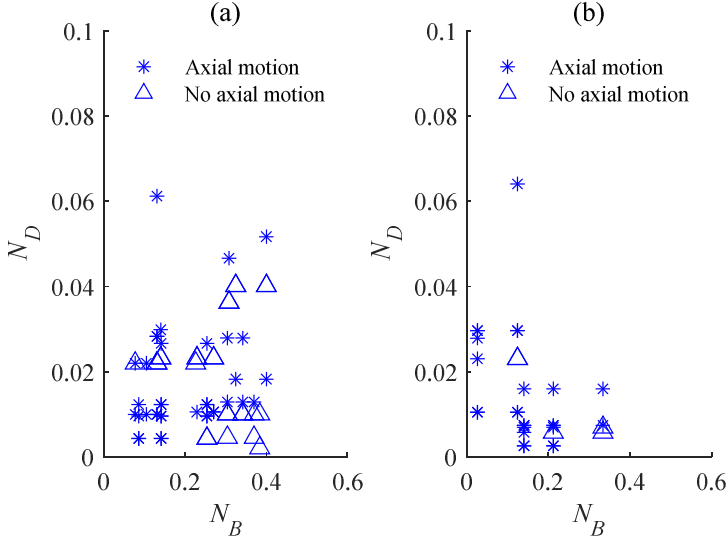


Figure 5.8: Experimental results of the measured motion of the particles as function of the dimensionless parameters  $N_B$  and  $N_D$ . (a) Results of the spheres and cubes. (b) Results of the ellipsoid.

For the free-surface vortex it is assumed that there is only vorticity  $\omega_z$  in the  $z$ -direction as defined in Chapter 3 and thus only a vorticity and particle rotation lift force in the horizontal plane. In vertical or axial direction and cylindrical coordinates, the equation of motion for spherical and non-spherical particles is then reduced to:

$$\begin{aligned}
 (\rho_p + C_A \rho_f) \chi \left( \frac{\partial U_z}{\partial t} + U_z \frac{\partial U_z}{\partial z} + U_r \frac{\partial U_z}{\partial r} + \frac{U_\theta}{r} \frac{\partial U_z}{\partial \theta} \right) = \\
 \rho_f (1 + C_A) \chi \left( \frac{\partial V_z}{\partial t} + V_z \frac{\partial V_z}{\partial z} + V_r \frac{\partial V_z}{\partial r} + \frac{U_\theta}{r} \frac{\partial V_z}{\partial \theta} \right) + \\
 0.5 \rho_f C_D A_N (V_z - U_z) (|V_z - U_z|) + \chi (\rho_f - \rho_p) g.
 \end{aligned} \tag{5.10}$$

The axial motion is characterized by the following conditions: (1) the particle is centralized in the vortex core without radial motion ( $U_r = 0$ ) and (2) the axial flow is axi-symmetric ( $\partial/\partial\theta = 0$ ), stationary ( $\partial/\partial t = 0$ ) and defined as radial uniform ( $\partial/\partial r = 0$ ). The equation of axial particle motion is then simplified to:

$$\begin{aligned}
 (\rho_p + C_A \rho_f) \chi \left( \frac{\partial U_z}{\partial t} + U_z \frac{\partial U_z}{\partial z} \right) = \rho_f (1 + C_A) \chi \left( V_z \frac{\partial V_z}{\partial z} \right) + \\
 0.5 \rho_f C_D A_N (V_z - U_z) (|V_z - U_z|) + \chi (\rho_f - \rho_p) g.
 \end{aligned} \tag{5.11}$$

The derivation of the motion condition focusses on the onset of particle motion and not on the particle motion itself. So, the left term in equation (5.11) must be  $> 0$ . Furthermore, at the onset of motion the term  $(1 + C_A) V_z \partial V_z / \partial z$  is assumed as negligible to the buoyance and drag force term and thus neglected. The equation of motion then reduces to:

$$-0.5\rho_f C_D A_N (V_z - U_z) (|V_z - U_z|) = \chi (\rho_f - \rho_p) g. \quad (5.12)$$

The axial drag force  $F_{D,z}$  on a particle is calculated by using the uniform flow approach:

$$F_D = 0.5\rho_f C_D A_N (|V_z - U_z|) (V_z - U_z). \quad (5.13)$$

In order to initiate a motion through the vortex core and by using the dimensionless buoyancy parameter  $N_B = (\rho_f - \rho_p) / \rho_f$  and applying the radially uniform axial velocity  $\bar{V}_z$  as discussed in section 5.4.2, the following condition must be met:

$$\frac{0.5C_D A_N (\bar{V}_z - U_z)^2}{\chi g} = \frac{\rho_f - \rho_p}{\rho_f}. \quad (5.14)$$

As the rotation-axis of the spinning particles is observed to be parallel with  $V_z$ , the spinning motion is assumed to have no effect on the axial drag force  $F_{D,z}$ .

#### TAYLOR DRAG COEFFICIENT FOR PARTICLE MOTION ALONG AXIS OF SOLID-BODY ROTATING FLUID

As mentioned in the introduction, a particle moving along the axis of a solid-body rotating fluid can be accompanied by a Taylor-column circumscribing the particle. This column has a significant effect on the drag force. The criterium for Taylor column formation is expressed by the Rossby number  $Ro = V_z / (\Omega 0.5L) < \sim 0.3$  with  $0.5L$  the radius of the sphere (Bush *et al.*, 1994). For all experiments in the present study,  $Ro < \sim 0.03$  and the Taylor-column is most likely to be present. Maxworthy (1970) experimentally studied the drag force on a rising sphere in a rotating flow and found that for large values of the Taylor number ( $T_a > \sim 10^2$ ) representing the relative magnitude of the Coriolis force to viscous force:

$$T_a = \frac{\Omega (0.5L)^2}{\nu} \quad (5.15)$$

and for the parameter  $N > 200$  that represents the relative magnitude of Coriolis force to inertia force:

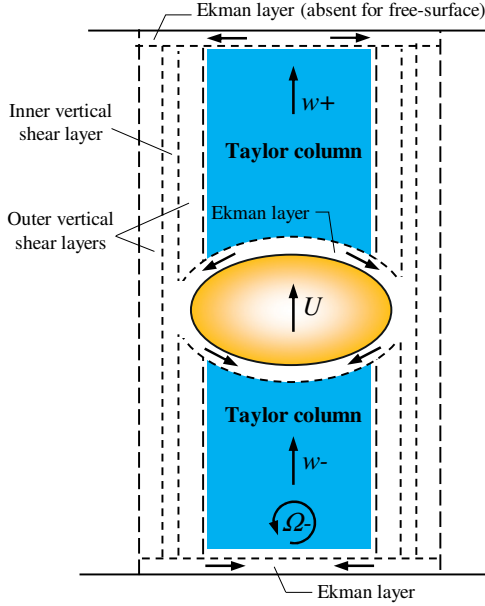


Figure 5.9: Rising body with velocity  $U$  pushing fluid into the Ekman layer that is present on the boundary of the geometry. This mechanism increases the fluid drag on the body with  $\sim 50\%$  (Moore & Saffman, 1968).

$$N = \frac{2\Omega(0.5L)^2}{U_z}. \quad (5.16)$$

The  $C_D$  for a sphere is independent of  $Re_z$  and depends on  $N$  only. In this study, the expression  $(0.5L)$  is used to indicate the use of the sphere radius. Based on experiments at  $T_a > \sim 200$ , that can be assumed as a geostrophic balanced fluid, Maxworthy (1970) found the following expression for the drag coefficient  $C_D$ :

$$C_D = (2.60 \pm 0.05) \left( \frac{2\Omega(0.5L)}{U_z} \right)^{1.00 \pm 0.01}. \quad (5.17)$$

The results of Maxworthy (1970) are in line with the theoretical results for inviscid conditions as presented by Stewartson (1952) and Moore & Saffman (1969) where  $C_D = 1.51N$ . The Taylor drag on a body is affected by the bounded geometry of the experimental set-up. When the set-up is axially bounded instead of a free-surface, the fluid in the Taylor column is pushed into an Ekman layer presented on this boundary and increases the drag with  $\sim 50\%$ , see Figure 5.9 (Moore & Saffman, 1968). In this study, the suction outlet at the bottom center is assumed to act as an unbounded condition, so bounding effects are neglected.

In the free-surface vortex, the rotation of the vortex core is assumed to be a solid-body rotation (this is not entirely valid as some radial diffusion of vorticity will occur). As the maximal tangential velocity  $V_\theta$  occurs near the vortex core radius  $r_c$ , the (maximum) angular velocity  $\Omega$  is:

$$\Omega(r_c) \approx \frac{V_\theta(r_c)}{r_c}. \quad (5.18)$$

By using the validated Burger's vortex model for  $V_\theta$  (equation (3.19)),  $\Omega$  is approximated by:

$$\Omega(r_c) \approx \frac{\Gamma_\infty}{2\pi r_c^2} \left\{ 1 - \exp \left[ - \left( \frac{r_c}{r_c} \right)^2 \right] \right\} \approx \frac{0.32\Gamma_\infty}{\pi r_c^2}. \quad (5.19)$$

The parameter  $N$  and thus  $C_D$  is thus a function of the vortex characteristics  $\Gamma_\infty$ ,  $r_c$  and the characteristic particle length  $L$ :

$$C_D \approx 2.60N \approx \frac{1.66\Gamma_\infty (0.5L)}{\pi r_c^2 (\overline{V}_z - U_z)}. \quad (5.20)$$

#### MOTION CONDITION FOR AXIAL MOTION THROUGH VORTEX CORE

By substituting the Taylor drag coefficient in the uniform drag force formula, the axial drag force is defined by the vortex and particle characteristics:

$$F_{D,z} = \frac{0.84\Gamma_\infty |\overline{V}_z - U_z| \rho_f A_N (0.5L)}{\pi r_c^2}. \quad (5.21)$$

By applying equations (5.14) and (5.21), the condition to determine if there is axial motion through the vortex core is approximated by:

$$\frac{0.84\Phi_T \Gamma_\infty \overline{V}_z}{\pi r_c^2 g} \neq \frac{\rho_f - \rho_p}{\rho_f}. \quad (5.22)$$

with  $\Phi_T$  the Taylor drag shape factor as discussed below. By substituting the expression for  $\overline{V}_z$ , equation (5.22) is expressed by:

$$\frac{6.8\Phi_T \Gamma_\infty V_{z,\max,av}}{\pi r_c^2 g L^2} \int_0^{0.5L} \exp \left[ - \left( \frac{r - r_{\max}}{\alpha r_{\max}} \right)^2 \right] r dr \neq \left( \frac{\rho_f - \rho_p}{\rho_f} \right). \quad (5.23)$$

In fact, equation (5.22) expresses the required condition for stage 2 motion through the vortex core as function of the vortex and particle characteristics where the left term presents the dimensionless Taylor drag force term  $N_{D,Taylor}$ :

$$N_{D,Taylor} = \frac{0.84\Phi_T \Gamma_\infty \bar{V}_z}{\pi r_c^2 g}. \quad (5.24)$$

The Taylor drag shape factor is  $\Phi_T = k (A_N/\chi)(0.5L)$ . As Maxworthy's expression for  $C_D$  was determined for spheres,  $k$  is the shape correction factor for the cubes and ellipsoids. As a first approximation  $k$  is taken as the ratio between the standard  $C_D$  of the non-spherical particles and the sphere by using equation (5.6). As the angled orientated cubes have a hexahedron shaped  $A_N$ , the integration domain to calculate  $\bar{V}_z$  is than approximated by taking the average radius of the inner and outer circle circumscribing the hexahedron:  $[0, 0.66L]$ . The ellipsoids orientation in the vortex core changes at the onset of axial motion and during the axial motion through the core. Consequently, the averaged axial velocity  $\bar{V}_z$  over the ellipsoid and its cross-sectional surface  $A_N$  is time depended:

$$\frac{\partial \bar{V}_z}{\partial t} \neq 0, \quad \frac{\partial A_N}{\partial t} \neq 0. \quad (5.25)$$

This implies that the Taylor drag force is time depended as well. The effect of this time dependency is experimentally observed as an oscillation in the orientation of the particle in the flow field. The averaged  $A_N$  is based on 3 orientations, see Figure 5.7. The dimensionless Taylor drag force is then defined as the average of the Taylor-drag force of each orientation:

$$\bar{N}_{D,Taylor} = \frac{1}{N} \left( \frac{0.84\Gamma_\infty}{\pi r_c^2 g \chi} \right) \sum_{i=1}^{N=3} k_i A_{N,i} (0.5L_{N,i}) \bar{V}_{z,i}. \quad (5.26)$$

So, for the three orientations the average dimensionless Taylor drag force is expressed by:

$$\bar{N}_{D,Taylor} = \frac{1}{3} \left( \frac{0.84\Gamma_\infty}{\pi r_c^2 g \chi} \right) 0.5 \left[ k_1 A_{N,1} \bar{V}_{z,1} L_{N,1} + k_2 A_{N,2} \bar{V}_{z,2} L_{N,2} + k_3 A_{N,3} \bar{V}_{z,3} L_{N,3} \right]. \quad (5.27)$$

The  $\bar{V}_z$  of each position is approximated by calculating the surface integral of the ellipsoid using a Cartesian coordinate system with the origin at the center of the ellipsoid and  $V_z(r)$  the scalar variable:

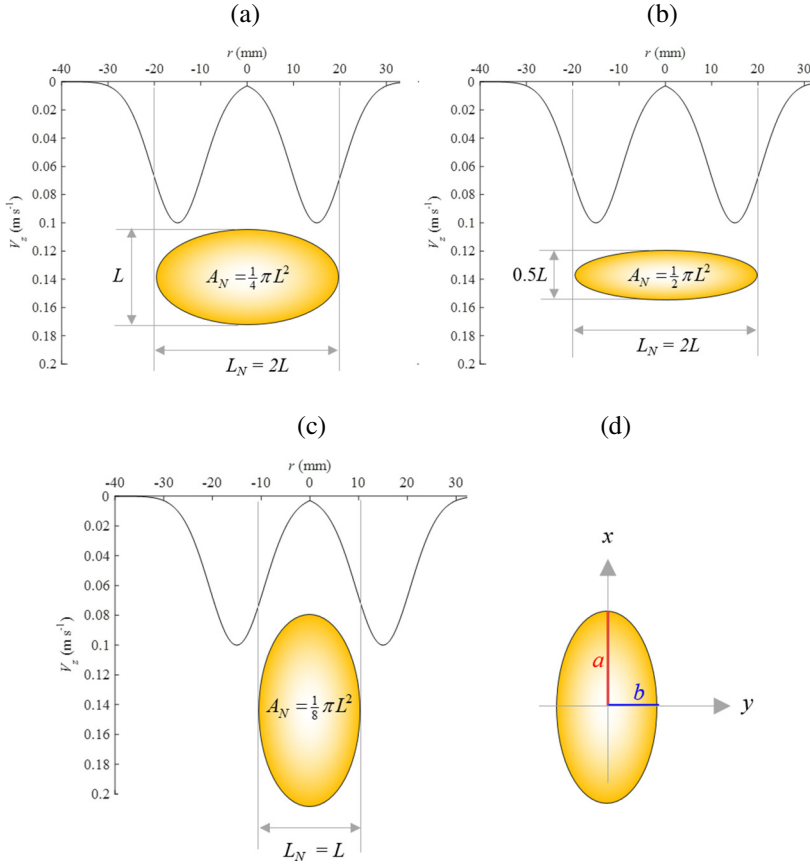


Figure 5.10: (a)-(c) The three positions of the ellipsoid in the vortex core used to determine the time averaged value of  $N_{D,Taylor}$ . (d) Definition of the ellipsoids semi-major and semi-minor axes.

$$\overline{V_{z,i}} = \frac{1}{A_i} \iint_{A_i} V_z(r) dx dy \quad (5.28)$$

$$r = \sqrt{x^2 + y^2}.$$

The integration boundary is calculated by using the ellipsoid's semi-major and semi-minor axes  $a$  and  $b$  with the semi-major axis in the  $x$ -direction, see Figure 5.10:

$$y = \frac{b}{a} \sqrt{a^2 - x^2}. \quad (5.29)$$

The surface integral is numerical solved using a step size  $\Delta x = \Delta y = 0.0005$  m.

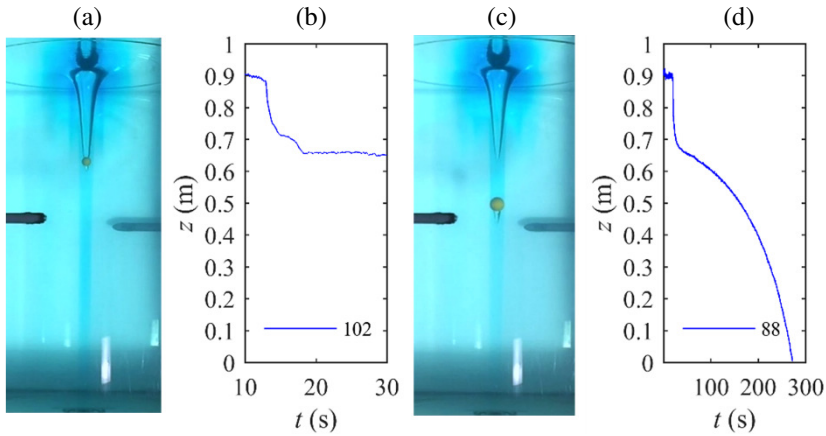


Figure 5.11: Recordings and 3D-PTV results of particle motion at series 6. (a)-(b) ‘No motion’ for sphere 102 (termination condition no. 2) where  $N_B \approx N_{D,Taylor}$ . The stationary situation holds for  $t > 300$  s while the graph is limited to  $t = 30$  s to illustrate the downward motion along the air core. (c)-(d) ‘Indecisive motion’ for sphere 86 (termination condition no. 1 and  $t_a > T$ ) where  $N_B < N_{D,Taylor}$ .

Figure 5.11 shows an example of the influence of the characteristic length on the downward particle motion. Compared to the  $\varnothing 25$  mm sphere (Figure 5.11(a)-(b)), the  $\varnothing 38$  mm sphere (Figure 5.11(c)-(d)) has a four times higher upward buoyancy force but does show a (slow) downward motion. This is due to the significant higher  $\overline{V_z}$  over the spheres cross-sectional area  $A_N$ .

#### EXPERIMENTAL VALIDATION OF THE STAGE 2 MOTION CONDITION

The Taylor drag motion condition is validated with a data set of 65 experiments for the spheres and cubes and 31 experiments for the ellipsoids, see section 5.2.2. Figure 5.12 shows the experimental and theoretical results for the spheres and cubes, see also section 5.2.2 for the experimental conditions. The experimental results are again presented by the labels ‘*Motion*’ and ‘*No motion*’ but supplemented with a label ‘*Indecisive motion*’. This label represents experiments that show a continuous downward motion but with  $t_a > T$  and thus not labelled as ‘*Motion*’. Figure 5.12(a) shows  $N_{D,Taylor}$  as a function of  $N_B$ . Figure 5.12(b) shows  $N_{D,sdc}$  with  $C_D$  determined using the standard drag curve. The line  $N_B = N_D$  represents the condition for ‘*Motion*’ or ‘*No motion*’. Some experiments showed a small air bubble beneath the particle with a maximum diameter of  $\sim 5$  mm. This bubble increases the particle buoyancy. The increase in buoyancy is converted to a decrease in particle density giving a maximum decrease of  $\sim 3\%$ . As the effect of the increase in buoyancy is much smaller than the uncertainty of  $N_D$ , the effect of the small bubble presence is neglected.

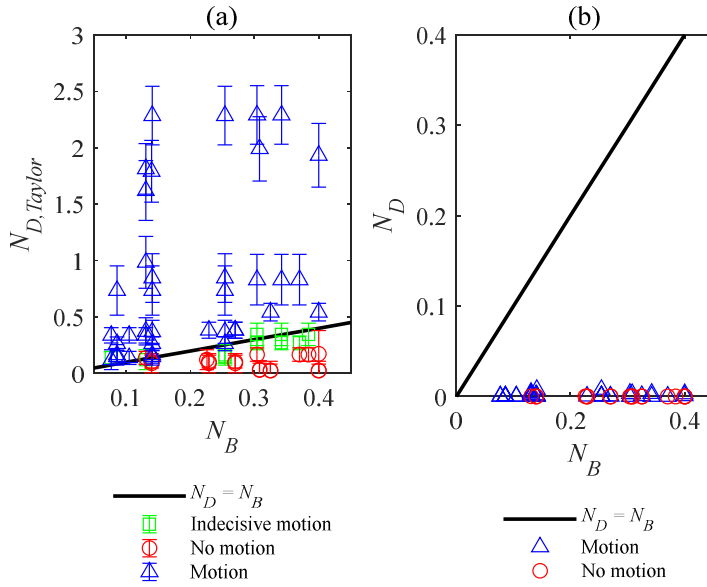


Figure 5.12: Experimental and theoretical results for axial motion of cubes and spheres (a)  $N_{D,Taylor}$  versus  $N_B$  with  $N_{D,Taylor}$  based on the Taylor-column effect. (b)  $N_{D,sdc}$  versus  $N_B$  with  $N_{D,sdc}$  based on the standard  $C_D$  values of equation (5.6).

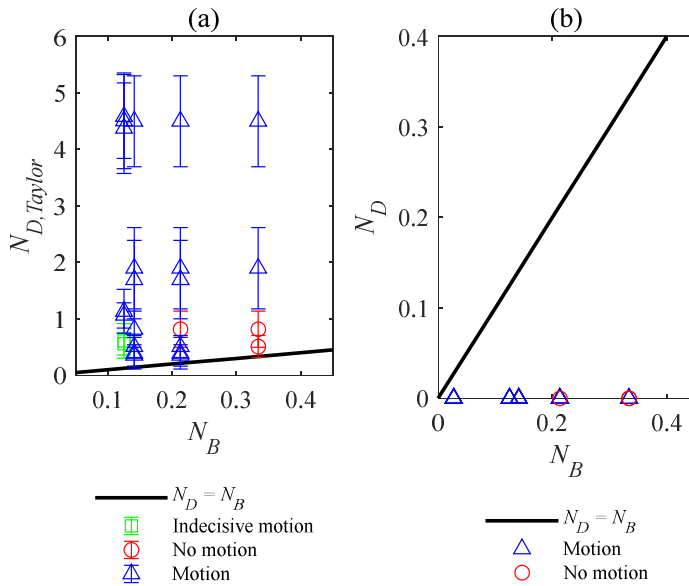


Figure 5.13: Experimental and theoretical results for axial motion of ellipsoids. (a)  $N_{D,Taylor}$  versus  $N_B$  with  $N_{D,Taylor}$  based on the Taylor-column effect. (b)  $N_{D,sdc}$  versus  $N_B$  with  $N_{D,sdc}$  based on the standard  $C_D$  values of equation (5.6).

Figure 5.13 shows the results for the ellipsoids. The results show a systematic overprediction of  $N_{D,Taylor}$ . This is probably due to the disputable assumption that every orientation is subjected to an equal time distribution. The behavior of the ellipsoids shows some similarity with the chaotic motion of an elliptical body due to body-vortex interactions as reported by Roenby & Aref (2010). Hence, it is difficult to provide a representative time distribution of each orientation.

## 5.6 DISCUSSION

The values obtained for  $N_{D,Taylor}$  using equation (5.24) generally match with the experimental results but also reveal a few mismatches. The mismatches are mostly found in experiments in which axial motion was observed but was labelled as '*Indecisive motion*' which opens the proposed motion condition for discussion. For instance, the recovery of the axial flow field after the field is disturbed when placing particles at the air core bottom, mostly leads to an instantaneously higher axial velocity field in the vortex core that introduces an unrealistic particle motion. Another uncertainty is the applicability of Maxworthy's expression of  $C_D$  for non-spherical objects. This is solved by a linear adaption of Maxworthy's expression using the shape correction factor  $k$ . However, the study of Tanzosh & Stone (1994) showed that for Taylor numbers  $T_a > \sim 10^3$ , the drag is determined by the cross-sectional area of the particle where the shape is less important and thus  $k = 1$  for non-spherical objects. In the present study  $T_a$  is in the range between  $\sim 3 \cdot 10^3$  and  $\sim 7 \cdot 10^4$  so the influence of the shape would be negligible. But the results of Tanzosh & Stone (1994) are for Stokes flow and the present study has a  $Re_{p,z}$  range between  $\sim 10^2$  and  $\sim 6 \cdot 10^3$  implying the Stokes condition is not met. Consequently and within the range of the authors' knowledge, the effect of non-spherical shapes on the Taylor drag is not entirely clear. Maxworthy's expression of  $C_D$  is determined in a full solid body rotation fluid while in the present study for the free-surface vortex, the solid body rotation is limited to a maximal radial range of  $r \sim r_c$ . If  $r_c < 0.5L$ , a part of the particle is located outside the solid body region. This effect on the Taylor-column formation is unknown and not taken into account. In conclusion, the stage 2 motion condition described by equation (5.22) provides a first indication when axial motion of buoyant particles occurs.

## 5.7 CONCLUSIONS

The downward motion of spherical, cubical and ellipsoidal shaped experimental particles through the free-surface vortex core is determined by the unbalance between the particle buoyancy force and the fluid drag force. It was found that the uniform drag force approach based on the standard drag coefficients  $C_D$  is insufficient to model the axial drag force in the rotating vortex core as the results do not match the

experimental results presented. The  $C_D$  in this solid-body rotating core seems to be determined by the presence of a Taylor-column under the particle and valid for Rossby number  $Ro < \sim 0.3$ . The  $C_D$  coefficient is then a function of the characteristic particle length  $L$  and the vortex core angular speed  $\Omega$  which is a function of the vortex characteristics  $\Gamma_\infty$ ,  $r_c$  and  $V_z$ . Based on this Taylor column drag force, a motion condition is proposed that provides a first indication if downward axial motion occurs as a function of the particle and vortex characteristics.



# 6

## **CONCLUSIONS AND RECOMMENDATIONS**

## 6.1 CONCLUSIONS

The structure of this section is as follow: first section 6.1.1 addresses the conclusions of the study on the free-surface vortex flow characteristics. Section 6.1.2 addresses the conclusions of the study on the vortex driven motion of buoyant particles and section 6.1.3 addresses a general conclusion on the potential of the vortex as a mean for downward transport of buoyant particles

### 6.1.1 CONCLUSIONS ON THE FREE-SURFACE VORTEX

1. Based on experiments with a vertical suction outlet and for the area between the air core bottom and the bottom Ekman layer, the circumferential velocity profile of the free-surface vortex is in good approximation independent of the vertical coordinate ( $\partial V_\theta / \partial z \approx 0$ ). So, the free-surface vortex can be assumed as an 2D line vortex.
2. Based on the characteristic vortex parameters  $r_c$  and  $\Gamma_\infty$ , where  $\Gamma_\infty$  is assumed to be equal to  $\Gamma$  at  $r \approx 3r_c$ , the Burgers vortex model (1948) produces a sufficiently accurate estimate of the circumferential velocity profile.
3. The Burgers model quantifies the air core depth with an uncertainty of 20% for the experimental range presented in this thesis. At the design stage of a WWPS, there is a safety margin in distance between the air core depth and the suction inlet depth. The uncertainty in calculated air core depth is negligible when compared to this margin. Consequently, the validity of the Burgers model is assumed as acceptable for engineering applications.
4. The horizontal radial inflow is observed as primary concentrated near the vortex core with a maximum velocity around  $r_c$  and being zero in the outer field.
5. The axial velocity profiles show that the axial down-flow is primary concentrated in a region with a radius comparable to approximately 2 to  $3r_c$  while showing a Gaussian shaped profile with a maximum around  $r_c$ . Integration of the measured axial profiles shows that between 10% and 25% of the flow is transported through the vortex core.

### 6.1.2 CONCLUSIONS ON THE FREE-SURFACE VORTEX DRIVEN MOTION OF BUOYANT PARTICLES

6. The experiments revealed two distinct stages in the vortex driven motion of buoyant particles. The stage 1 motion is characterized by the particle following a helical motion along the vortex air core until the particle reaches the air core bottom where the particle centralizes in the vortex core. During the helical downward motion, the particle may be ejected out of the air core or reaches a

more or less stable orbit around the air core at some depth. The stage 2 motion is the axial motion through the vortex core where the particle is centralized in the core. In this stage the particle either shows a continuous downward axial motion towards the outlet or the particle remains in position at the air core bottom.

7. The vortex driven particle motion has a very sensitive dependence on the particle initial conditions i.e. the initial velocity  $\mathbf{V}$  and rotation  $\boldsymbol{\Omega}_p$  by showing chaotic behavior. Consequently, the vortex driven particle motion has limited predictability. The motion can only be analysed in a qualitative manner by applying phase portraits.
8. The stage 1 motion through the vortex flow of cubical and ellipsoidal shaped experimental particles with similar characteristics i.e. characteristic length  $L$  and density  $\rho_p$  showed to be less sensitive to the particle initial conditions and thus showed less chaotic behavior.
9. Without having access to the detailed experimental data collected by Voßwinkel (2017) for verification, a possible explanation for the statistical relations found between vortex and particle characteristics may be found in the chaotic behavior of the vortex-particle interaction as shown in this thesis.
10. At the stage 1 motion, the spherical particles are subjected to a lift force that can terminate the downward motion by ejecting the particle out of the air core. This behavior is not observed for cubical and ellipsoidal shaped particles.
11. For the stage 1 motion of spherical particles, a motion parameter is proposed which provides a first indication if a continuous downward motion along the air core occurs as function of the system parameters that includes  $\Gamma_\infty$  and  $r_c$ .
12. It is useless to predict the stage 2 motion of spherical, cubical and ellipsoid shaped particles by applying the uniform drag force approach and the standard drag coefficients  $C_D$ .
13. The  $C_D$  in the solid-body rotating core seems to be determined by the presence of a Taylor-column under the particle and valid for Rossby number  $Ro < \sim 0.3$ . The coefficient is determined by the vortex core angular speed that is a function of both the vortex and particle characteristics (the characteristic length).
14. For the stage 2 motion, a motion condition is proposed that provides a first indication if downward motion through the vortex core occurs as a function of the particle and vortex characteristics.

### 6.1.3 GENERAL CONCLUSION ON THE POTENTIAL OF A FREE-SURFACE VORTEX AS A MEAN FOR THE DOWNWARD TRANSPORT OF BUOYANT PARTICLES

The free-surface vortex is a potentially effective mean for the downward transport of buoyant particles. However, the effectivity is strongly determined by the combination of the particle shape, particle initial conditions and the vortex flow characteristics. As the experimental observations show a chaotic behavior, the motion of the particle has a limited predictability and hence, the motion can only be analysed in a qualitative manner by applying phase portraits. During the downward helical motion along the vortex air core, spherical particles with an (initial) rotation direction equal to vortex rotation are subjected to lift forces. An unbalance between the lift and inertial forces can eject the particle out of the vortex. Cubical or ellipsoid shaped particles prove to be less sensitive to this mechanism. Regarding the axial motion through the vortex core, the motion depends, apart from the axial velocity and particle density, strongly on the ratio between the particle length  $L$  and the vortex core radius  $r_c$  and is found to be less sensitive to the particle's shape.

### 6.1.4 ENGINEERING ASPECTS

To apply the vortex as a transport mechanism in practice, data of the hydraulic and geometrical conditions is required that provides the occurrence of a vortex with sufficient strength (strength 4 to 6, see Figure 1.6). To obtain these conditions, a single-phase CFD model can be a quick and effective engineering tool. However, the question arises on the reliability of single-phase CFD as engineering tool for vortices. To obtain an indication of its reliability, the physical results of two cases (both cases comprise a rectangular shaped geometry with a jet-shaped inflow) were qualitatively compared with CFD results. A detailed description of the cases and comparison is addresses in Appendix F. Based on these comparisons and concerning rectangular geometries, the conclusion is that single-phase CFD seems able to provide a first indication of the possible occurrence of a free-surface vortex. However, the use of single-phase model for an accurate simulation of the vortex location and strength is unrealistic. To obtain detailed information i.e. the vortex location and air core depth, the use of physical (scale) models is preferred.

## 6.2 RECOMMENDATIONS

1. (Minor) secondary flow patterns in the vortex flow were not observed due to the SPIV method's measure uncertainty. To obtain a more complete insight in the vortex flow, research on the presence and quantification of secondary velocity profiles is recommended.
2. The vortex's axial velocity profiles  $V_z(r,z)$  are only measured in horizontal planes through the rotating vortex core. Measuring the profiles along the air core with

Stereo Particle Image Velocimetry (SPIV) was found to be difficult due to the presence of the water-air interface. However, for a detailed analysis of the vortex driven motion along the air core, it is recommended to obtain knowledge of  $V_z(r,z)$  along the vortex air core.

3. In this research, the important vortex core radius  $r_c$  is determined by measurements. An accurate prediction of  $r_c$  by a mathematical model seems to be highly depended on the geometry in which the vortex occurs. To avoid (expensive) experimental set-ups for the determination of  $r_c$ , further research on the prediction of  $r_c$  is recommended.
4. The applied mathematical model for the prediction of the stage 1 motion is a two-dimensional model in the horizontal plane. For an accurate prediction of this motion, the vertical motion component must be included in the model.
5. The computation of the Taylor-column drag coefficient  $C_D$  for non-spherical shaped particles is based on the experimental results of a sphere (Maxworthy, 1970) and by applying a shape correction factor. The validity of this approach is, however, uncertain. It is recommended therefore to conduct experiments on the characteristics of a Taylor-column and  $C_D$  for rising non-spherical objects.
6. The formation of a Taylor-column by a rising object in a fluid that is not in full solid-body rotation, i.e. the free-surface vortex flow, is unknown. To optimize the validity range of the proposed stage 2 motion condition, more research on the Taylor-column formation in free-surface vortex flows is recommended.
7. The orientation of the point-symmetric cubical and spherical particles in the vortex core was found to be approximately stationary, see Figure 5.7. However, the ellipsoidal shaped particles showed a dynamic orientation, see Figure 5.7(b-d). For an accurate prediction of the axial motion through the vortex core for non-point symmetric particles, research on the dynamical orientation is recommended.
8. This research is conducted with a vertically oriented outlet i.e. the flow direction in the outlet is nearly vertical, see Figure 2.1(a). Vortex transport with a horizontally placed outlet is not studied and is recommended for further study.
9. Based on maintenance data of real WWPS, Nieuwenhuis *et al.* (2018) showed a negative correlation between the wastewater kinetic energy density and the occurrence of floating solids. Consequently, this could be a simple but effective mean to reduce the formation of layers of accumulated floating solids. It is highly recommended therefore to study the potential of kinetic energy density as a transport means in a controlled experimental set-up.

10. It is recommended to conduct extensive research to the validity of CFD as an engineering tool for the occurrence of free-surface vortices in irregular shaped pump sumps.

# REFERENCES

- ADRIAN, R.J. & WESTERWEEL, J. (2011). Particle image velocimetry. No. 30. *Cambridge University Press*.
- ANDERSEN, A., BOHR, T., STENUM, B., JUUL RASMUSSEN, J. & LAUTRUP, B. (2006). The bathtub vortex in a rotating container. *Journal of Fluid Mechanics*, 556, 121-146.
- ANWAR, H.O. (1966). Formation of a Weak Vortex. *Journal of Hydraulic Research*, 4(1), 1-16.
- ANWAR, H.O., WELLER, J.A. & AMPHLETT, M.B. (1978). Similarity Of Free-Vortex At Horizontal Intake. *Journal of Hydraulic Research*, 16(2), 95-105.
- ANWAR, H.O. & AMPHLETT, M.B. (1980). Vortices at vertically inverted Intake. *Journal of Hydraulic Research*, 18(2), 123-134.
- AMERICAN NATIONAL HYDRAULIC STANDARDS INSTITUTE (2012). *American National Standard for rotodynamic pumps for pump intake design*. ANSI 9.8-2012. ISBN 978-880952-70-2.
- AUTON, T.R. (1987). The lift force on a spherical body in a rotational flow. *Journal of Fluid Mechanics*, 183, 199-218.
- AUTON, T.R., HUNT, J.C.R. & PRUD'HOMME, M. (1988). The force exerted on a body in inviscid unsteady non-uniform rotational flow. *Journal of Fluid Mechanics*, 197, 241-257.
- BAGCHI, P. & BALACHANDAR, S. (2002). Shear versus vortex-induced lift force on a rigid sphere at moderate Re. *Journal of Fluid Mechanics*, 473, 379-388.
- BASHKATOV, A.N. & GENINA, E.A. (2003) Water refractive index in dependence on temperature and wavelength: a simple approximation. *Saratov Fall Meeting 2002: Optical Technologies in Biophysics and Medicine IV*, Valery V. Tuchin, Editor, Proceedings of SPIE Vol. 5068.
- BAYATI, M., SABERI, A. & GLEICH, F.D. (2009). Algorithms for Large, Sparse Network Alignment Problems. In: *ACM Transactions on Knowledge Discovery from Data*.

- BERKLITE, R.B. (1972). Added mass of submerged objects of arbitrary shape. *Naval Postgraduate School*, Monterey, California, U.S.A.
- BLUEMINK, J.J., LOHSE, D., PROSPERETTI, A. & VAN WIJNGAARDEN, L. (2009). Drag and lift forces on particles in a rotating flow. *Journal of Fluid Mechanics*, 1-31.
- BROCARD, D.N., BEAUCHAMP, C.H. & HECKER, G.E. (1983). Analytic Predictions of Circulation and Vortices at Intakes (Research Project 1199-8). Holden, MA: Alden Research Laboratory (US).
- BURGERS, J.M. (1948). A Mathematical Model Illustrating the Theory of Turbulence. *Advances in Applied Mechanics*, 1, 171-199.
- BUSH, J.W.M., STONE, H.A. & TANZOSH, J.P. (1994). Particle motion in rotating viscous fluids: Historical survey and recent developments. *Current Topics in The Physics of Fluids*, 1.
- BUSH, J.W.M., STONE, H.A. & BLOXHAM, J. (1995). Axial drop motion in rotating fluids. *Journal of Fluid Mechanics*, 282, 247-278.
- CIDDOR, P.E. (1996). Refractive index of air: new equations for the visible and near infrared. *Applied Optics Vol. 35*, No. 9 pp 1566-1573. Dagget, L.L. & Keulegan, G.H. 1974. Similitude Conditions in Free Surface Vortex Formations. *Journal of Hydraulics Division*, 100, 1565-1581.
- DELAUNAY, B. (1934). On the empty sphere. In memory of Georges Voronoi, Org. title: "Sur la sphère vide. A la mémoire de Georges Voronoi", *Bulletin de l'Académie des Sciences de l'URSS. Classe des sciences mathématiques et naturelles*, 1934, 6, 793-800.
- DUINMEIJER, S.P.A., CLEMENS, F.H.L.R. AND VERHAART, F. (2015, September). On the research to free-surface vortices in wastewater pump sumps. *Paper Presented at the 10<sup>th</sup> Int. Urban Drainage Modelling Conference, Québec, Canada*.
- DUINMEIJER, S.P.A. & CLEMENS, F.H.L.R. (2016, September). Experimental research on free-surface vortices as transport mechanism in wastewater sumps. *Paper presented at the 8<sup>th</sup> Int. Conference on Sewer Processes and Networks, Rotterdam, The Netherlands*.
- DUINMEIJER, S.P.A., MORENO-RODENAS, M.A., LEPOT, M., NIEUWENHUIZEN VAN, C., MEYER, I. & CLEMENS, F.H.L.R. (2019a). A Simple measuring set-up for the experimental determination of the dynamics of a large particle in the 3D velocity field around a free-surface vortex. *Journal of Flow Measurement and Instrumentation*, doi.org/10.1016/j.flowmeasinst.2018.10.007.

- DUINMEIJER, S.P.A., OLDENZIEL, G. & CLEMENS, F.H.L.R. (2019b). Experimental study on the 3D-flow field of a free-surface vortex using stereo PIV. *Journal of Hydraulic Research*, DOI: 10.1080/00221686.2018.1555558.
- DUINMEIJER, S.P.A. & CLEMENS, F.H.L.R. (2019c). (subm.). Experimental study on free-surface vortex driven particle motion at high Reynolds numbers: helical motion along the air core. Submitted to *Journal of Hydraulic Research*.
- DUINMEIJER, S.P.A. & CLEMENS, F.H.L.R. (2019d). (subm.). Experimental study on free-surface vortex driven particle motion at high Reynolds numbers: axial motion through the vortex core. Submitted to *Journal of Hydraulic Research*.
- ECKMANN, J.P. & RUELLE, D. (1992). Fundamental limitations for estimating dimensions and Lyapunov exponents in dynamical systems. *Physica D* 56 (1992) 195.
- ECHÁVEZ, G. & MCCANN, E. (2002). An experimental study on the free surface vertical vortex. *Experiments in Fluids*, 33, 414-421.
- EINSTEIN, H. A., & LI, H. L. (1951). Steady vortex flow in a real fluid. *Proceedings of the Heat Transfer and Fluid Mechanics Institute*, 4, 33-43.
- FUKADA, T., TAKEUCHI, S. & KAJISHIMA, T. (2014). Effects of curvature and vorticity in rotating flows on hydrodynamic forces acting on a sphere. *International Journal of Multiphase Flow*, 58, 292-300.
- GRANGER, R.A. (1995). *Fluid Mechanics*. New York, NY: Dover Publications Inc.
- GHYS, E. (2010). The Lorenz Attractor, a Paradigm for Chaos. *Translation by Stephane Nonnenmacher from the original French text: Seminaire Poincare XIV*, 1-52.
- GULLIVER, S. & RINDELS, A.J. (1987). Weak Vortices at Vertical Intakes. *Journal of Hydraulic Engineering*, 113, 1101-1116.
- HEIKKILA, J. & SILVÉN, O. (1997). A four-step camera calibration procedure with implicit image correction. *Proceedings 1997 IEEE Computer Society Conference on Computer Vision and Pattern Recognition*, 1106-1112.
- HITE, E.J. & MIH, W.C. (1994). Velocity of Air-Core Vortices at Hydraulic Intakes. *Journal of Hydraulic Engineering*, 120(3), 284-297.
- HOLZER, A. & SOMMERFELD, M. (2008). New simple correlation formula for the drag coefficient of non-spherical particles. *Powder Technology*, 184, 361-365.

- ITO, K., EZURE T. & OHSHIMA, H. (2014). Development of vortex model with realistic axial velocity distribution. *The Japan Society of Mechanical Engineers*, 80(818).
- JONES, G.M. & SANKS, R.L. (2008). *Pumping Station Design* (Third Edition), Elsevier Ltd.
- KASAROVA, S.N., SULTANOVA, N.G., IVANOV, C.D. & NIKOLOV, I.D. (2007). Analysis of the dispersion of optical plastic materials. *Optical Materials* 29, 1481-1490.
- KEENER, K.M., DUCOSTE, J.J. & HOLT, L.M. (2008) "Properties Influencing Fat, Oil, and Grease Deposit Formation." *Water Environment Research* 80 (12): 2241-46.
- KORVING, J.L., CLEMENS F.H.L.R., & VAN NOORTWIJK J.M. (2006). Statistical Modelling of the Serviceability of Sewage Pumps. *Journal of Hydraulic Engineering*, 132, 1076-1085.
- LORENZ, E.N. (1963). Deterministic nonperiodic flow. *Journal of the Atmospheric Sciences*, 20, 130-141.
- LUKERCHENKO, N., KVURT, YU., KEITA, I., CHARA, Z. & VLASAK, P. (2012). Drag Force, Drag Torque, and Magnus Force Coefficients of Rotating Spherical Particle Moving in Fluid, *Particulate Science and Technology*, 30:1, 55-67.
- MARQUART, D. (1963). An algorithm for least-squares estimation of nonlinear parameters, *SIAM J. Appl. Math.* 11(2), 431-441.
- MAXWORTHY, T. (1970). The flow created by a sphere moving along the axis of a rotating, slightly-viscous fluid. *Journal of Fluid Mechanics*, 40, 453-479.
- MEI, R. (1992). An approximate expression for the shear lift force on a spherical particle at finite Reynolds number. *International Journal of Multiphase flows*, 18(1), 145-147.
- MEINHART C., WERELEY, S. & SANTIAGO, J. (2000). A PIV algorithm for estimating time-averaged velocity fields. *Journal of Fluids Engineering*, 122, 285-289.
- MIH, W.C. (1990). Discussion of Analysis of fine particle concentrations in a combined vortex. *Journal of Hydraulic Research*, 28(3), 392-395.
- MOORE, D.W. & SAFFMAN, P.G. (1968). The rise of a body through a rotating fluid in a container of finite length. *Journal of Fluid Mechanics*, 31(4), 635-642.

- MOORE, D.W. & SAFFMAN, P.G. (1969). The structure of free vertical shear layers in a rotating fluid and the motion produced by a slowly rising body. *Phil. Trans. Roy. Soc. London. A* 264, 597-643.
- NIEROP VAN, E.A., LUTHER, S., BLUEMINK, J.J., MAGNAUDET, J., PROSPERETTI, A. & LOHSE, D. (2007). Drag and lift forces on bubbles in a rotating flow. *Journal of Fluid Mechanics*, 571, 439-454.
- NIEUWENHUIS, E., POST J., DUINMEIJER A., LANGEVELD, J. & CLEMENS, F. (2018). Statistical modelling of Fat, Oil and Grease (FOG) deposits in wastewater pump sumps. *Water Research*, 135, 155-167.
- NIEUWENHUIZEN, C. (2017) Floating solids transport in pump sumps by means of controlled free-surface vortices (research into the possibilities of transporting Fat, Oil and Grease with controlled vortices) B.Sc thesis, Delta academy, HZ University of Applied Sciences.
- ODGAARD, A. J. (1986). Free-surface air core vortex. *Journal of Hydraulic Engineering*, 112(7), 610-620.
- PENNINGS, P. C., WESTERWEEL, J. & VAN TERWISGA, T.J.C. (2015). Flow field measurement around vortex cavitation. *Experiments in Fluids*, 56(11), 1-13.
- POELMA, C. (2017). Ultrasound Imaging Velocimetry: a review. *Experiments in fluids*, Jan. 2017, 58:3.
- POWELL, M.J.D. (1970). *A Fortran Subroutine for Solving Systems of Nonlinear Algebraic equations*. Numerical Methods for Nonlinear Algebraic equations, (P. Rabinowitz, ed.), Chapter 7.
- PROUDMAN, J. (1916). On the motion of solids in a liquid possessing vorticity. *Proc. Roy. Soc. London A*. 92, 408.
- RANKINE, W.J.M. (1858). *Manual of Applied Mechanics*. London: R. Griffin & Co.
- RINDELS, A.J. & GULLIVER, J.S. (1983). *An experimental study of critical submergence to avoid free-surface vortices at vertical intakes* (Report No. 224). Minneapolis (MN): University of Minnesota (US).
- ROENBY, J. & AREF, H. (2010). Chaos in body-vortex interactions. *Proc. Roy. Soc. A*. 466, 1871-1891.
- ROSENHEAD, L. (1930). The spread of vorticity in a wake behind a cylinder. *Proceedings of the Royal Society A*, 27(806), 590-612.

- ROSENSTEIN, M.T., COLLINS, J.J. & DELUCA, C.J. (1993) A practical method for calculating the largest Lyapunov exponents from small data sets. *Physica D* 65, 117-134.
- SAFFMAN, P.G. (1965). The lift on a small sphere in a slow shear flow. *Journal of Fluid Mechanics*, 22, 385-400.
- SAFFMAN, P. G. (1968). Corrigendum to "The lift on a small sphere in a slow shear flow". *Journal of Fluid Mechanics*, 31, 624.
- SMID, M. & MATAS, J. (2017). Rolling shutter camera synchronization with sub-millisecond accuracy, in: *Proceedings of the VISAPP - 12th International Conference on Computer Vision Theory and Applications*, 2017.
- STEWARTSON, K. (1952). On the slow motion of a sphere along the axis of a rotating fluid. *Proc. Camb. Phil. Soc.* 48, 168-177.
- STICHTING TOEGEPAST ONDERZOEK WATERBEHEER (2012). *Hydraulisch Ontwerp en beheer afvalwatertransportsystemen*. Stowa 2012-48. ISBN 978.90.5773.586.8.
- SOLOFF, S., RONALD, M., ADRIAN, J. & ZI-CHAO, L. (1997) Distortion compensation for generalized stereoscopic particle image velocimetry. *Measurement science and technology*, 8(12), 1441.
- SUERICH-GULICK, F., GASKIN, S.J., VILLENEUVE, M. & PARKINSON, E. (2014a). Free surface intake vortices: Scale effects due to surface tension and viscosity. *Journal of Hydraulic Research*, 52(4), 513-522.
- SUERICH-GULICK, F., GASKIN, S.J., VILLENEUVE, M. & PARKINSON, E. (2014b). Characteristics of Free Surface Vortices at Low-Head Hydropower Intakes. *Journal of Hydraulic Engineering*, 140, 291-299.
- SUN, H., LIU, Y. (2015). Theoretical and experimental study on the vortex at hydraulic intakes. *Journal of Hydraulic Research*, 53(6), 787-796.
- TANZOSH, J.P. & STONE, H.A. (1994). Motion of a rigid particle in a rotating viscous flow: an integral equation approach. *Journal of Fluid Mechanics*, 275, 225-256.
- TAYLOR, G.I. (1917). Motion of solids in fluids when the flow is not irrotational. *Proc. Roy. Soc. London A*. 93, 99.
- TIO, K-K., LIÑÁN A., LASHERES, J.C. & GAÑAN-CALVO, M. (1993). On the dynamics of buoyant and heavy particles in a periodic Stuart vortex flow. *Journal of Fluid Mechanics*, 254, 671-699.

- VATISTAS, G.H., (1989) Analysis of fine particle concentrations in a combined vortex. *Journal of Hydraulic Research*, 27(3), 417-427.
- VOBWINKEL, N. (2017). Transportvermögen von Einlaufwirbeln [Transport capacity of free-surface vortices], Band: 21, Reihe: Bericht-Lehr- und Forschungsgebiet Wasserwirtschaft und Wasserbau, ISBN 978-3-8440-5242-8. Shaker Verlag GmbH Germany.
- WANG, Y., JIANG, C. & LIANG, D. (2011). Comparison between empirical formulae of intake vortices. *Journal of Hydraulic Research*, 49(1), 113-116.
- WESTERWEEL, J. & SCARANO, F. (2005) Universal outlier detection for PIV data. *Experiments in Fluids*, 39(6), 1096-1100.
- YING, H., LIANG, B., YANG., J. SHUNZHI, L., & HE, J. (2017). An Iterative Closest Point Algorithm for Registration of 3D Laser Scanner Point Clouds with Geometric Features. *Sensors 2017*, 17, 1862.



# A

## 3D-PARTICLE TRACKING VELOCIMETRY

### A.1 DESIGN OF THE RAY-TRACING TECHNIQUE

The path of a light ray is determined by the position of the camera, the position of the observed particle by the camera (focussed on the side wall of the outer tank's wall), the geometry of the setup and the optical properties of the matter through which the light travels (i.e. air, water and acrylate (PMMA)). For reconstructing the light path intersection points between the path of the light and planes (outer and inner surface of the outer tank and the intersection of the light path with the inner and outer wall of the cylinder) as well as the effects of refraction have to be determined. In the following the basic equations to do so are presented. Figure A.1 shows an example of the result.

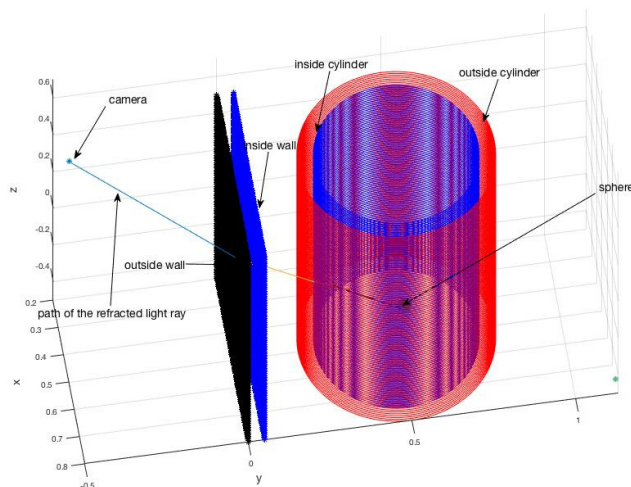


Figure A.1: Intersection of a line with planes, cylinder, walls and sphere.

A plane  $p$  is defined by:

$$\bar{x}_p = \bar{S}_p + \lambda \bar{r}_1 + \xi \bar{r}_2. \quad (\text{A.1})$$

A line  $l$  is defined by:

$$\bar{x}_l = \bar{S}_l + \gamma \bar{r}_l. \quad (\text{A.2})$$

The intersection point  $x_p$  is defined by:

$$\bar{0} = \bar{S}_p - \bar{S}_l + \lambda \bar{r}_1 + \xi \bar{r}_2 - \gamma \bar{r}_l \quad (\text{A.3})$$

or:

$$\bar{0} = \bar{S}_p - \bar{S}_l + \lambda \bar{r}_1 + \xi \bar{r}_2 - \gamma \bar{r}_l \quad (\text{A.4})$$

or:

$$\bar{r}_4 = A^{-1} * (\bar{S}_l - \bar{S}_p) = [\lambda, \xi, \gamma]. \quad (\text{A.5})$$

With:

$$A = \begin{bmatrix} r_1(1) & r_2(1) & -r_l(1) \\ r_1(2) & r_2(2) & -r_l(2) \\ r_1(3) & r_2(3) & -r_l(3) \end{bmatrix}. \quad (\text{A.6})$$

And finally:

$$\bar{x}_p = \bar{S}_l + \bar{r}_4(3) \bar{r}_l = \bar{S}_p + \bar{r}_4(1) \bar{r}_1 + \bar{r}_4(2) \bar{r}_2. \quad (\text{A.7})$$

#### INTERSECTION LINE AND CYLINDER

A cylinder of infinite length is defined by an axis (directional vector  $n_c$ ) and radius  $r$ .

A line  $l$  is defined by  $\bar{x}_l = \bar{S}_l + \lambda \bar{r}_l$ . The intersection of this line with a cylinder with radius  $r$ , axis  $n_c$  and support vector  $S_c$  is defined by:

$$\left\| (\bar{S}_l - \bar{S}_c - \lambda \bar{r}_l) \times \bar{n}_c \right\|^2 - r^2 = 0. \quad (\text{A.8})$$

An analytical solution for equation (A.8) is:

$$a\lambda^2 + b\lambda + c = 0. \quad (\text{A.9})$$

With:  $\bar{x} = (\bar{s}_l - \bar{s}_c)$ ,  $\bar{y} = \bar{r}_l \times \bar{n}_c$ ,  $D = r^2 \bar{n}_c \cdot \bar{n}_c$ ,  $a = \bar{y} \cdot \bar{y}$ ,  $b = 2(\bar{x} \cdot \bar{y})$  and  $c = \bar{x} \cdot \bar{x} - D$  which is solved for  $\lambda$  resulting in the following possible scenarios: (1) one intersection point, (2) two intersection points, (3) the line is parallel to the axis of

the cylinder (so, either no intersection or an infinite number when the line is a distance equal to the radius of the cylinder) and (4) no intersection at all. Condition 3 is tested by if:

$$\frac{\vec{r}_l \times \vec{n}_c}{\|\vec{r}_l\| \|\vec{n}_c\|} = 1 \quad (\text{A.10})$$

the line is parallel to the axis of the cylinder. Condition 4 is tested by the minimal distance between the line  $l$  and the axis of the cylinder:

$$d = \frac{(\vec{S}_c - \vec{S}_l) \cdot (\vec{n}_c \times \vec{r}_l)}{\|(\vec{n}_c \times \vec{r}_l)\|}. \quad (\text{A.11})$$

If  $d > r$  then there is no intersection point, when  $d = r$  and condition 3 is not met, there is one intersection point and otherwise there are 2 intersection points depending on the value of the discriminant of equation (A.9).

#### INTERSECTION LINE AND SPHERE

For a sphere a similar procedure is followed as described for the cylinder, in this case the equation for the 3D object is:

$$\vec{X}_s - \vec{S}_s^2 = r^2. \quad (\text{A.12})$$

The equation for the line is:

$$\vec{X}_l = \vec{S}_l + \lambda \vec{r}_3. \quad (\text{A.13})$$

Combining Equations (A.12) and (A.13) leads to the following analytical solution in  $\lambda$ :

$$\lambda_{1,2} = \frac{-2[\vec{r}_3 \cdot (\vec{S}_l - \vec{S}_s)] \pm \sqrt{[2\vec{r}_3 \cdot (\vec{S}_l - \vec{S}_s)]^2 - 4\vec{r}_3 \cdot [\|\vec{S}_l - \vec{S}_s\|^2 - r^2]}}{2\vec{r}_3 \cdot \vec{r}_3}. \quad (\text{A.14})$$

Here, the following scenarios are possible and depending on the numerical value of the discriminant: (1) no solution, (2) one solution and (3) two solutions.

#### SNELL'S LAW IN 3D

Let  $n$  be the outward facing normal to a surface  $A$  and let  $r$  be the directional vector of a line (light ray)  $B$ , while  $n_1$  and  $n_2$  are the refraction indices of the materials (see Figure A.2): the directional vector  $r_{out}$  of the refracted beam is defined by:

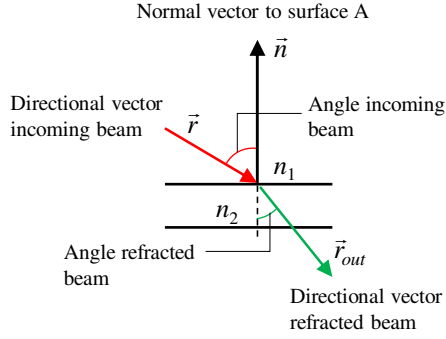


Figure A.2: Schematic overview of Snell's law.

$$\vec{r}_{out} = \frac{n_1}{n_2} [\vec{n} \times (-\vec{n} \times \vec{r})] - \vec{n} \sqrt{1 - \left(\frac{n_1}{n_2}\right)^2 (\vec{n} \times \vec{r}) \cdot (\vec{n} \times \vec{r})}. \quad (\text{A.15})$$

### TRIANGULATION

Combining two camera lines  $i$  and  $j$  ( $i, j \in \{1, \dots, 6\} \mid i \neq j$ ) yields:

$$\begin{aligned} \vec{v}_i &= \vec{s}_i + \lambda \vec{r}_i \\ \vec{v}_j &= \vec{s}_j + \lambda \vec{r}_j. \end{aligned} \quad (\text{A.16})$$

The location where the distance between the lines is minimal can be calculated by finding the shortest line segment that can be found between two lines. The coordinates of the two points defining this line segment are determined by:

$$\begin{aligned} c_1 &= \vec{s}_i + \frac{(\vec{s}_j - \vec{s}_i) \cdot \vec{n}_j}{\vec{r}_i \cdot \vec{n}_j} \vec{r}_i \\ c_2 &= \vec{s}_j + \frac{(\vec{s}_i - \vec{s}_i) \cdot \vec{n}_i}{\vec{r}_j \cdot \vec{n}_i} \vec{r}_j \end{aligned} \quad (\text{A.17})$$

with:

$$\begin{aligned} \vec{n} &= \vec{r}_i \times \vec{r}_j \\ \vec{n}_i &= \vec{r}_i \times \vec{n} \\ \vec{n}_j &= \vec{r}_j \times \vec{n}. \end{aligned} \quad (\text{A.18})$$

For each combination of cameras  $i$  and  $j$ , the following estimate for the location of the object is defined by:

$$p_{est,i,j} = 0.5(c_{1,ij} + c_{2,ij}). \quad (\text{A.19})$$

When  $N$  cameras are used, the number of combinations for position estimation are:

$$n_{com} = \binom{N}{2} = \frac{N!}{2!(N-2)!}. \quad (\text{A.20})$$

When the particle is visible for all 6 cameras this yields to:

$$n_{com} = \binom{6}{2} = \frac{720}{2 \cdot 24} = 15.$$

When the particle is behind the air core of the vortex, the image gets blurred due to hard to compensate image distortions which happens for maximal 3 cameras at the same time. In that case only 3 cameras can be used to obtain a 2D position estimate and thus the number of combinations for position estimation is:

$$n_{com} = \binom{3}{2} = \frac{6}{2} = 3.$$

This implies that in most cases 15 position estimates are obtained. This allows for an evaluation of the uncertainty of the measurement by calculating the standard deviations in  $x$ ,  $y$  and  $z$  direction using the singular value decomposition method.

## A.2 SYNCHRONIZATION OF THE VIDEO FRAMES

The first stage of the synchronisation consists of determining the first frame in which in each camera the LED is detected to switch on. All frames recorded prior to this frame are deleted from the records. The second stage is to compensate for the ‘rolling shutter effect’ as much as possible. To this end several options are available: (1) A method proposed by Smid & Matas (2017) relying on light flashes affecting the whole frame for all camera's (e.g. photo flashlights), (2) synchronization on phase differences, for this one has to assume the particle path is a perfect circle and (3) minimise the accuracy in the position by sub-frame shifts in time. The first method is very promising, the acquired footage however, contained no flashes that affect the whole frame for all cameras. The second method relies on a prior assumption on the path of the particle which is, principally, unknown. This might be solved by application of an iterative approach. However, this will be very computational demanding and therefore the last method mentioned was adopted. With respect to the sub-frame synchronisation, the iPhone 5s are leading, the read out is done line per line starting at the right of the sensor and finishing after 1/120 s at the left. This implies that in the most extreme case there might be a time shift of  $\sim 1/120$  s (one-time step) between cameras. Such a time shift results in a loss of accuracy of the end result.

Therefore, the following additional synchronisation algorithm was applied: for each experiment the position  $p_i(\tau)$  of the particle as observed by each camera was defined as a linear interpolation between two successive frames with unknown weight factors  $w_e$ :

$$p_i(\tau) = w_{e,i} \cdot p_i(t) + (1 - w_{e,i}) \cdot p_i(t - dt). \quad (\text{A.21})$$

The values for  $w_{e,i}$  ( $i = 1, \dots, 6$ ) were determined by minimising the sum of the standard deviations in the position of the particle in 3 dimensions by using the 15 estimates for the position obtained for each frame:

$$\bar{w}_{opt} = \min \left[ \sum_{i=1}^{i=3} \sigma_i \mid p_i, p_{i-1} \right]. \quad (\text{A.22})$$

The weight vector  $\bar{w}_{opt}$  was determined using the Levenberg-Marquart algorithm (Marquart, 1963). Overall, the remaining uncertainty (95% uncertainty interval: i.e. 3.92 standard deviations) in position in  $x$ ,  $y$  and  $z$ -direction obtained on moving particles is determined to be about 0.16 mm. The uncertainty varies with the position of the particle and is influenced by the presence/absence of reflections in the raw video footage. The accuracy in the time-dimension cannot be determined as a generic value for all frames, which is seen a serious drawback of the chosen solution.

# B

## STEREO PIV MEASURED VELOCITY PROFILES

In this appendix the stereo PIV measured free-surface vortex velocity profiles of  $V_\theta$ ,  $V_r$  and  $V_z$  are presented for series 1 to 7. The graphs include Burgers' profile of  $V_\theta$  (equation (3.19)) using the characteristic parameters  $\Gamma_\infty$  and  $r_c$ . The measured profiles are shown for measurements without the air core crossing a measurement plane only. Because of the different SPIV measurements post-processing methods,  $V_r$  and  $V_z$  are shown for  $0 < r < 0.04$  m and  $V_\theta$  is shown for  $0 < r < 0.10$  m.

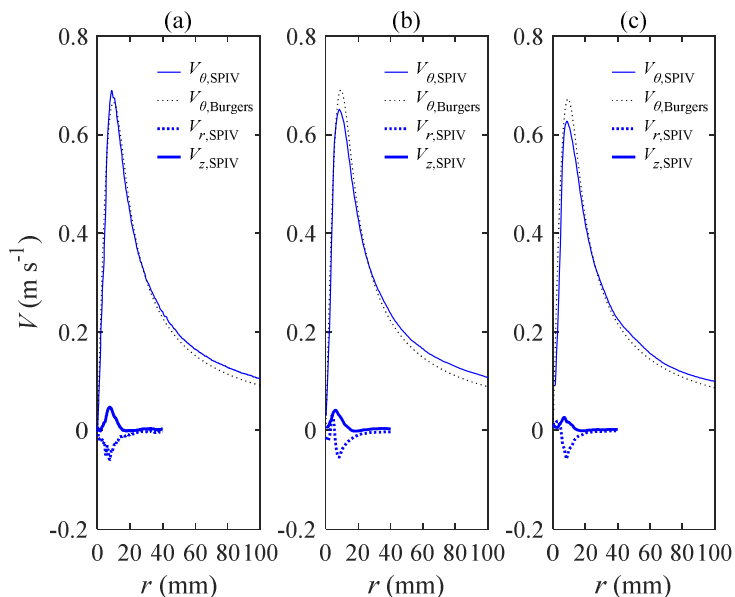


Figure B.1: Measured profiles of  $V_\theta$ ,  $V_r$  and  $V_z$  for series 1. (a) At plane 0.29 m. (b) At plane 0.49 m. (c) At plane 0.62 m.

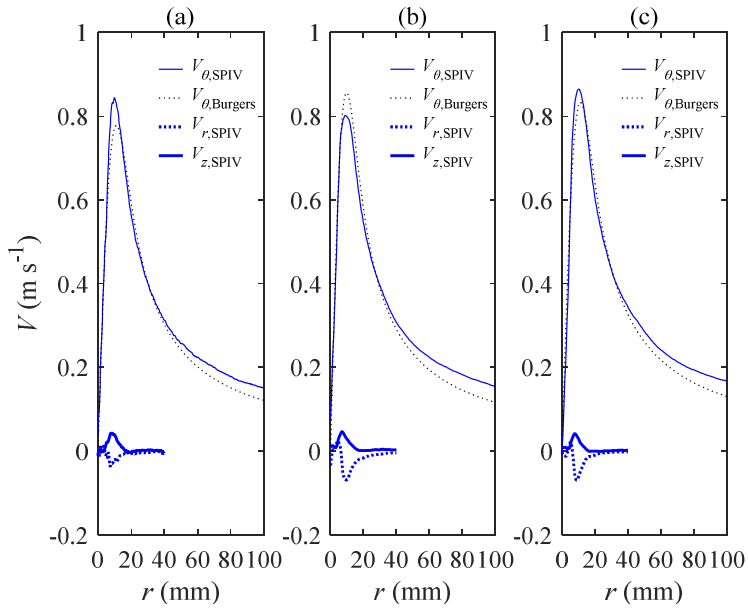


Figure B.2: Measured profiles of  $V_{\theta}$ ,  $V_r$  and  $V_z$  for series 2. (a) At plane 0.29 m. (b) At plane 0.49 m. (c) At plane 0.62 m.

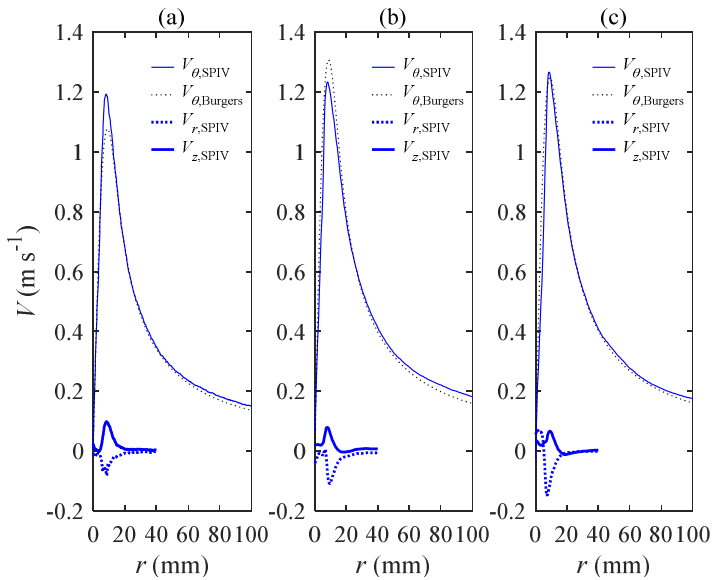


Figure B.3: Measured profiles of  $V_{\theta}$ ,  $V_r$  and  $V_z$  for series 3. (a) At plane 0.29 m (b) At plane 0.49 m (c) At plane 0.62 m.

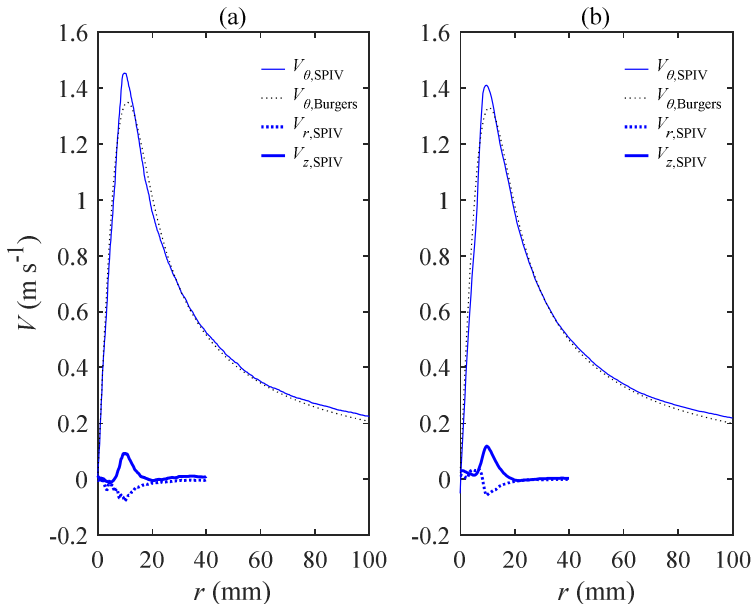


Figure B.4: Measured profiles of  $V_{\theta}$ ,  $V_r$  and  $V_z$  for series 4 (a) At plane 0.29 m. (b) At plane 0.49 m.

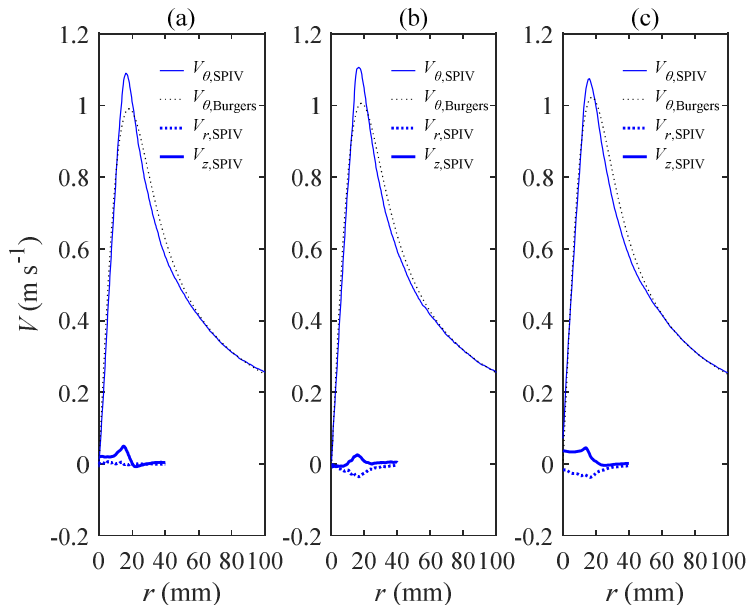


Figure B.5: Measured profiles of  $V_{\theta}$ ,  $V_r$  and  $V_z$  for series 5. (a) At plane 0.29 m. (b) At plane 0.49 m. (c) At plane 0.62 m.

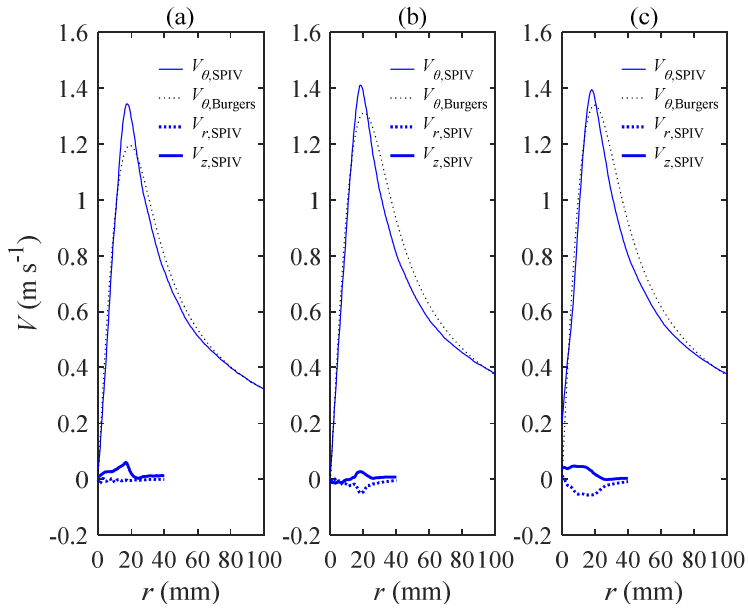


Figure B.6: Measured profiles of  $V_\theta$ ,  $V_r$  and  $V_z$  for series 6. (a) At plane 0.29 m. (b) At plane 0.49 m. (c) At plane 0.62 m.

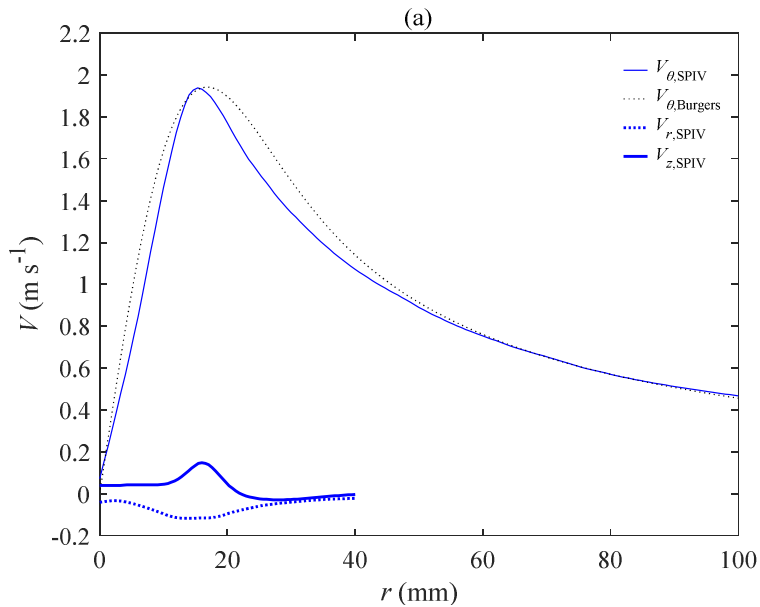


Figure B.7: Measured profiles of  $V_\theta$ ,  $V_r$  and  $V_z$  for series 7 at plane 0.29 m.

# C

## 2D-PTV PARTICLE MOTION RESULTS

In this appendix the 2D-PTV measured motion of the particles in the horizontal  $x, y$  plane are presented. As the goal of this appendix is to display the chaotic behavior of the particle motion, the motions of the spheres are showed only because the cubes and ellipsoids showed less chaotic behavior. The spheres are released at different positions indicated by the yellow dot.  $r_0$  is the distance between the vortex center and position of release. The characteristics of the particles are addressed in Table 2.3 The characteristics of the series (the hydraulic conditions) are addressed in Table 3.1.

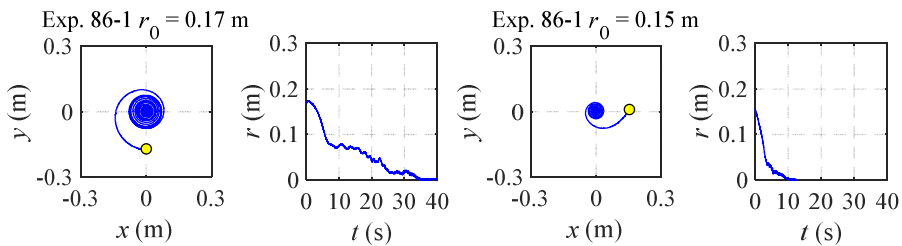


Figure C.1: 2D measured motion of sphere 86 at series 1.

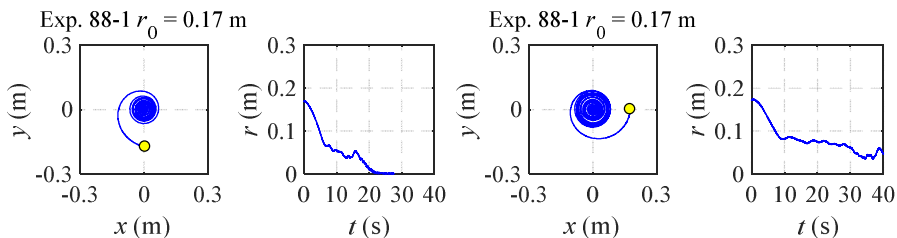


Figure C.2: 2D measured motion of sphere 88 at series 1.

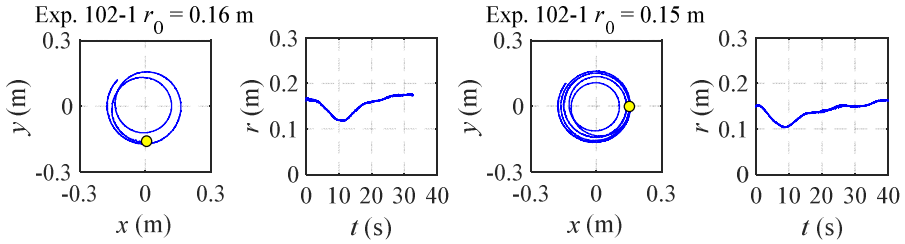


Figure C.3: 2D measured motion of sphere 102 at series 1.

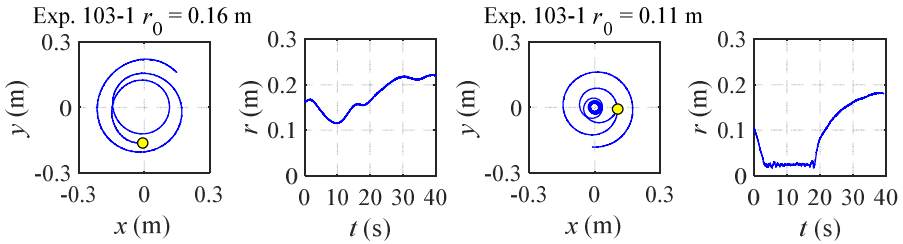


Figure C.4: 2D measured motion of sphere 103 at series 1.

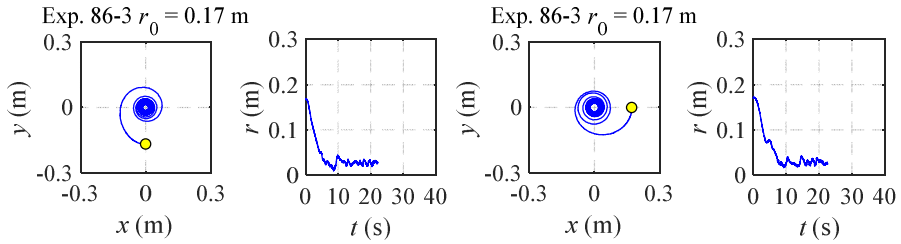


Figure C.5: 2D measured motion of sphere 86 at series 3.

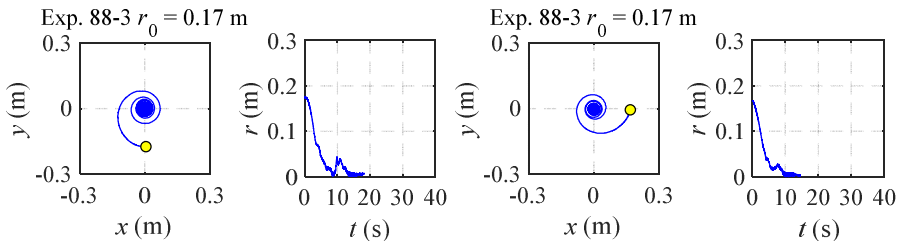


Figure C.6: 2D measured motion of sphere 88 at series 3.

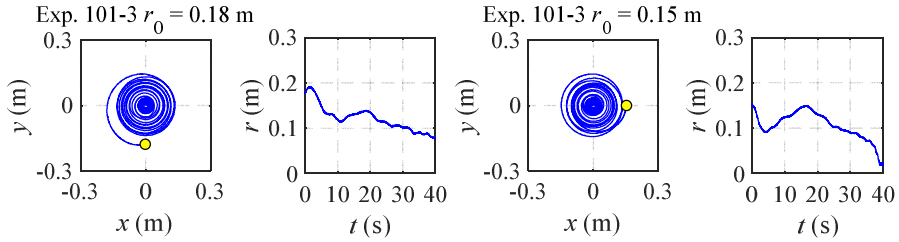


Figure C.7: 2D measured motion of sphere 101 at series 3.

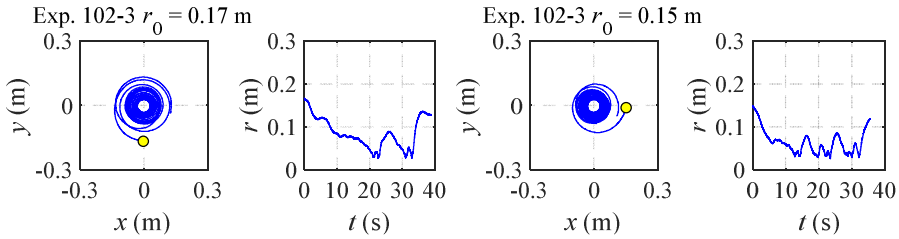


Figure C.8: 2D measured motion of sphere 102 at series 3.

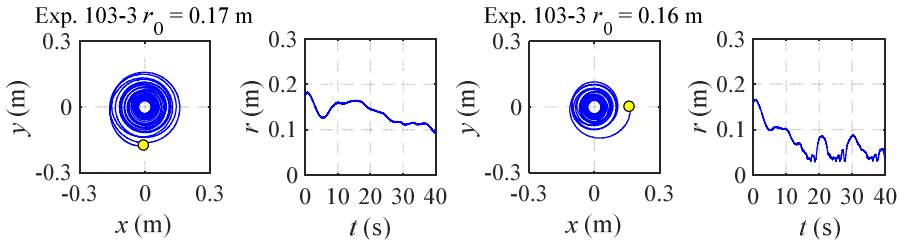


Figure C.9: 2D measured motion of sphere 103 at series 3.

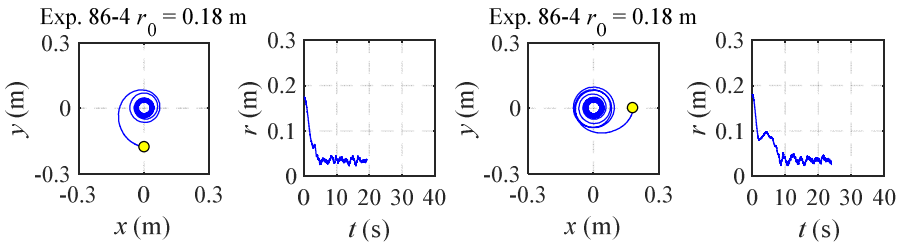


Figure C.10: 2D measured motion of sphere 86 at series 4.

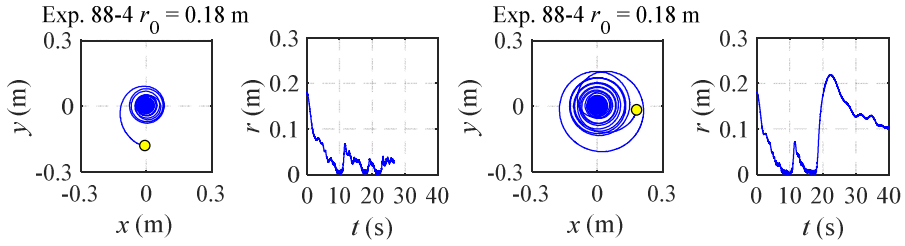


Figure C.11: 2D measured motion of sphere 88 at series 4.

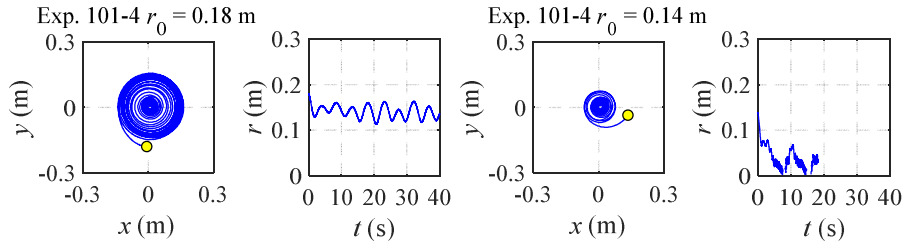


Figure C.12: 2D measured motion of sphere 101 at series 4.

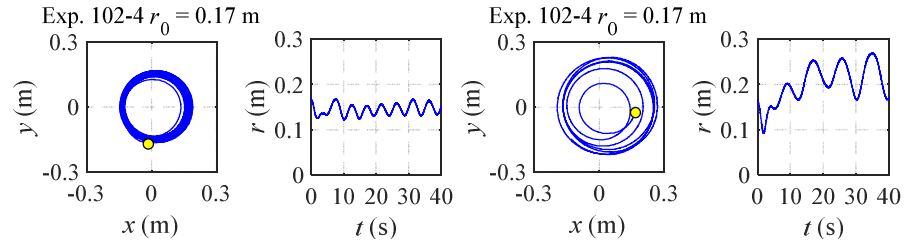


Figure C.13: 2D measured motion of sphere 102 at series 4.

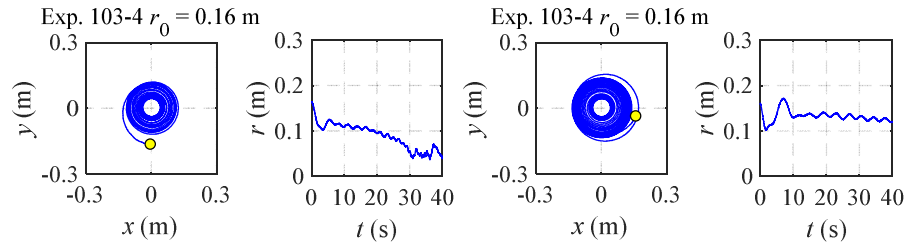


Figure C.14: 2D measured motion of sphere 103 at series 4.

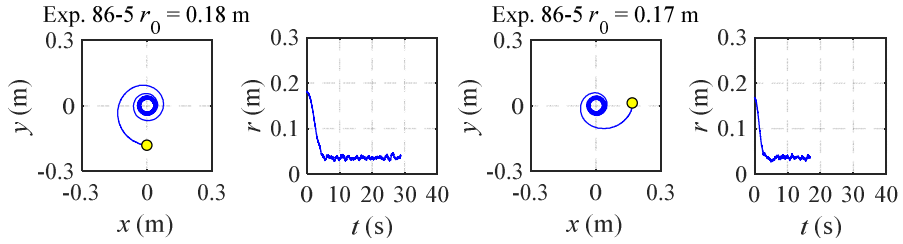


Figure C.15: 2D measured motion of sphere 86 at series 5.

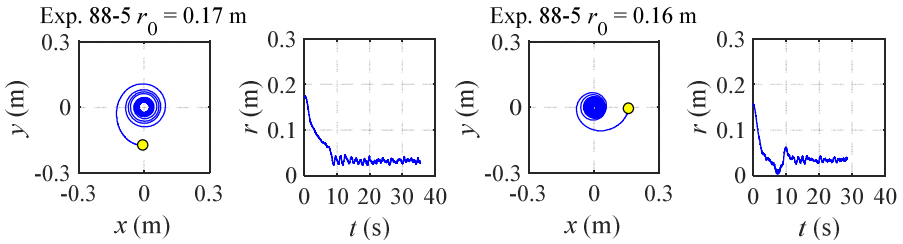


Figure C.16: 2D measured motion of sphere 88 at series 5.

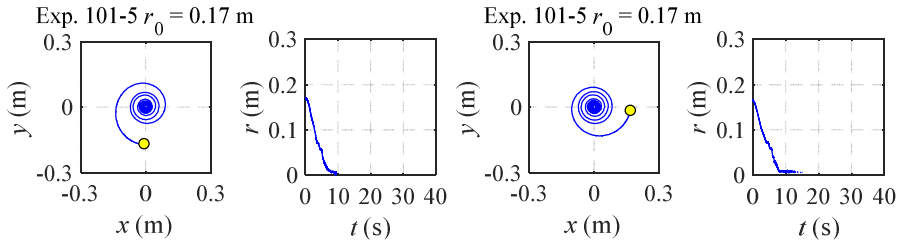


Figure C.17: 2D measured motion of sphere 101 at series 5.

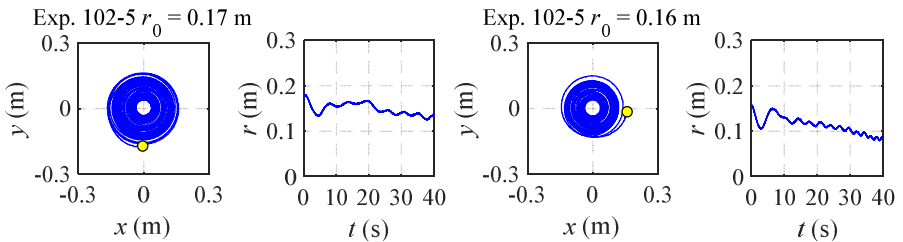


Figure C.18: 2D measured motion of sphere 102 at series 5.

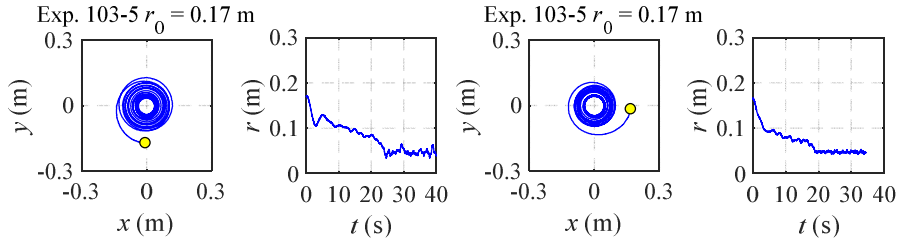


Figure C.19: 2D measured motion of sphere 103 at series 5.

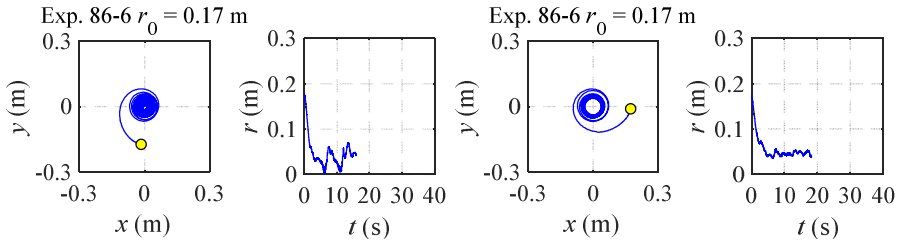


Figure C.20: 2D measured motion of sphere 86 at series 6.

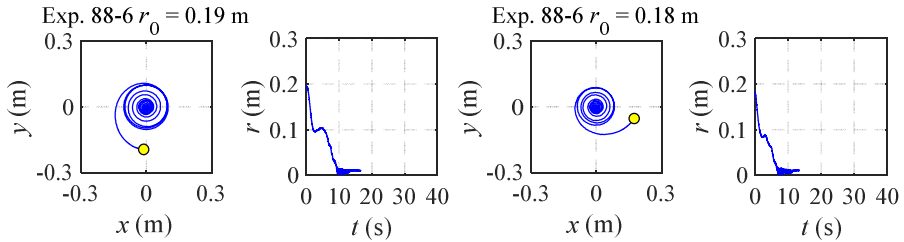


Figure C.21: 2D measured motion of sphere 88 at series 6.

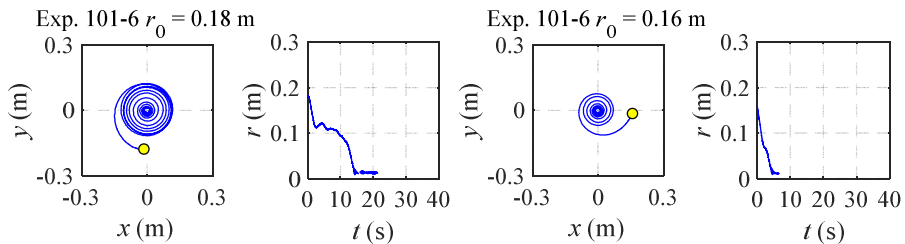


Figure C.22: 2D measured motion of sphere 101 at series 6.

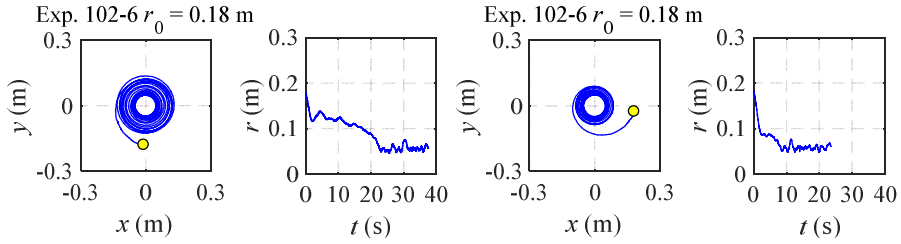


Figure C.23: 2D measured motion of sphere 102 at series 6.

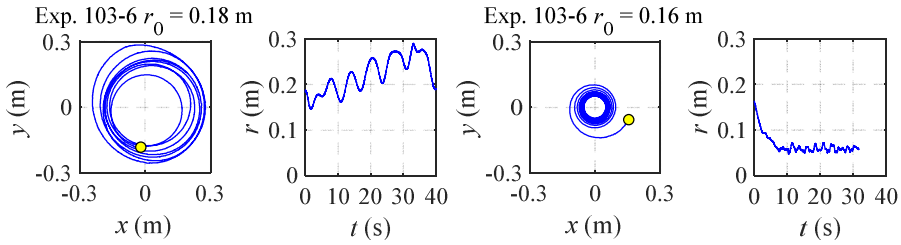


Figure C.24: 2D measured motion of sphere 103 at series 6.

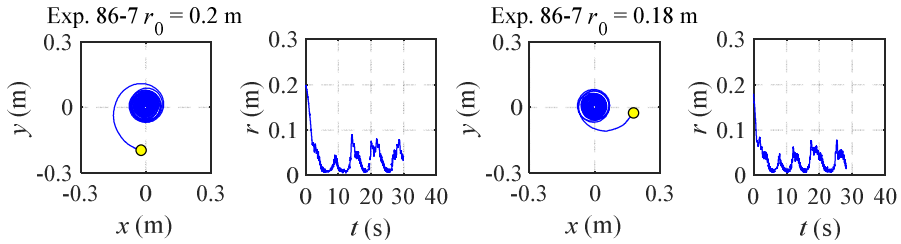


Figure C.25: 2D measured motion of sphere 86 at series 7.

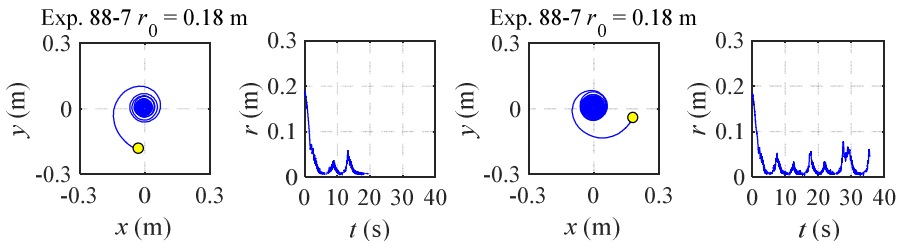


Figure C.26: 2D measured motion of sphere 88 at series 7.

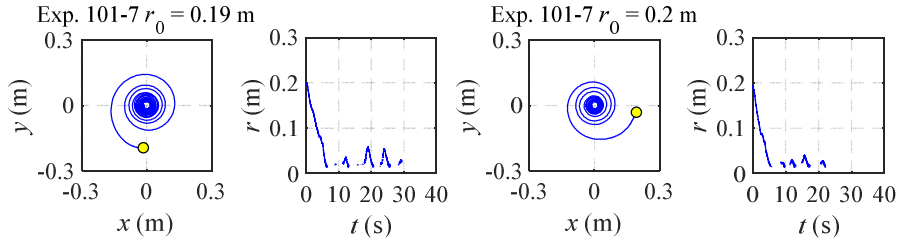


Figure C.27: 2D measured motion of sphere 101 at series 7.

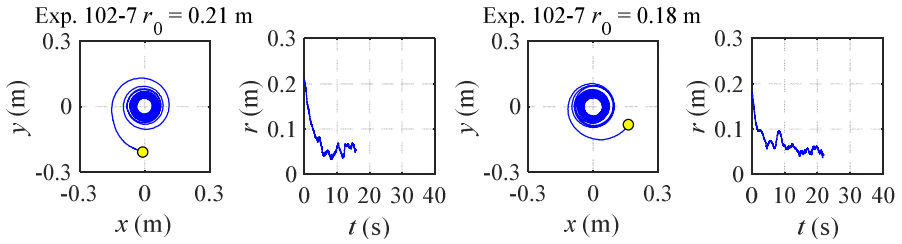


Figure C.28: 2D measured motion of sphere 102 at series 7.

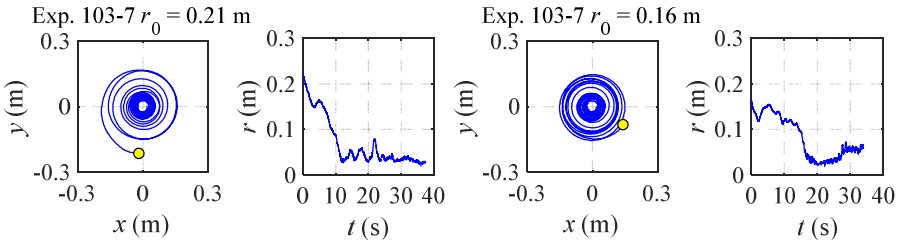


Figure C.29: 2D measured motion of sphere 103 at series 7.

# D

## 3D-PTV PARTICLE MOTION RESULTS

In this appendix the 3D-PTV measured axial motion of the particles along the air core and through the vortex core are showed. Each experiment is repeated 5 times (sub-exp. 1 to 5) to check the consistency of the results. Only sub-exp. 1 to 4 are listed in this appendix. For few experiments there are no results listed or the results of 2 to 3 sub-experiments are listed. This is due to some failures in the post processing of the experiments. The initial position of the particles is at the free-surface at a height of  $z \approx 0.90$  m.

### D.1 MEASURED AXIAL MOTION OF THE SPHERES

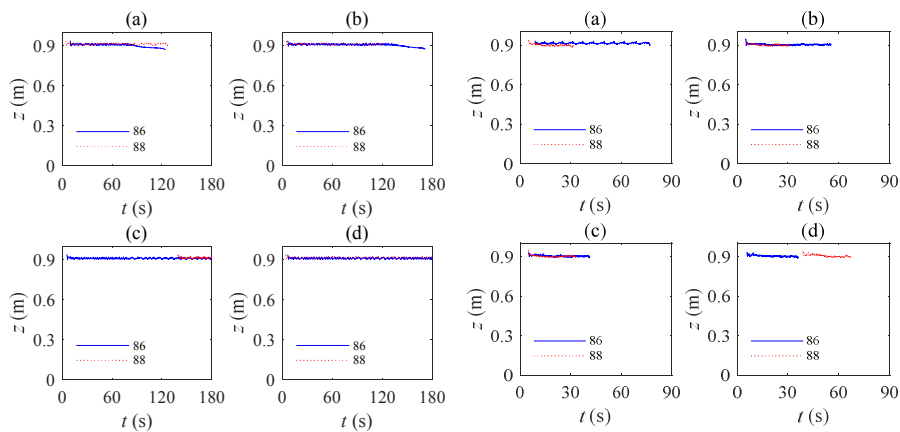


Figure D.1: Measured axial motion of spheres 86 and 88 for series 1. (a)-(d) Results of sub-exp. 1 to 4.

Figure D.2: Measured axial motion of spheres 86 and 88 for series 4. (a)-(d) Results of sub-exp. 1 to 4.

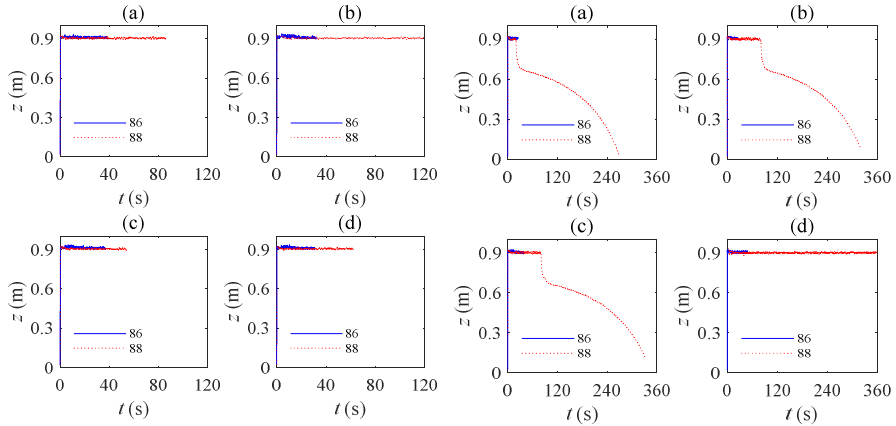


Figure D.3: Measured axial motion of spheres 86 and 88 for series 5. (a)-(d) Results of sub-exp. 1 to 4.

Figure D.4: Measured axial motion of spheres 86 and 88 for series 6. (a)-(d) Results of sub-exp. 1 to 4.

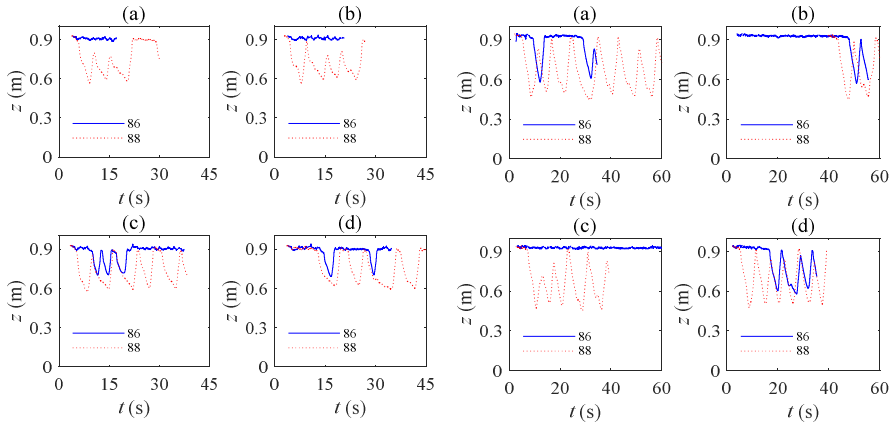


Figure D.5: Measured axial motion of spheres 86 and 88 for series 7. (a)-(d) Results of sub-exp. 1 to 4.

Figure D.6: Measured axial motion of spheres 86 and 88 for series 8. (a)-(d) Results for sub-exp. 1 to 4.

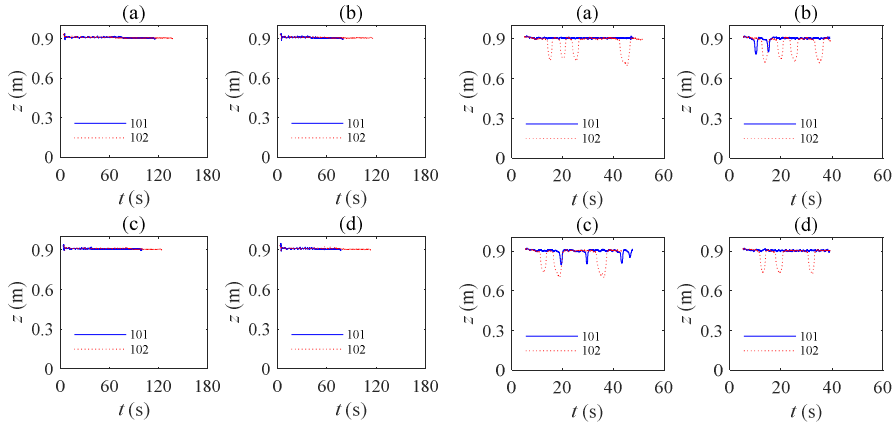


Figure D.7: Measured axial motion of spheres 101 and 102 for series 1. (a)-(d) Results of sub-exp. 1 to 4.

Figure D.8: Measured axial motion of spheres 101 and 102 for series 4. (a)-(d) Results of sub-exp. 1 to 4.

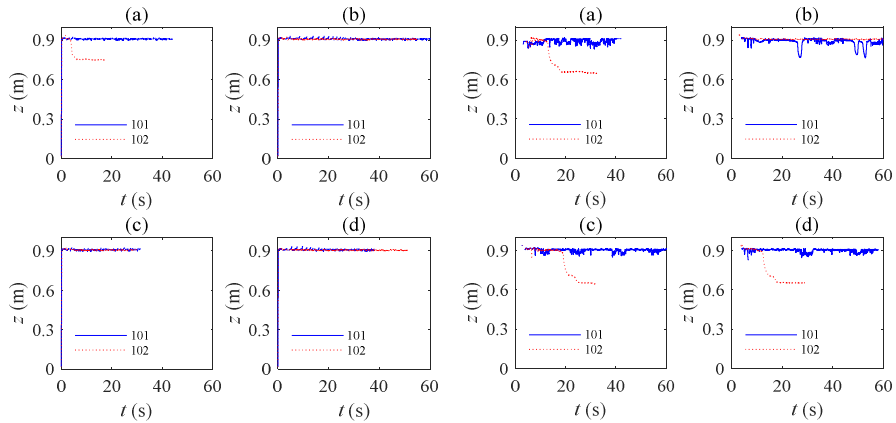


Figure D.9: Measured axial motion of spheres 101 and 102 for series 5. (a)-(d) Results of sub-exp. 1 to 4.

Figure D.10: Measured axial motion of spheres 101 and 102 for series 6. (a)-(d) Results of sub-exp. 1 to 4.

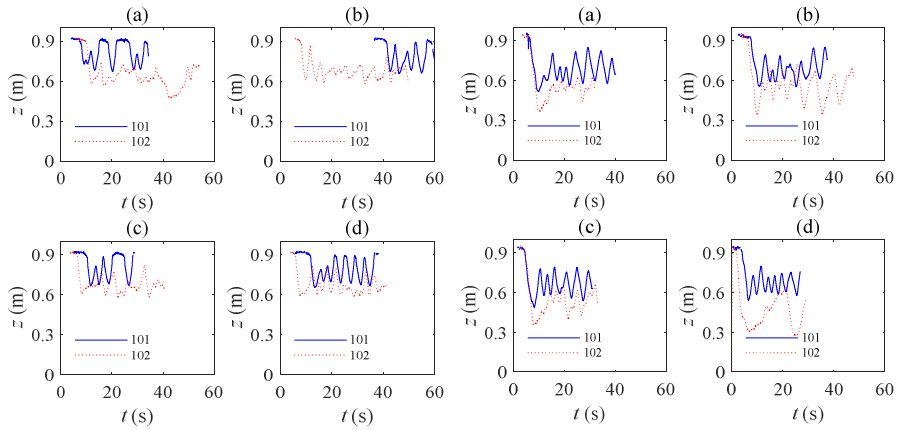


Figure D.11: Measured axial motion of spheres 101 and 102 for series 7. (a)-(d) Results of the sub-exp. 1 to 4.

Figure D.12: Measured axial motion of spheres 101 and 102 for series 8. (a)-(d) Results of sub-exp. 1 to 4.

## D.2 MEASURED AXIAL MOTION OF THE CUBES

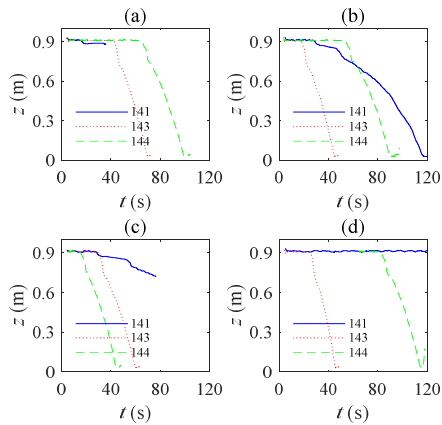


Figure D.13: Measured axial motion of cubes 141, 143 and 144 for series 1. (a)-(d) Results of sub-exp. 1 to 4.

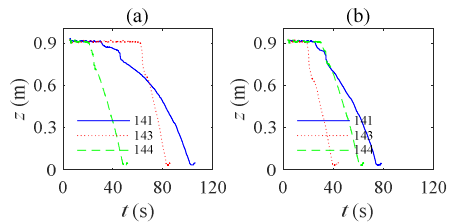


Figure D.14: Measured axial motion of cubes 141, 143 and 144 for series 2. (a)-(b) Results of sub-exp. 1 to 2.

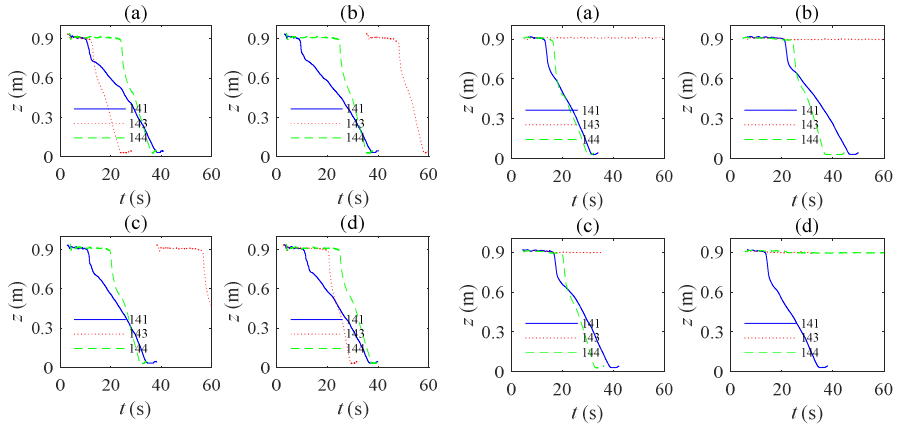


Figure D.15: Measured axial motion of cubes 141, 143 and 144 for series 3. (a)-(d) Results of sub-exp. 1 to 4.

Figure D.16: Measured axial motion of cubes 141, 143 and 144 for series 4. (a)-(d) Results of sub-exp. 1 to 4.

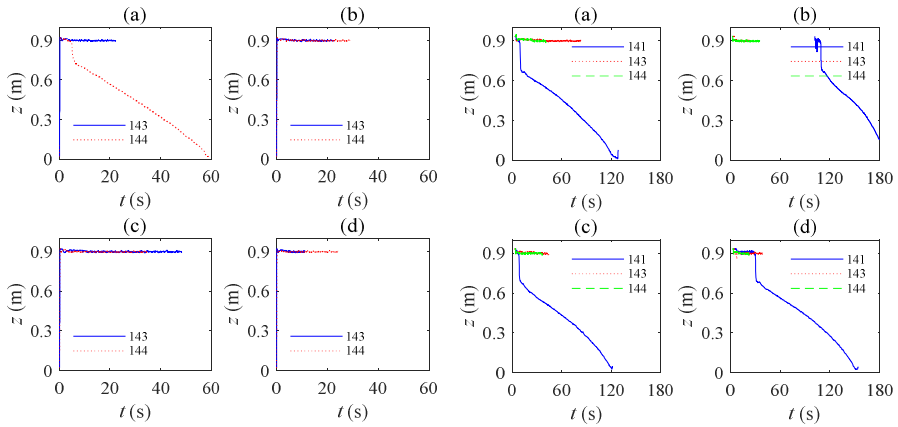


Figure D.17: Measured axial motion of cubes 143 and 144 for series 5. (a)-(d) Results of sub-exp. 1 to 4.

Figure D.18: Measured axial motion of cubes 141, 143 and 144 for series 6. (a)-(d) Results of the sub-experiments 1 to 4.

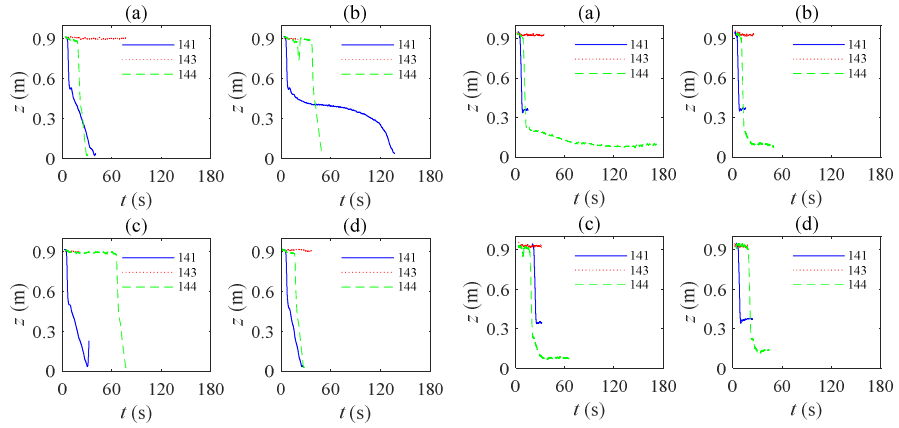


Figure D.19: Measured axial motion of cubes 141, 143 and 144 for series 7. (a)-(d) Results of the sub-experiments 1 to 4.

Figure D.20: Measured axial motion of cubes 141, 143 and 144 for series 8. (a)-(d) Results of the sub-experiments 1 to 4.

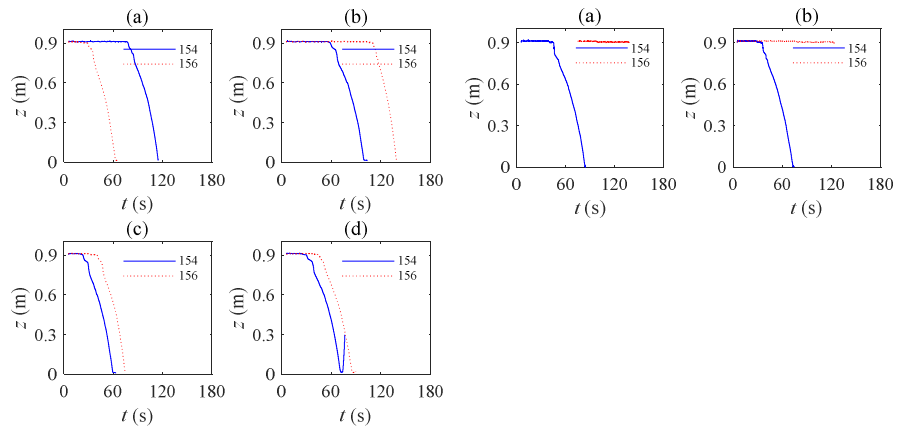


Figure D.21: Measured axial motion of cubes 154 and 156 for series 1. (a)-(d) Results of the sub-experiments 1 to 4.

Figure D.22: Measured axial motion of cubes 153, 154 and 156 for series 2. (a)-(b) Results of the sub-experiments 1 to 2.

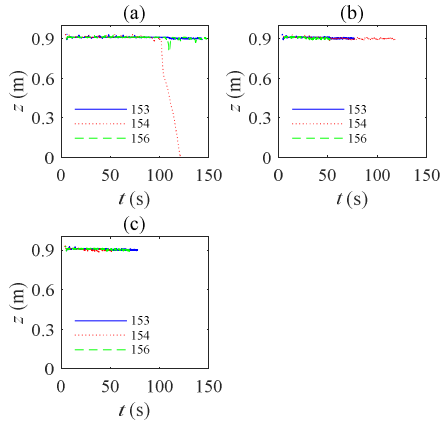


Figure D.23: Measured axial motion of cubes 153, 154 and 156 for series 3. (a)-(d) Results of the sub-experiments 1 to 3.

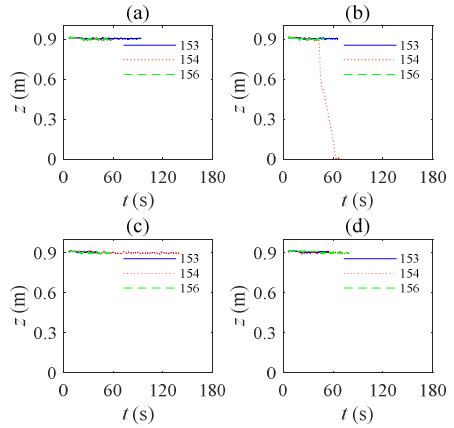


Figure D.24: Measured axial motion of cubes 153, 154 and 156 for series 4. (a)-(d) Results of the sub-experiments 1 to 4.

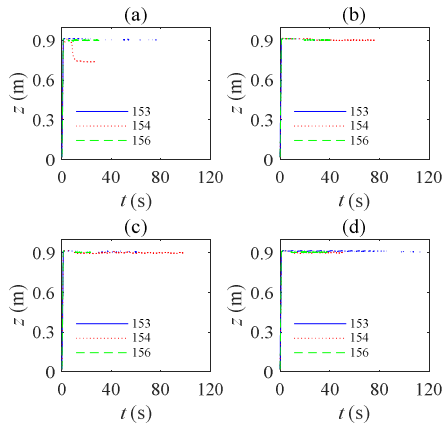


Figure D.25: Measured axial motion of cubes 153, 154 and 156 for series 5. (a)-(d) Results of the sub-experiments 1 to 4.

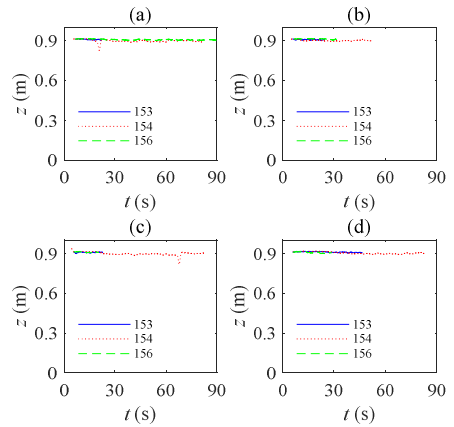


Figure D.26: Measured axial motion of cubes 153, 154 and 156 for series 6. (a)-(d) Results of the sub-experiments 1 to 4.

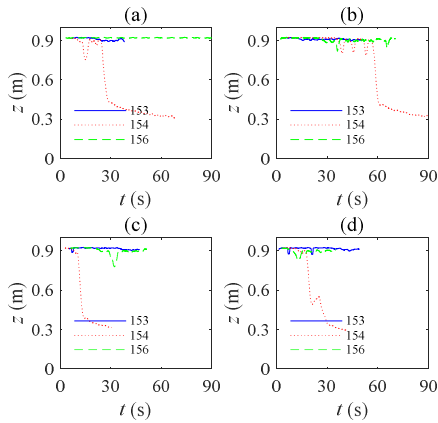


Figure D.27: Measured axial motion of cubes 153, 154 and 156 for series 7. (a)-(d) Results of the sub-experiments 1 to 4.

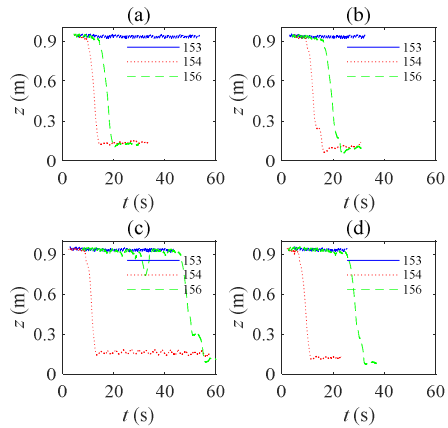


Figure D.28: Measured axial motion of cubes 153, 154 and 156 for series 8. (a)-(d) Results of the sub-experiments 1 to 4.

### D.3 MEASURED AXIAL MOTION OF THE ELLIPSOIDS

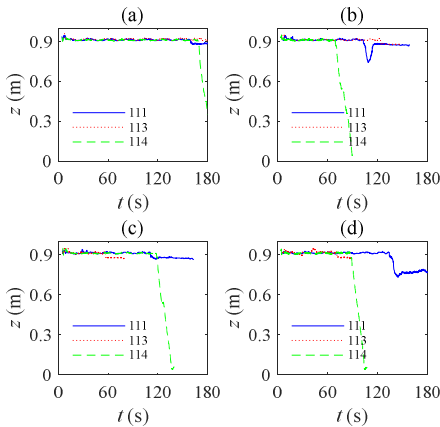


Figure D.29: Measured axial motion of ellipsoids 111, 113 and 114 for series 1. (a)-(d) Results of the sub-experiments 1 to 4.

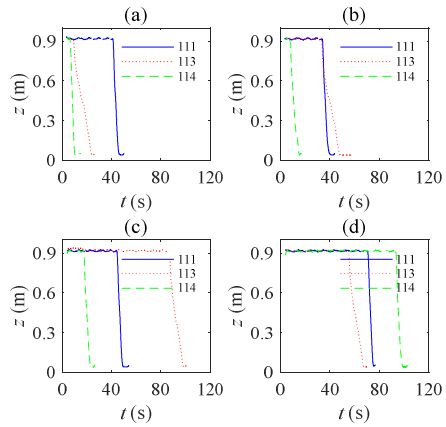


Figure D.30: Measured axial motion of ellipsoids 111, 113 and 114 for series 4. (a)-(d) Results of the sub-experiments 1 to 4.

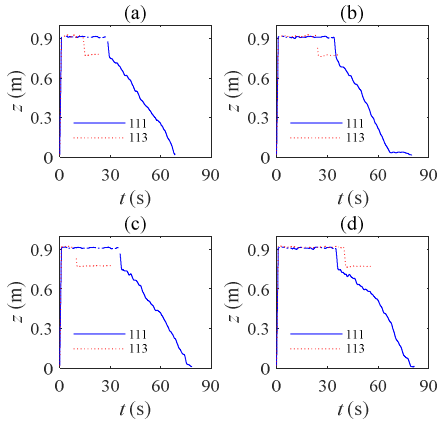


Figure D.31: Measured axial motion of ellipsoids 111 and 113 for series 5. (a)-(d) Results of the sub-experiments 1 to 4.

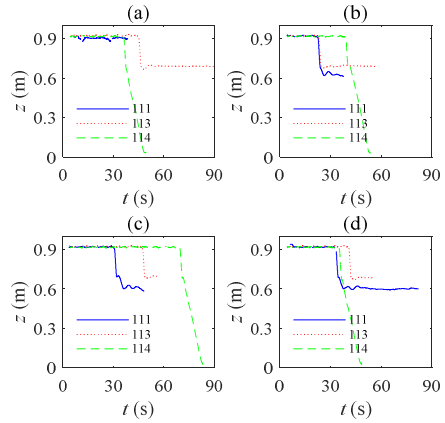


Figure D.32: Measured axial motion of ellipsoids 111, 113 and 114 for series 6. (a)-(d) Results of the sub-experiments 1 to 4.

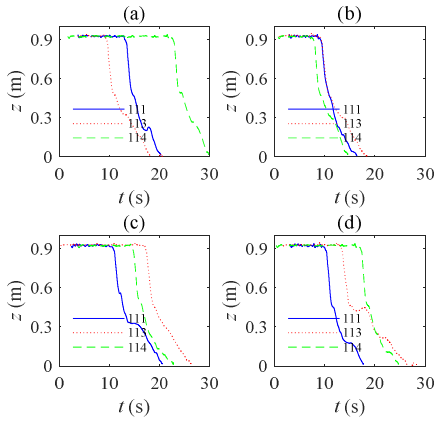


Figure D.33: Measured axial motion of ellipsoids 111, 113 and 114 for series 7. (a)-(d) Results of the sub-experiments 1 to 4.

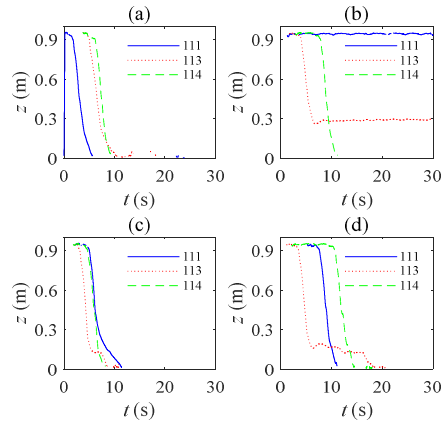


Figure D.34: Measured axial motion of ellipsoids 111, 113 and 114 for series 8. (a)-(d) Results of the sub-experiments 1 to 4.

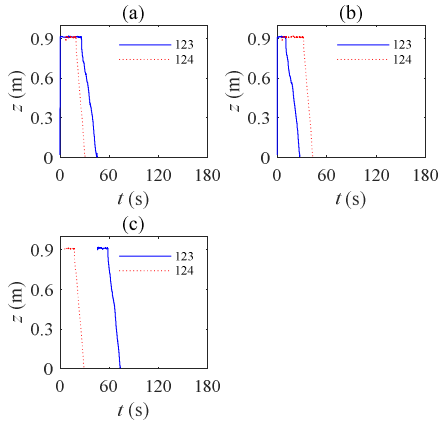


Figure D.35: Measured axial motion of ellipsoids 123 and 124 for series 2. (a)-(c) Results of the sub-experiments 1 to 3.

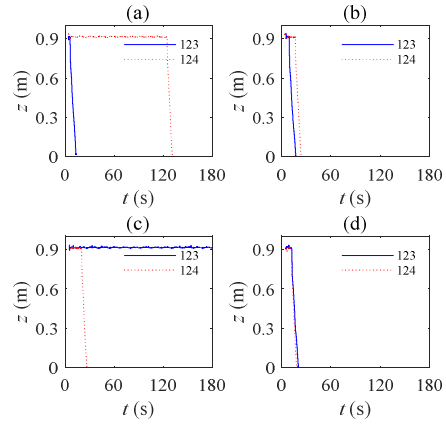


Figure D.36: Measured axial motion of ellipsoids 123 and 124 for series 3. (a)-(d) Results of the sub-experiments 1 to 4.

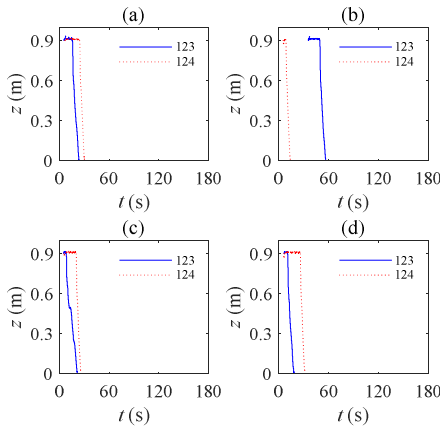


Figure D.37: Measured axial motion of ellipsoids 123 and 124 for series 4. (a)-(d) Results of the sub-experiments 1 to 4.

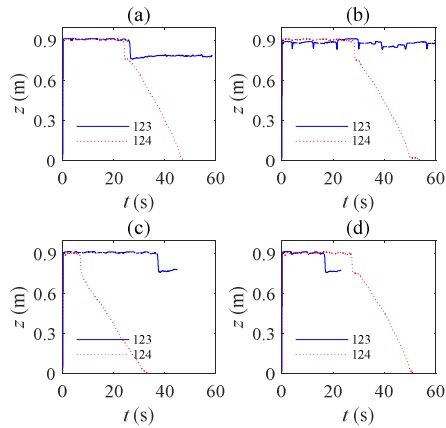


Figure D.38: Measured axial motion of ellipsoids 123 and 124 for series 5. (a)-(d) Results of the sub-experiments 1 to 4.

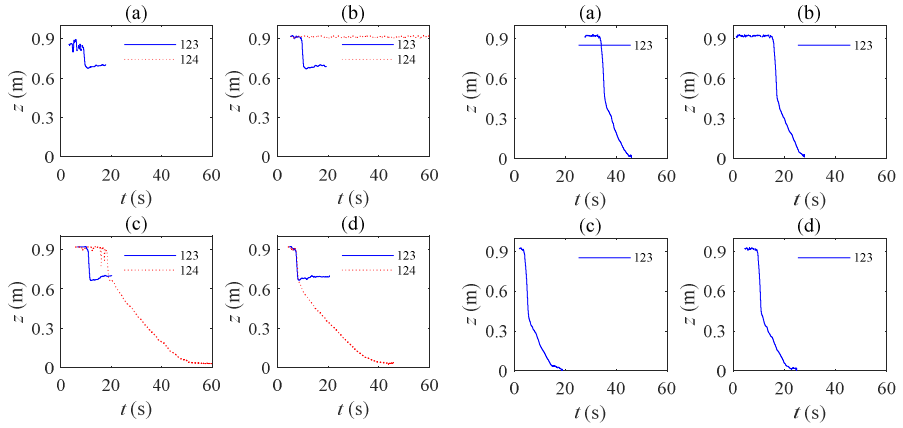


Figure D.39: Measured axial motion of ellipsoids 123 and 124 for series 6. (a)-(d) Results of the sub-experiments 1 to 4.

Figure D.40: Measured axial motion of ellipsoids 123 for series 7. (a)-(d) Results of the sub-experiments 1 to 4.

## D.4 EXPERIMENTAL DATA-SET FOR VALIDATION OF THE STAGE 2 MOTION CONDITION

Table D.1: Executed experiments for the spheres and cubes.

Particle	Series						
	1	2	3	4	5	6	7
71			•		•	•	
83	•		•		•		
84	•					•	
86	•		•		•	•	•
88			•		•	•	•
91	•				•	•	
92	•		•		•	•	•
101	•				•	•	
102	•				•	•	
103			•		•	•	
141	•	•	•	•	•	•	•
143	•	•	•		•		
144	•	•	•	•	•	•	•
151						•	
153	•				•	•	
154	•	•	•	•	•	•	•
156	•				•		

Table D.2: Executed experiments for the ellipsoids.

Particle	Series						
	1	2	3	4	5	6	7
111	•	•	•	•	•	•	•
113				•	•	•	•
114	•	•	•	•	•	•	•
123	•	•	•	•	•	•	•
124	•	•	•	•	•	•	

# E

## EQUATIONS FOR THE 2D MOTION OF SPHERICAL PARTICLES

The equation of motion for a sphere with volume  $\chi$  at Reynolds number in the order of  $10^3$  to  $10^5$  moving with velocity  $\mathbf{V}$  through an ambient non-uniform flow with velocity  $\mathbf{U}$  is expressed by:

$$\begin{aligned} (\rho_p + C_A \rho_f) \chi \frac{D\mathbf{U}}{Dt} = \rho_f (1 + C_A) \chi \frac{D\mathbf{V}}{Dt} + \chi (\rho_f - \rho_p) \mathbf{g} + \\ 0.5 \rho_f C_D A_N (\mathbf{V} - \mathbf{U}) (|\mathbf{V} - \mathbf{U}|) + \rho_f \chi C_L (\mathbf{V} - \mathbf{U}) \times \boldsymbol{\omega} + 2 \rho_f \chi (\mathbf{V} - \mathbf{U}) \boldsymbol{\Omega}_p \end{aligned} \quad (\text{E.1})$$

By describing the motion in Cartesian coordinates, for a steady flow and by neglecting the velocity gradients of  $V_x$  and  $V_y$  in axial direction, the equation of motion in  $x$  and  $y$  direction is then:

$$\begin{aligned} \frac{dU_x}{dt} = \left( \frac{\chi_s \rho_f (1 + C_A)}{\chi \rho_p + \chi_s C_A \rho_f} \right) \left( V_x \frac{\partial V_x}{\partial x} + V_y \frac{\partial V_x}{\partial y} \right) + \\ \left( \frac{0.5 \rho_f C_D A_N}{\chi \rho_p + \chi_s C_A \rho_f} \right) \left[ (V_x - U_x)^2 + (V_y - U_y)^2 \right] \cos(\theta) + \\ \left( \frac{\rho_f \chi}{\chi \rho_p + \chi_s C_A \rho_f} \right) \left( \sqrt{(V_x - U_x)^2 + (V_y - U_y)^2} \right) \cos\left(\theta + \frac{1}{2}\pi\right) (2\Omega_{p,z} + C_L \omega_z) \end{aligned} \quad (\text{E.2})$$

$$\begin{aligned}
\frac{dU_y}{dt} &= \left( \frac{\chi_s \rho_f (1+C_A)}{\chi \rho_p + \chi_s C_A \rho_f} \right) \left( V_x \frac{\partial V_y}{\partial x} + V_y \frac{\partial V_y}{\partial y} \right) + \\
&\left( \frac{0.5 \rho_f C_D A_N}{\chi \rho_p + \chi_s C_A \rho_f} \right) \left[ (V_x - U_x)^2 + (V_y - U_y)^2 \right] \sin(\theta) + \\
&\left( \frac{\rho_f \chi}{\chi \rho_p + \chi_s C_A \rho_f} \right) \left( \sqrt{(V_x - U_x)^2 + (V_y - U_y)^2} \right) \sin\left(\theta + \frac{1}{2}\pi\right) (2\Omega_{p,z} + C_L \omega_z)
\end{aligned} \tag{E.3}$$

where  $\chi_s$  is the submerged volume of the sphere. The angle  $\theta$  is determined by the relative velocity components:

$$\theta = \begin{cases} \tan^{-1}\left(\frac{V_y - U_y}{V_x - U_x}\right) & \text{if } V_x - U_x > 0 \\ \tan^{-1}\left(\frac{V_y - U_y}{V_x - U_x}\right) + \pi & \text{if } V_x - U_x < 0. \end{cases} \tag{E.4}$$

The values of  $\mathbf{V}$  at the sphere's center are derived from the Burgers vortex model for the undisturbed tangential fluid velocity  $V_\theta$ :

$$V_\theta = \frac{\Gamma}{2\pi r} \left[ 1 - \exp\left(-\frac{r^2}{r_c^2}\right) \right] \tag{E.5}$$

and by applying the  $x, y$  coordinates to express  $r$ , the velocities become a function of the independent variables  $x, y, \Gamma$ , and  $r_c$ :

$$\begin{aligned}
x > 0 &\begin{cases} V_x = \frac{\Gamma_\infty}{2\pi\sqrt{x^2 + y^2}} \left[ 1 - \exp\left(-\frac{x^2 + y^2}{r_c^2}\right) \right] \cos\left(\varphi - \frac{\pi}{2}\right) \\ V_y = \frac{\Gamma_\infty}{2\pi\sqrt{x^2 + y^2}} \left[ 1 - \exp\left(-\frac{x^2 + y^2}{r_c^2}\right) \right] \sin\left(\varphi - \frac{\pi}{2}\right) \end{cases} \\
x < 0 &\begin{cases} V_x = \frac{\Gamma_\infty}{2\pi\sqrt{x^2 + y^2}} \left[ 1 - \exp\left(-\frac{x^2 + y^2}{r_c^2}\right) \right] \cos\left(\varphi + \frac{\pi}{2}\right) \\ V_y = \frac{\Gamma_\infty}{2\pi\sqrt{x^2 + y^2}} \left[ 1 - \exp\left(-\frac{x^2 + y^2}{r_c^2}\right) \right] \sin\left(\varphi + \frac{\pi}{2}\right) \end{cases}
\end{aligned} \tag{E.6}$$

where:

$$\varphi = \begin{cases} \tan^{-1}\left(\frac{y}{x}\right) & \text{if } x \geq 0 \\ \tan^{-1}\left(\frac{y}{x}\right) + \pi & \text{if } x < 0 \end{cases} \quad (\text{E.7})$$

consequently, the spatial derivatives of  $\mathbf{V}$  are (only showed for  $x > 0$ ):

$$\begin{aligned} \frac{\partial V_x}{\partial x} &= \frac{x\Gamma_\infty \cos(\varphi + \frac{\pi}{2})}{2\pi r^3} \left( \exp\left[-\left(\frac{r}{r_c}\right)^2\right] - 1 \right) + \frac{x\Gamma_\infty \cos(\varphi + \frac{\pi}{2})}{\pi r_c^2 r} \left( \exp\left[-\left(\frac{r}{r_c}\right)^2\right] \right) - \\ &\quad \frac{y\Gamma_\infty \sin(\varphi + \frac{\pi}{2})}{2\pi r y^2 \left(\frac{Y^2}{X^2} + 1\right)} \left( \exp\left[-\left(\frac{r}{r_c}\right)^2\right] - 1 \right) \\ \frac{\partial V_x}{\partial y} &= \frac{y\Gamma_\infty \cos(\varphi + \frac{\pi}{2})}{2\pi r^3} \left( \exp\left[-\left(\frac{r}{r_c}\right)^2\right] - 1 \right) + \frac{y\Gamma_\infty \cos(\varphi + \frac{\pi}{2})}{\pi r_c^2 r} \left( \exp\left[-\left(\frac{r}{r_c}\right)^2\right] \right) + \\ &\quad \frac{\Gamma_\infty \sin(\varphi + \frac{\pi}{2})}{2\pi r x \left(\frac{y^2}{x^2} + 1\right)} \left( \exp\left[-\left(\frac{r}{r_c}\right)^2\right] - 1 \right) \\ \frac{\partial V_y}{\partial x} &= \frac{x\Gamma_\infty \sin(\varphi + \frac{\pi}{2})}{2\pi r^3} \left( \exp\left[-\left(\frac{r}{r_c}\right)^2\right] - 1 \right) + \frac{x\Gamma_\infty \sin(\varphi + \frac{\pi}{2})}{\pi r_c^2 r} \left( \exp\left[-\left(\frac{r}{r_c}\right)^2\right] \right) + \\ &\quad \frac{y\Gamma_\infty \cos(\varphi + \frac{\pi}{2})}{2\pi r y^2 \left(\frac{Y^2}{X^2} + 1\right)} \left( \exp\left[-\left(\frac{r}{r_c}\right)^2\right] - 1 \right) \\ \frac{\partial V_y}{\partial y} &= \frac{y\Gamma_\infty \sin(\varphi + \frac{\pi}{2})}{2\pi r^3} \left( \exp\left[-\left(\frac{r}{r_c}\right)^2\right] - 1 \right) + \frac{y\Gamma_\infty \sin(\varphi + \frac{\pi}{2})}{\pi r_c^2 r} \left( \exp\left[-\left(\frac{r}{r_c}\right)^2\right] \right) - \\ &\quad \frac{\Gamma_\infty \cos(\varphi + \frac{\pi}{2})}{2\pi r x \left(\frac{y^2}{x^2} + 1\right)} \left( \exp\left[-\left(\frac{r}{r_c}\right)^2\right] - 1 \right). \end{aligned} \quad (\text{E.8})$$



# F

## COMPARISON OF PHYSICAL RESULTS WITH CFD RESULTS

### F.1 CASE 1: THE BREDA TEST FACILITY PUMP SUMP

#### DESCRIPTION OF THE PUMP SUMP

The concrete sump has a rectangular geometry of  $1.5 \times 1.5$  m and the height is 3.3 m, see Figure F.1. The sump bottom is flat without fillets or flow regulating measures like splitters or cones. The sump is connected by a  $\text{\O}600$  mm concrete inlet to an upstream reservoir of  $3.0 \times 3.0$  m. The sump has a submersible pump type Flygt 3153.181-412 that operates at flow rates between 50 and  $400 \text{ m}^3 \text{ h}^{-1}$ . The pump discharges into the reservoir so the set-up acts as a loop providing a constant water depth. The flow rate is controlled by a combination of a frequency converter and control valve and measured with a Krohne Aquaflux F DN300 flow meter. The horizontal water surface movement is recorded with a D-link DCS-2310L camera that is placed at the top of the sump. When a stable vortex was present, camera snapshots were made of the water surface. To provide realistic flow conditions as in real WWPS's, the water depth was set to  $\sim 0.93$  m to obtain a jet-shaped inflow from the circular inlet. At a flow rate of  $275 \text{ m}^3 \text{ h}^{-1}$  the test facility showed a free-surface vortex with a strength of 4 to 6 (see Figure 1.6 for the strength definition). Figure F.3(a) shows a snapshot of the free-surface vortex. The vortex showed some horizontal displacement. The presence of the vortex was accompanied by a gulping sound due to the entrainment of air by the suction inlet and thus the vortex had a full air core.

#### THE CFD MODEL AND BOUNDARY CONDITIONS

The model uses a single-phase approach and consists of a hexahedral mesh with 1.2 million cells, see Figure F.2(b). The model uses the Reynolds-Averaged Navier-Stokes (RANS) turbulence model. Both a  $k\text{-}\epsilon$  and  $k\text{-}\Omega$  model was used providing the

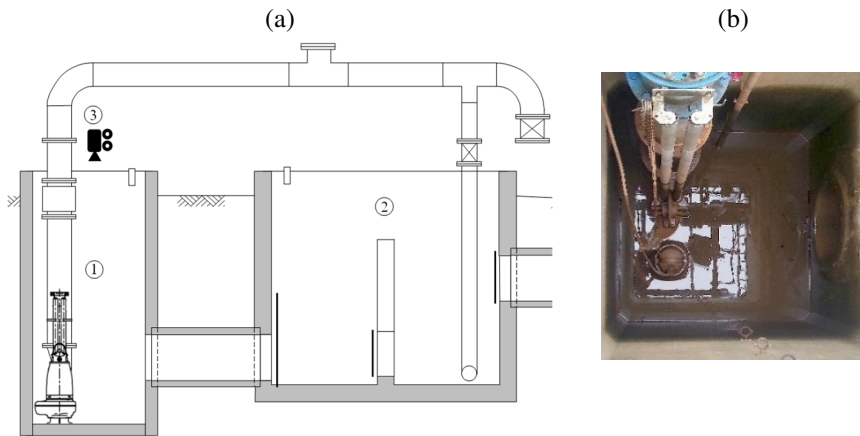


Figure F.1: (a) Schematic side view of the Breda test facility with (1) the pump sump and submerged pump (2) the upstream reservoir and (3) the camera. (a) Top view of the pump sump reservoir.

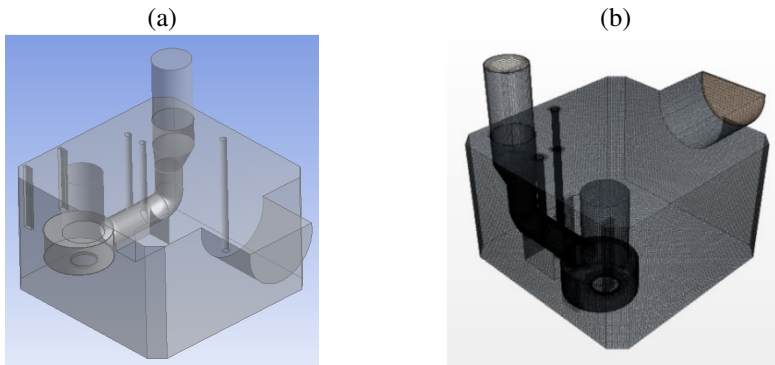


Figure F.2: (a) CFD model of the Breda test facility pump sump. (b) Model mesh of pump sump. The model includes the circular inlet, the submersible pump and discharge line.

same results. The boundary condition comprises a pressure boundary at the inlet conduit and a mass outflow at the pump pressure line. The constant flow rate and water depth is set to  $275 \text{ m}^3 \text{ h}^{-1}$  and  $0.93 \text{ m}$ . The top side of the model represents a fixed water free-surface where a slip condition is applied and thus a non-zero tangential fluid velocity.

#### QUALITATIVE COMPARISON OF PHYSICAL RESULTS WITH CFD RESULTS

Figure F.3 shows the physical results versus the CFD simulation results. The CFD results show a clear flow circulation in the same region as in the test facility. The axis of this circulation can be seen as a location of the vortex core. This is also indicated

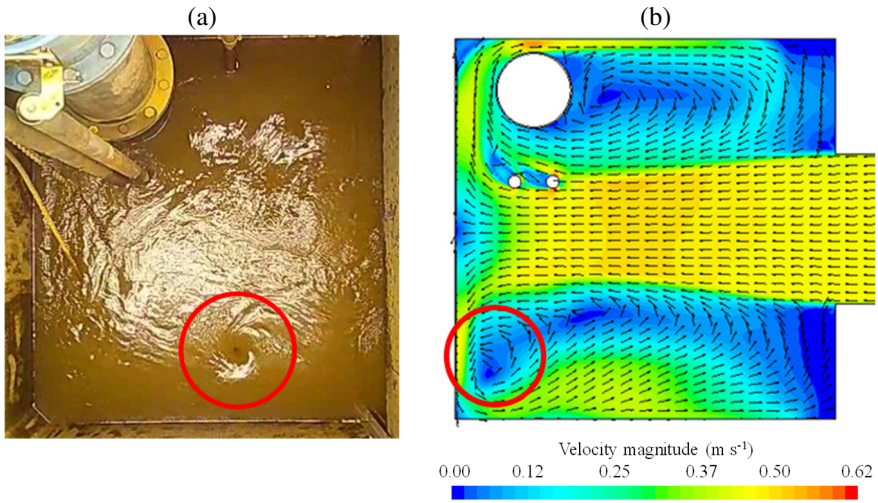


Figure F.3: (a) Occurrence of a free-surface vortex in the Breda test facility pump sump at a flow rate of  $275 \text{ m}^3 \text{ h}^{-1}$  and constant water depth of 0.93 m. (b) CFD results showing the water surface velocity vectors. The red circled area shows a clear flow circulation. The axis of this circulation is defined as a vortex core which provides an indication of the position of a possible strong free-surface vortex.

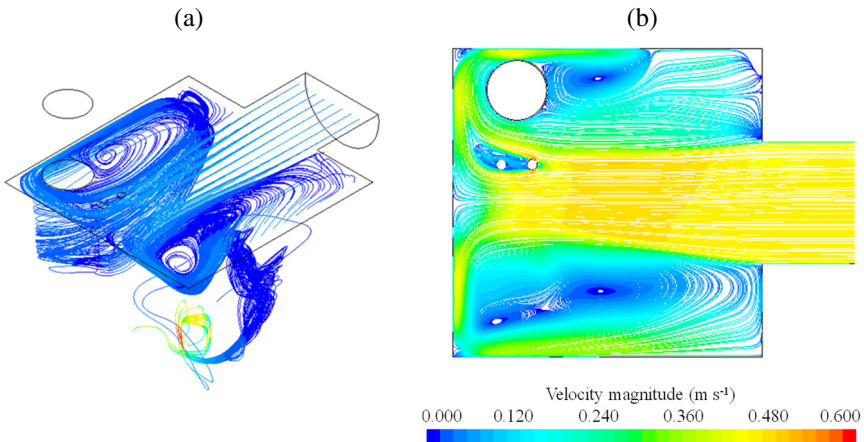


Figure F.4: (a) CFD results of the 3D flow streamlines in the Breda test facility pump sump with the origin at the surface. (b) CFD results of horizontal surface flow velocities.

by the 3D flow streamlines as shown in Figure F.4. Consequently and regarding rectangular shaped sump geometries with jet-shaped inflow, the use of CFD with a single-phase approach seems usable to simulate the occurrence of free-surface vortices. Furthermore, it is obvious apparent that the CFD flow pattern is more

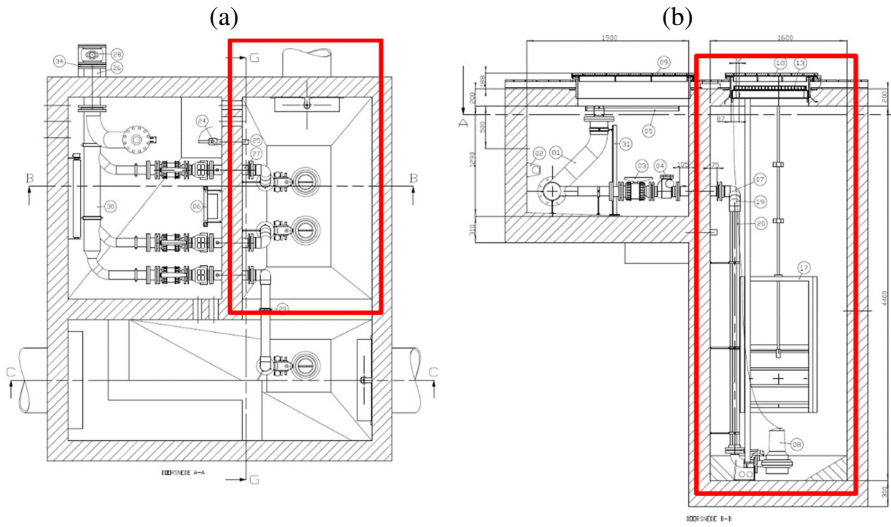


Figure F.5: Construction drawings of the WWPS. The red lines indicate the pump sump as modelled in CFD. (a) Top view. (b) Side view.

stratified than the ‘chaotic’ 3D moving water surface in the test facility. This is a result of the single-phase approach which does not model the interaction between the different phases. To simulate this interaction, the simulation should be carried out with a multi-phase model.

## F.2 CASE 2: THE WASTEWATER PUMPING STATION PUMP SUMP

### DESCRIPTION OF THE PUMP SUMP

The wastewater pumping station (WWPS) is located in Rotterdam, The Netherlands, see Figure F.5. The sump surface area is  $1.60 \times 2.50$  m and the height is 4.40 m. The WWPS has two submerged pumps for the discharge of wastewater. The fixed capacity is  $\sim 35 \text{ m}^3 \text{ h}^{-1}$ . An Axis M1125-E Network camera is placed at the sump ceiling to record the water surface movement and the dynamic behaviour of the floating FOG particles. Figure F.6 shows a screen shot. To obtain a free-surface vortex in the pump sump there must be a ‘sufficient’ flow circulation (not quantified) and an axial flow gradient  $dV_z/dz$  (the vortex ‘stretching’, see section 3.2). The gradient is provided by the accelerating flow towards the pump suction inlet. The current flow circulation, however, seems not sufficient to obtain a free-surface vortex of strength 4 to 6 (see Figure 1.6) in the pump sump. A larger circulation can be achieved by geometrical adaptations of the sump. The suggested adaptations were tested with a CFD model as described in the next section.

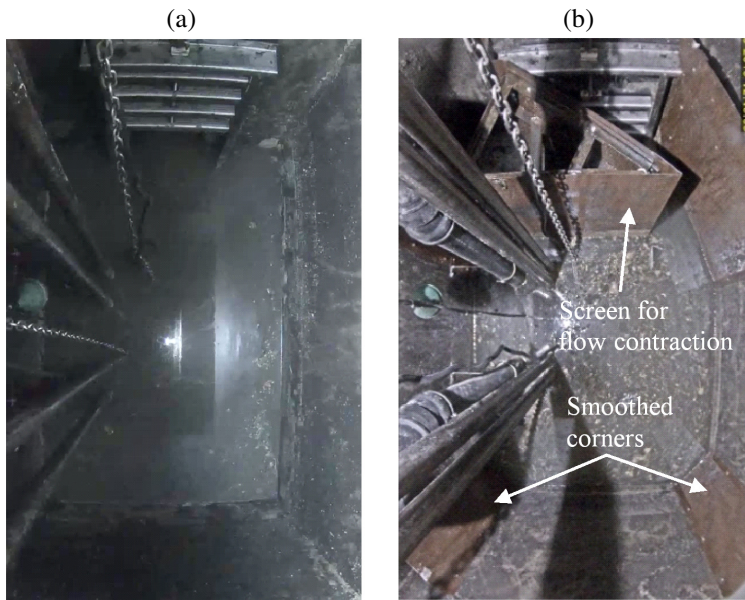


Figure F.6: Screen shot of the pump sump camera. (a) Original sump. (b) Adapted sump. A screen is placed in front of the inlet to contract the inflow streamlines and the sump corners are smoothed to guide the flow. These adaptations should provide a sufficient flow circulation.

#### THE CFD MODEL AND BOUNDARY CONDITIONS

The model uses a single-phase approach and uses the RANS turbulence model with a  $k$ - $\epsilon$  two layer model. The model has a polyhedral mesh with  $\sim 350.000$  cells. The applied fluid density and kinematic viscosity is respectively  $997.56 \text{ kg m}^3$  and  $0.891 \cdot 10^{-6} \text{ m}^2 \text{ s}^{-2}$ . The model discharges only through pump 1, see Figure F.7(a), with a constant flow rate of  $33 \text{ m}^3 \text{ h}^{-1}$ . The constant water depth in the sump is 1.2 m. The velocity profile on the inlet is based on a fully developed flow inside the pipe. The roughness height of the sump walls is 1.0 mm with a no-slip condition at these boundaries. The top side of the model represents a fixed water free-surface where a slip condition is applied and thus a non-zero tangential fluid velocity.

#### QUALITATIVE COMPARISON OF PHYSICAL RESULTS WITH CFD RESULTS

The CFD results are presented for the model with original sump geometry and the model with adapted sump geometry. To improve readability, both models are hereafter referred to as 'original sump' and 'adapted sump'. For the original sump Figure F.8(a) shows the calculated horizontal flow velocities and directions at different heights. Figure F.8(b) shows the velocities and directions for the adapted pump sump. When compared to the flow field in the CFD model of the original sump,

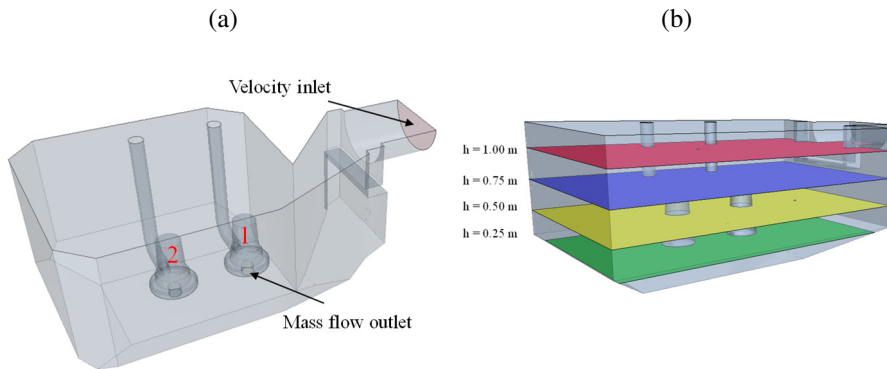


Figure F.7: (a) CFD model of the adapted WWPS pump sump. (b) Horizontal planes in the model to analyse the flow velocity fields.

the flow circulation in the adapted sump is obvious visible. The axis of the flow circulation (at  $h = 0.75$  and  $h = 1$  m) is defined as a vortex core in order to better visualize the possibility of a vortex occurrence. The strongest vortex core (and some other cores) is showed in Figure F.9

Subsequently, the geometry of the real sump is adapted as determined by the CFD results, see Figure F.6(b). Based on the CFD results, the occurrence of a free-surface vortex is expected. However, the occurrence of a free-surface vortex in the real pump sump was not observed and thus measured results were compared with CFD-results to examine differences in the results that explains the non-occurrence of the vortex. Figure F.10 shows the measured surface flow field and the CFD surface flow field. The measured and computed flow velocities are approximately similar in magnitude and direction. Consequently, differences in flow field between the experiment and the CFD model are not assumed to be responsible for the non-occurrence of the vortex. However, there are more motives left to examine that could explain the non-occurrence and are subject to further study.

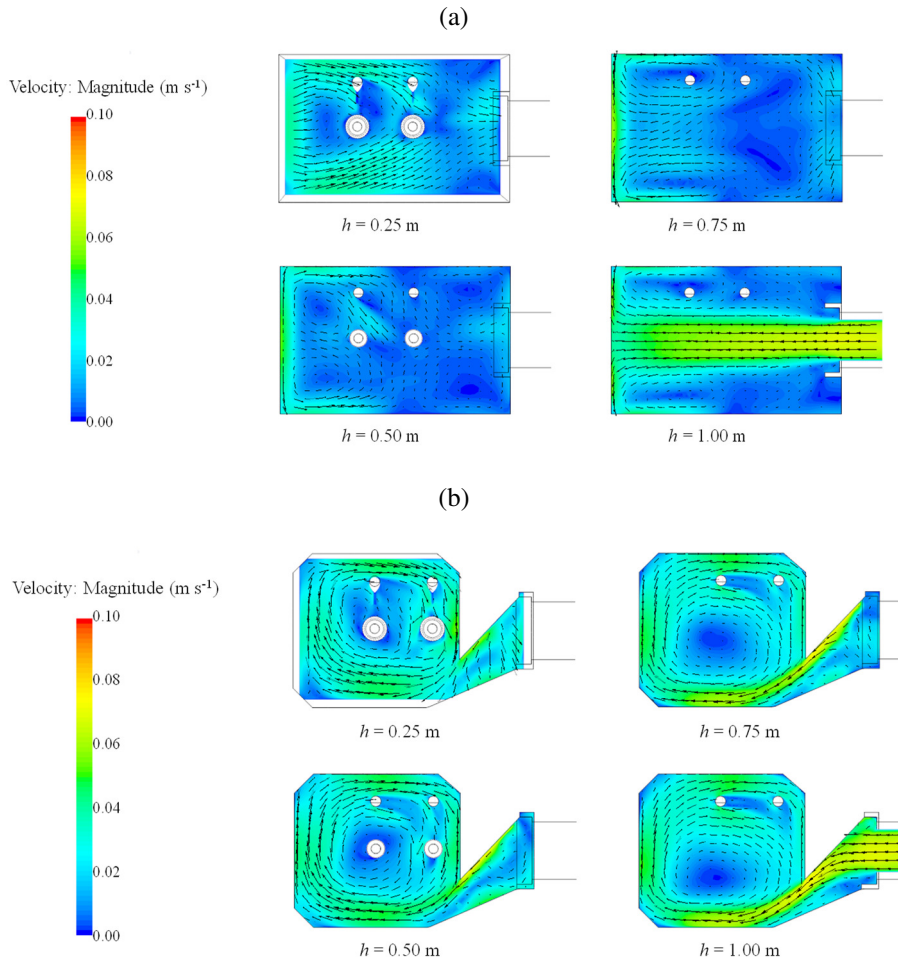


Figure F.8:(a) CFD results of the horizontal flow velocities and directions in the original sump at different heights  $h$ . (b) CFD results in the adapted sump at different heights  $h$ .

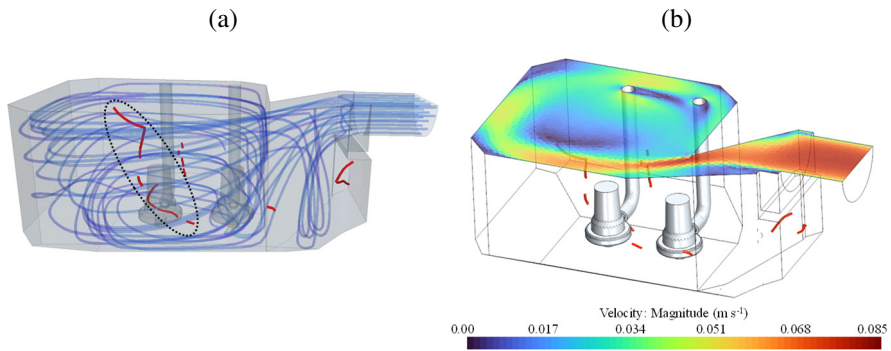


Figure F.9: (a) CFD results of the 3D flow streamlines in the adapted WWPS pump sump and the occurrence of the strongest vortex core (red line) and marked by the dashed ellipse. The core starts at the free-surface and ends in the pump suction inlet. (b) CFD results of the horizontal surface flow velocities and the occurrence of vortex cores.

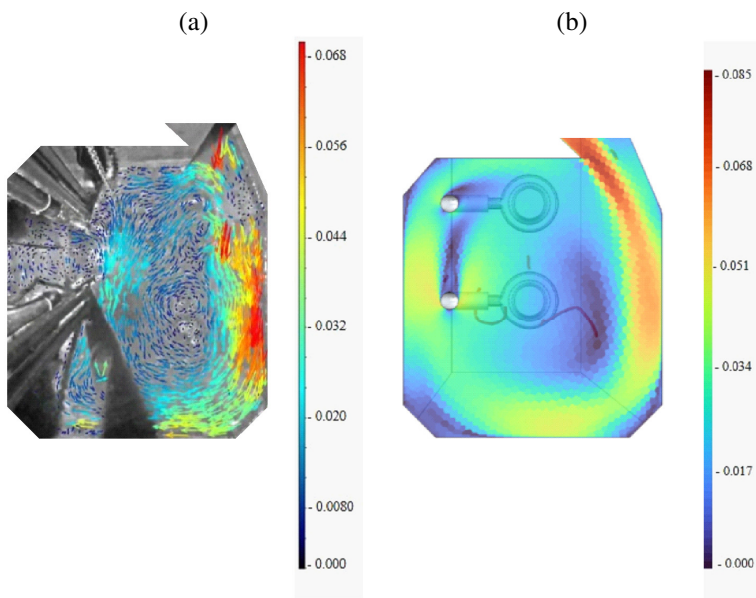


Figure F.10: Measured and CFD simulated surface flow velocities in the WWPS pump sump at similar hydraulic conditions. (a) Measured velocities. (b) CFD computed velocities and the presence of multiple vortex cores. The flow velocities are approximately similar in magnitude and direction.

# ACKNOWLEDGEMENTS

Sometime mid 2014, it crossed my mind to study the formation of floating fat layers in wastewater pumping stations. Maybe, I could find a relation between the sump geometry and the formation of these layers. This relation could help to avoid layer formation in future sump design. Now, in 2020, that thought has brought me a PhD thesis on particle transport by a free-surface vortex. However, not being aware of opening a kind of Pandora's box studying rotating two-phase systems. Off course, several people supported me to accomplish this PhD who I want to thank.

First, I'm very grateful to Ronald Zandbergen and Daphne de Koeijer from the municipality of Rotterdam. The financial support from their departments made this PhD journey possible. The experimental part of this journey started at the Breda test facility. I want to thank Peter Meissen and Martijn Klootwijk for letting me use the facility. The vortex appearance in this facility was the trigger to build Pandora's box. This brings me to thank my mate Friso for building this box (who else could I appoint if we are dealing with a 'doos'). Also thanks to Job & Jos to bring this box alive at the Deltares laboratory. Thanks to Christiaan van Nieuwenhuizen for improving the box and conducting experiments. Also thanks to Irene Clemens for building the SQL database. Special thanks to the Julio Iglesias look-a-like Antonio Moreno Rodenas for designing the 3D-PTV software. Jaap Peters, thank you for managing the experiments in the wastewater pumping station. Thanks to Koen for the history of pumping stations in Rotterdam. Thanks to my (former) TU colleagues Jeroen, Johan, Wouter, Bram, Mathieu, Adithia, Eva, Matthijs, Job and Kostas for the drinking events. Without you Bram, I would have had more brain cells left after the Prague Conference. To Mathieu: thanks for showing me the proper way to wear a sweater in Quebec.

Special thanks to Gosse Oldenziel for being my co-promoter and performing the Stereo PIV measurements. I appreciated your critical remarks.

When you are travelling you need guides. In this case four guides. The first guide I'm very grateful to is my promotor François Clemens. To ask the question who has spent more private time on this PhD, François or me, is to answer the question. To keep it short: François, many thanks for all the effort you have put into this research including the 3D-PTV design and particle tracking software. However, various brass hinge pins are still missing in our antique doors. The next two guides to be grateful to are my amazing kids Rosalie en Robin. Thank you for understanding that pappa spent so

much time in his workroom instead of spending time with you guys. The next few years, you may claim my time...And then Lysette: not only a guide but also the captain of a ship called 'family' which was often on a collision course. Every time she managed to bring the ship to safe harbour. Without you Lyset, it would have been a mess most likely...Thank you X!

# LIST OF PUBLICATIONS

## PEER-REVIEWED JOURNAL ARTICLES

- DUINMEIJER, S.P.A., MORENO-RODENAS, M.A., LEPOT, M., NIEUWENHUIZEN VAN, C., MEYER, I. & CLEMENS, F.H.L.R. (2018). A Simple measuring set-up for the experimental determination of the dynamics of a large particle in the 3D velocity field around a free-surface vortex. *Journal of Flow Measurement and Instrumentation*, doi.org/10.1016/j.flowmeasinst.2018.10.007.
- DUINMEIJER, S.P.A., OLDENZIEL, G. & CLEMENS, F.H.L.R. (2019). Experimental study on the 3D-flow field of a free-surface vortex using stereo PIV. *Journal of Hydraulic Research*, DOI: 10.1080/00221686.2018.1555558
- DUINMEIJER, S.P.A., OLDENZIEL, G. & CLEMENS, F.H.L.R. (2020) (subm.). Experimental study on the 3D-flow field of a free-surface vortex using stereo PIV, Closure. Submitted to *Journal of Hydraulic Research*.
- DUINMEIJER, S.P.A. & CLEMENS, F.H.L.R (2019). (subm.). Experimental study on free-surface vortex driven particle motion at high Reynolds numbers: helical motion along the air core. Submitted to *Journal of Hydraulic Research*.
- DUINMEIJER, S.P.A. & CLEMENS, F.H.L.R. (2019). (subm.). Experimental study on free-surface vortex driven particle motion at high Reynolds numbers: axial motion through the vortex core. Submitted to *Journal of Hydraulic Research*.
- NIEUWENHUIS, E., POST J., DUINMEIJER A., LANGEVELD, J., CLEMENS, F. (2018). Statistical modelling of Fat, Oil and Grease (FOG) deposits in wastewater pump sumps. *Water Research*, 135, 155-167.
- STELLING, G.S. & DUINMEIJER, S.P.A. (2003) A Staggered conservative scheme for every Froude number in rapidly varied shallow water flows. *Journal of Numerical Methods in Fluids*, 43: 1329-1354.

## CONFERENCE PAPERS

- DUINMEIJER S.P.A. AND VERHAART, F. (2015, June/July) *On the (in)applicability of ANSI guidelines at wastewater sump design*. Presented at the 36<sup>th</sup> IAHR World Congress, Den Haag, The Netherlands.

- DUINMEIJER, S.P.A., CLEMENS, F.H.L.R., POTHOF, I. AND VERHAART, F. (2015, June/July). *On the set-up of experiments on surface pollution influenced vortices*. Presented at the 36<sup>th</sup> IAHR World Congress, Den Haag, The Netherlands.
- DUINMEIJER, S.P.A., CLEMENS, F.H.L.R. AND VERHAART, F. (2015, September). *On the research to free-surface vortices in wastewater pump sumps*. Presented at the 10<sup>th</sup> Int. Urban Drainage Modelling Conference, Québec, Canada.
- DUINMEIJER, S.P.A. AND CLEMENS, F.H.L.R. (2016, September). *Experimental research on free-surface vortices as transport mechanism in wastewater sumps*. Presented at the 8<sup>th</sup> Int. Conference on Sewer Processes and Networks, Rotterdam, The Netherlands.
- DUINMEIJER, S.P.A. AND CLEMENS, F.H.L.R. (2017, September). *3D-PTV on large particles in the free-surface vortex*. Presented at the 14<sup>th</sup> International Conference on Urban Drainage, Prague, Czech Republic.

#### **NATIONAL PUBLICATIONS**

- DUINMEIJER, S.P.A. (2019). *Floating debris in sewer pump sumps*. Dutch Technical Magazine H2O.
- DUINMEIJER, S.P.A. (2018). *Removal of floating debris in sewer pumping stations*. Dutch Magazine of Civil Engineering.
- DUINMEIJER, S.P.A. (2014). *World Port Rotterdam needs a world-class pressurized sewer system*. Dutch Scientific Magazine for collection, transport and treatment of wastewater.

# ABOUT THE AUTHOR

Alex Duinmeijer was born on June the 2th of 1972 in Alkmaar, The Netherlands. He started with the Elementary technical school “L.T.S Sint Willibrord” in Alkmaar (1985-1989) with specialisation Electric Engineering. Then he did intermediate technical school “M.T.S Alkmaar” (1989-1993) with specialisation Energy Engineering. After graduation he studied Civil Engineering at Alkmaar University of applied sciences (“H.T.S. Alkmaar”) from 1993 till 1997. After graduating Alex studied Civil Engineering at Delft University of Technology specializing in Fluid mechanics (1997-2002). During his study Alex was employed as a student-assistant at the Fluid mechanics department of Civil Engineering. He graduated at the WL | Delft Hydraulics on the verification of a numerical model (Delft FLS / Sobek 2D) for the prediction of the two-dimensional overland flooding after a dike-break.

In 2001, Alex started his career as a researcher/consultant at the Waterloopkundig Laboratorium | Delft. Then Alex worked as a research engineer at Van Oord Dredging Contractors. Currently, he works as a senior consultant at the Engineering’s Consultancy of the municipality of Rotterdam. In this position, Alex is responsible for the (hydraulic) design of the Rotterdam wastewater transport system which is one of the largest systems in the Netherlands.

Motivated to solve practical problems by applying the laws of physics, Alex started this PhD research at the end of 2014 next to his job with Engineering’s Consultancy of the municipality of Rotterdam.